APPLICATIONS OF OPTICAL FREQUENCY COMBS IN MICROWAVE PHOTONICS AND QUANTUM OPTICS

A Dissertation

Submitted to the Faculty

of

Purdue University

by

Mohammed S. Al Alshaykh

In Partial Fulfillment of the

Requirements for the Degree

of

Doctor of Philosophy

December 2020

Purdue University

West Lafayette, Indiana

THE PURDUE UNIVERSITY GRADUATE SCHOOL
STATEMENT OF DISSERTATION APPROVAL

Prof. Andrew M. Weiner, Chair
School of Electrical and Computer Engineering

Prof. Minghao Qi
School of Electrical and Computer Engineering

Prof. Sunil Bhave
School of Electrical and Computer Engineering

Prof. Peter Bermel
School of Electrical and Computer Engineering

Approved by:

Prof. Dimitrios Peroulis
Head of the School Graduate Program

To my mother, my first teacher, and the one who's always been by my side.

To my father, the pillar of support in my life and the man whom I always look up to.

ACKNOWLEDGMENTS

Throughout my life, I have been blessed with the company of caring friends and family. I thank God first and foremost for this blessing, and I thank my mother and father who have always been by my side; I could not have done this without your support.

I also want to express my heartfelt thanks to my advisor Prof. Andrew Weiner for his guidance and patience on my – often incoherent – ideas, especially during my first two years! During my Ph.D. career, I had the opportunity to work on topics covering, biomedical imaging, integrated optics, microwave photonics, frequency metrology, and quantum photonics. Such opportunities wouldn't be available in most other labs. I will always be inspired by Prof. Weiner's ability and eagerness to learn new topics and by his ability to apply his knowledge to contribute to those fields. My gratitude extends to my committee members: Prof. Minghao Qi, Prof. Sunil Bhave, and Prof. Peter Bermel for their time and comments. A special thanks goes to Prof. Qi not only for the infinite supply of microrings but also for his ever so gracious and humble manners; it has been a pleasure working with you.

Being a part of the Ultrafast Optics and Optical Fiber Communications group gave me a chance to work with and meet colleagues who made my years at Purdue much more enjoyable. First, I want to thank Dr. Daniel Leaird for his invaluable help in the laboratory. His supernatural abilities to fix any malfunction, procure equipment, and construct whatever setup needed in the machine shop will surely be missed! I also thank Dr. Poolad Imany whom I have had the pleasure to work closely with under multiple successful – and unsuccessful – projects! My thanks and gratitude extend to my colleagues: Dr. Andrew Metcalf, Dr. Xiaoxiao Xue, Dr. Hyoung-Jun Kim, Dr. Pei-Hsun Wang, Dr. Chengying Bao, Dr. Jose Jaramillo-Villegas, Eric Topel, Dr. Ogaga Odele, Dr. Bohao Liu, Dr. Oscar Sandoval, Ziyun

Kong, Keith McKinzie, Cong Wang, Abdullah Al Noman Ovi, Hsuan-Hao (Peach) Lu, Nathan OMalley, Navin Lingaraju, Alexandria Moore, Suparna Seshadri, Karthik V. Myilswamy, Lucas Cohen, Saleha Fatema, and Michael Kickbush. I also acknowledge my collaborators: Dr. Jason D. McKinney, Dr. Joseph Lukens, Prof. Victor Torres-Company and his group, Prof. Sabre Kais and his group, and Prof. Ji-Xin Cheng and his group.

Academic and professional degrees are nothing without the personal connections we make. My years at Purdue gave me a chance to forge new friendships that I will cherish for life. Your company made life much more enjoyable, exciting, and fun! And for some of you, I say: see you soon!

TABLE OF CONTENTS

Page

Page

LIST OF TABLES

Table Page

LIST OF FIGURES

Figure Page

ABSTRACT

Al Alshaykh, Mohammed S. Ph.D., Purdue University, December 2020. Applications of Optical Frequency Combs in Microwave Photonics and Quantum Optics. Major Professor: Andrew M. Weiner.

Remarkable miniaturization of optical frequency combs was achieved using integrated microring resonators based on the Kerr nonlinearity. Operated below the parametric instability threshold, such microrings can generate high-dimensionally entangled biphoton frequency combs. To process such states, we encode qudits in the time and frequency degree of freedom of a single photon and experimentally demonstrate a deterministic high-dimensional 16×16 SUM gate. We then operate this gate on two frequency-bin entangled photons–each carrying two 32-dimensional qudits–to generate a two-photon four-party Greenberger-Horne-Zeilinger state. Subsequently, we utilize single-photon encoding concepts to demonstrate the first qutrit-based phase implementation of the quantum phase estimation algorithm – a key subroutine of several important algorithms – and successfully retrieve the eigenphase with one ternary digit of precision. Lastly, by manipulating the input state using an electro-optic phase modulator, we implement a tunable frequency-domain quantum walk demonstrating ballistic energy transport and energy bound states. These demonstrations highlight the potential of frequency-domain encoding and processing using well-established tools developed for the communication industry. The second part of this thesis focuses on the microwave photonic applications of frequency combs. Using dual electro-optic combs, we exploit the Vernier effect to develop an optical-based radio-frequency subsampled link and derive a detailed analytical model identifying a third-order limited operational point. In a second demonstration, we use Kerr combs to mitigate detrimental stimulated Brillouin scattering effects in long-haul analog optical links. Using

both dark pulses and solitons in a sampled analog link, we perform thorough measurements of the analog link metrics to compare their performance and study the effect of the combs' conversion efficiency. Finally, we report on our progress towards integrating atomic-optical clocks, where we experimentally generate on-chip octave-spanning solitons and discuss a novel Vernier division scheme to readout the comb's large repetition rate. To address challenges imposed by the low comb-line powers, we propose a comb stabilization scheme that utilizes the clock laser for the nonlinear frequency mixing operations, relieving the need for external lasers or amplifiers.

1. OPTICAL FREQUENCY COMBS

1.1 Introduction

As is the case with many scientific explorations, the story of optical frequency combs is one of unexpected twists and surprises. After the invention of the laser, the community diverged to multiple branches. One was focusing on developing stable continuous wave (CW) lasers for narrow-line spectroscopy, while the other was pushing the limits on generating ultrashort optical pulses leading to pump-probe experiments at unprecedentedly short timescales. In the late 1990s, these two communities joined forces in a quest to push the limits of time-keeping and precision. Armed with advancements in the engineering of nonlinear materials, researchers demonstrated the first fully referenced coherent octave-spanning frequency comb—providing a phase-coherent link between atomic transitions and the microwave domain which facilitates the readout of atomic clocks. The importance of timekeeping and historical advancements in the field are summarized by Hall and Hänsch [1, 2], who shared half of the Noble prize in physics in 2005.

It is insightful to look at optical frequency combs (OFC) in both the time and frequency domain pictures, shown in Fig. 1.1. We see a periodic train of pulses, e.g. from a mode-locked laser, with a repetition period of τ_{rep}, which through the Fourier transform results in the discretization of the spectral envelope that is centered at some carrier frequency. The width of the envelopes in the two domains has an inverse relationship—shorter pulses are created by coherently adding more spectral lines. The temporal envelope of the pulse has underlying oscillations at the carrier frequency. When looking at these oscillations from pulse to pulse, a phase slip is noticed. Physically, this slip arises from the carrier traveling at a phase velocity v_p while the envelope lags behind traveling at a group velocity v_g. This mismatch

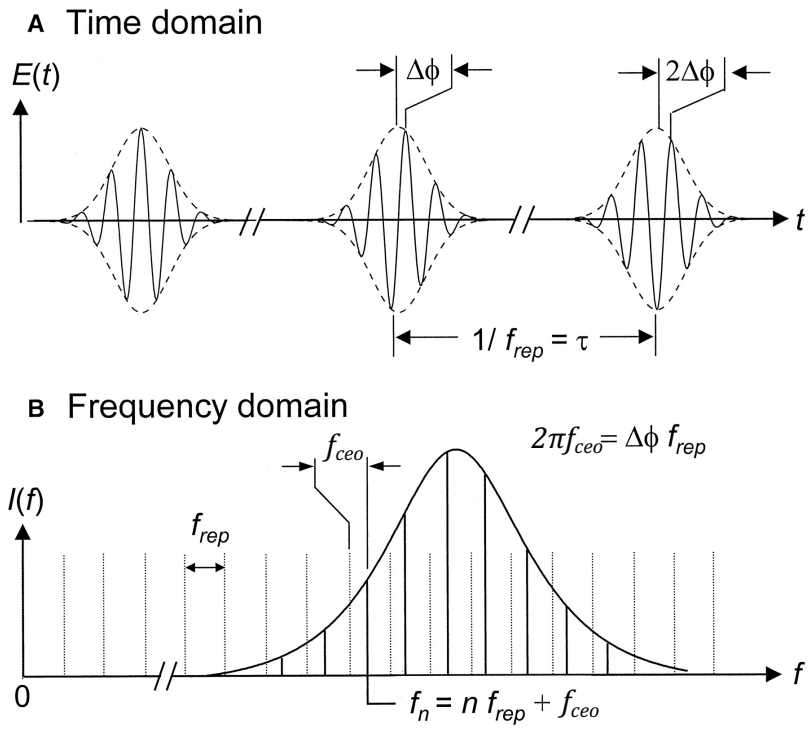

Fig. 1.1. Time and Frequency representation of a frequency comb. A)In the time domain, a phase slip between the carrier (solid) and the envelope (dotted) aggregates from pulse to pulse. B) In the frequency domain. Figure adapted from [3]

between phase and group velocity is a result of dispersion inside the cavity, leading to a phase relationship

$$2\pi\nu_n\tau_{rep} = 2\pi n + \Delta\phi_{ceo} \tag{1.1}$$

which can be rewritten as

$$\nu_n = f_{ceo} + nf_{rep} \tag{1.2}$$

where the carrier-envelope offset $f_{ceo} \equiv f_{rep}\Delta\phi_{ceo}/2\pi$. Remarkably, the frequency of any comb line (ν_n) is defined by two microwave frequencies, f_{rep} and f_{ceo}. By stabilizing the comb's two degrees of freedom through feedback servo loops, the comb is said to be self-referenced. Typically, f_{rep} is stabilized by photodetecting the pulse train and locking f_{rep} to a microwave reference through feedback to the laser cavity.

Provided the comb spans an octave, f_{ceo} can be detected following the f-to-2f scheme, which will be discussed in chapter 7, and stabilized to a reference typically through feedback control of the pump laser's power. With the f_{ceo} stabilized, a comb line can be heterodyned and locked to some optical reference. The comb then provides a phase-coherent link that divides the optical reference down to f_{rep}.

While frequency meteorology and timekeeping were the main motivations behind developing OFCs, numerous other fields are benefiting from it. Some examples include dual-comb spectroscopy of molecular vibration, ranging, low-noise microwave generation, and a host of photonics-based radio-frequency (RF) signal processing capabilities. Luckily, not all of these applications require fully referenced combs, but each application has a preference for a certain comb spacing. This is elegantly illustrated in the application wheel picture, Fig.1.2, adapted from a review article on OFC applications by Newbury [4].

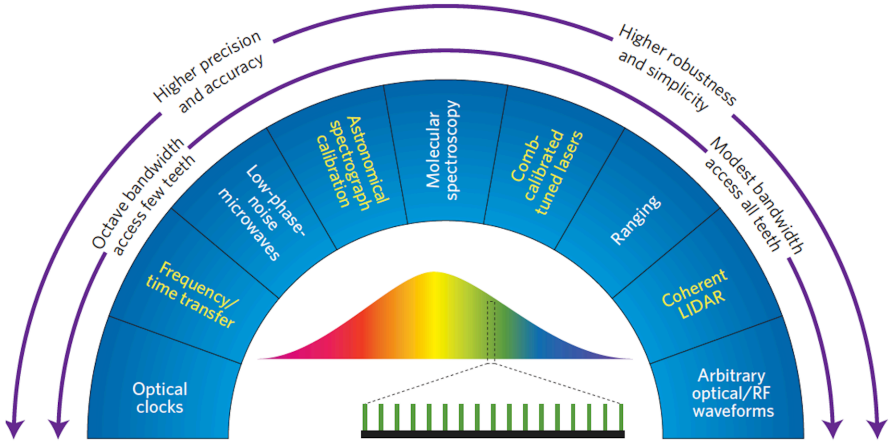

Fig. 1.2. Applications of optical frequency combs. Figure adapted from [4].

In this thesis, we will focus on combs with large repetition rates ($f_{rep} \geq 10\ GHz$). Electro-optic (EO) and Kerr combs are two examples of such sources. They are briefly introduced in the following sections.

1.2 Electro-Optic Combs[1]

EO combs are the most commonly used OFC source in RF-photonics. They have the advantage of reliability, robustness, ease of operation, and simple repetition rate tunability by adjusting the frequency of the driving RF oscillator. Typical commercial phase modulators based on $LiNbO_3$ have an insertion of loss 2 to 4 dB and support an RF bandwidth of 20 to 40 GHz with a V_π of 3 to 4 V at 10 GHz and an RF power handling of 1 W, resulting in $\sim$ 20 spectral lines at -10 dB with spectral envelope following a Bessel distribution. By cascading intensity (IM) and phase (PM) modulators [6], flat-top combs can be generated, see Fig. 1.3. Further flat comb generation techniques are detailed in [7]. Note that the bandwidth scales linearly with the modulation index or RF-voltage, which might not be appealing for applications with strict constraints on power consumption. Efforts in integrating such modulators are heavily pursued. Recent advancements in thin-film LN modulators [8] demonstrated impressive improvements in the RF-bandwidth $\geq$ 100 GHz, reduced loss, high RF-power handling, and a voltage-length product of 2.2 V·cm. In another promising platform for integration, InP, an integrated flat-top comb generator system consisting of an intensity modulator cascaded with 2 PMs generating 28 comb lines. The full system with an on-chip laser has a footprint of $4.5 \times 2.5\ mm^2$ [9].

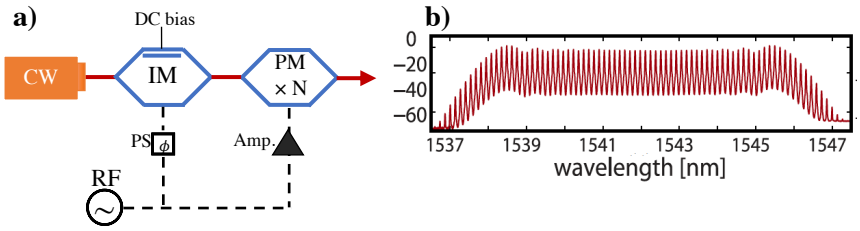

Fig. 1.3. EO combs. a) Comb generator using a cascaded IMs and PMs setup. b) A 17 GHz comb using 3 cascaded PMs and an IM [6].

Another interesting OFC generator is the resonant EO-comb generators. By placing the modulator in a Fabry-Perot cavity, the light becomes trapped in the cavity

[1]The results in this section are partially adapted from the publication [5]

for several round trips passing through the phase modulator multiple times [10]. This design enhances modulation efficiency at the expense of reduced tunability, as the repetition rate is set by the round trip of the cavity. Note that it still requires an external RF-drive. The comb's bandwidth offered by such modulators is proportional to the product of the modulation depth and quality factor, however; material dispersion eventually becomes the limiting factor [11]. Time-domain analysis through line-by-line pulse shaping shows that such a comb generator gives rise to two pulses per modulation period [12]. Early demonstrations required stabilization and feedback locking loops, along with high losses and limited dispersion engineering in bulk modulators, these constraints limited the spread of such comb generators. However, using a low loss thin-film $LiNbO_3$ ring resonators in which the dispersion can be optimized via appropriate waveguide design, researchers in [13] demonstrated larger comb bandwidths with reduced losses and improved optical and microwave field overlap, reigniting interest in such comb sources.

1.3 Kerr Combs

Outstanding miniaturization of OFC generators was achieved using high-quality factor (Q) integrated non-linear ring resonators, often referred to as Kerr combs. The resonant enhancement and tight confinement of light along with the right balance between dispersion and loss pave the way to broadband comb generation from a continuous wave (CW) pump. The two most common types of resonators are:- whispering gallery mode resonator (WGM) and on-chip integrated microring resonators. WGM resonators are fabricated using fused Silica or crystalline (MgF_2, CaF_2) materials with high Q-factors ($10^8 - 10^{10}$). For integrated microcombs, Si_3N_4 is the most common platform offering Qs between 10^5 and 10^7.

The nonlinear dynamics can be described by the Lugiato-Lefever equation (LLE). A simple way of thinking to understand the LLE equation is to think about a nonlinear Schrödinger (NLS) equation with a damping term arising from cavity losses.

Combined with a periodic boundary condition imposed on the circulating cavity field and a driving term to account for the CW pump, these two equations form an infinite-dimensional map (Ikeda map) describing the nonlinear dynamics. Direct simulation of the two equations is computationally exhaustive as it requires a step smaller than the cavity length. In the limit of high finesse cavities, the field is slowly varying over a round-trip, and these two equations can be averaged leading to the mean-field LLE

$$t_r \frac{dE(t,\tau)}{dt} = \left(-i\delta - (\alpha+\kappa)/2 + i\gamma L|E|^2 + L\sum_{n=2}^{\infty} i^{(n+1)} \frac{\beta_n}{n!} \frac{d^n}{d\tau^n} \right) E + \sqrt{\kappa}\ E_{in} \quad (1.3)$$

where $E, L, t_r, \beta, \gamma, \alpha, \kappa, \delta, E_{in}$ are the envelope of the intracavity field, cavity length, roundtrip time, group-velocity dispersion, nonlinear coefficient, intrinsic and coupling loss, pump phase detuning, and the CW pump amplitude, respectively [14]. The continuous variable t is the 'slow' time, and τ is the 'fast' time. This approximation is valid if the dispersion and nonlinear lengths are longer than the cavity length, and the detuning is small relative to the free spectral range (FSR). Alternatively, an equivalent spatio-temporal form of the LLE can be derived starting from a modal expansion approach [15]. It is instructive to look at the case where only second-order dispersion is present ($\beta_{n\geq 3} = 0$). The nonlinear dynamics vary significantly depending on the sign of the dispersion.

Anomalous Dispersion ($\beta_2 < 0$)

Stability analysis of the LLE in the anomalous dispersion regime shows rich nonlinear dynamics [16]. The bifurcation diagram is shown in Fig. 1.4 as a function of two normalized parameters, detuning and pump power. Other than the CW solutions, three regions can be identified. The First is Turing rolls or stable modulation instability (MI), which typically has few spectral lines separated by multiple FSRs. The spacing can be predicted by calculating the peak of the modulation instability gain. In the time-domain, Turing rolls correspond to identical multiple short pulses circulating in the cavity. The second region is the chaotic region, which typically has single FSR combs with high pump conversion efficiencies, however, the comb is

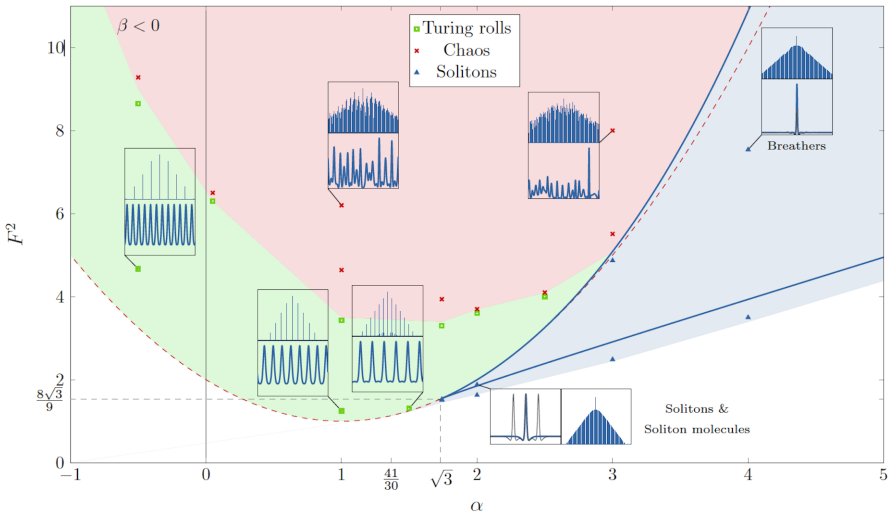

Fig. 1.4. Bifurcation diagram, the x-axis is the normalized detuning and the y-axis in the normalized pump power. Figure adapted from [16].

incoherent exhibiting a noisy temporal profile. The third region is the soliton region, which has a rich variety of coherent solutions. Some appear as multiple interacting co-propagating inside the cavity, others behave as crystals in which the pulses are equidistant thereby resulting in comb with FSR spacing equal to the number of circulating pulses. The most sought after solution is the single soliton since it gives a smooth single FSR sech^2 spectral profile. Within this region, soliton breathers also exist, where the pulse-width oscillates at a time scale much longer than the roundtrip time.

The standard experimental method for generating solitons is to start with a CW laser at a fixed power level and increase the wavelength. Upon entering the resonance, we typically observe Turing rolls, followed by a higher intracavity power chaotic single FSR region. As we further increase the detuning, the intracavity power rapidly decays to a soliton state. The intracavity power for N multiple solitons is N times that of a single soliton. This step-like drop in intracavity power is a signature of solitons [17]. Nevertheless, experimentally, thermal effects complicate the process of achieving and locking to a soliton state. The rapid drop in intracavity power results in a

drop in temperature, which changes the refractive index and the resonance location, thereby increasing the effective detuning between the pump laser and the resonance. This increase in effective detuning can eventually place the laser outside the soliton existence range. The thermal response time of Si_3N_4 is c. 100-500 ns, resulting in short-lived solitons. These thermal effects also shift the soliton regions, rendering single solitons inaccessible through the usual forward tuning method. Methods to access the single soliton state through a combination of forward followed by backward tuning has been demonstrated [18]. Several methods have been adopted to mitigate thermal effects, including fast tuning [19], power-kicking [20], phase modulation of the pump [21], the use of auxiliary pump lasers [22, 23] and operating the microring at cryogenic temperatures [24].

The repetition rate of Kerr combs is tightly set by the dimension of the resonator and does not require any external RF drive. The repetition rates of demonstrated solitons for WGM resonators are on the order of few to tens of GHz while for microring resonators are typically ≥ 80 GHz except for a recent demonstration achieving solitons with repetition rates of 10-20 GHz [25, 26]. Such mode-locked on-chip pulses proved useful for a plethora of applications, e.g, LIDAR, coherent digital communications, spectroscopy, and microwave signal generation. From an application perspective, the main drawback of the single soliton state is its low pump conversion efficiency, ca. 1% or lower. For a more detailed review of the Kerr comb applications and platforms, we refer the reader to [27]. The aforementioned improvements in $LiNbO_3$ have made their way to Kerr combs. So far, these came with pleasant surprises, as the photorefractive effect allowed accessing solitons from the high wavelength side via slow tuning as well as novel switching between soliton crystals [28, 29].

Normal Dispersion ($\beta_2 > 0$)

In the normal dispersion regime, the nonlinear regions are not as rich and wide as the previous case [16]. Turing rolls and dark solitons - which appear as dips in the

time-domain- can exist within a narrow region. Note that this stability analysis gives no information about the accessibility of such states. Dark solitons, or platicons, were observed in WGM resonators where the coupling between the back-scattered wave and the pump diode laser is believed to have had a role in accessing such states [30]. Other tricks involved avoided mode crossings, at which a resonance exhibits local anomalous dispersion that initiates the modulation instability process [31]. Demonstrated dark pulses have shown significantly higher conversion efficiencies (10% to 30%) [32]. An advantage of the high conversion efficiency is that no significant power drops are observed, so the state can be accessed via slow tuning.

1.4 Biphoton Frequency Combs

The previous discussion of microrings focused on pumping above the parametric generation threshold. Pumped below the threshold, the spontaneous four-wave mixing (SFWM) effect arising from the $\chi^{(3)}$ nonlinearity leads to the generation of entangled photons (biphotons), annihilating two pump photons and creating an entangled pair of signal and idler photons. The resonator's periodic boundary condition results in biphotons created in a superposition of discrete frequency modes, i.e. a biphoton frequency comb (BFC). The biphotons can be written as

$$|\psi\rangle = \sum_{1}^{N} \alpha_m \, |m, m\rangle_{SI} \tag{1.4}$$

with

$$|m, m\rangle_{SI} = \int d\Omega \; \Phi(\Omega - m\Delta\omega) \, |\omega_o + \Omega, \omega_o - \Omega\rangle_{SI} \tag{1.5}$$

where the subscripts (S,I) denotes the signal and idler photons, $|m, m\rangle_{SI}$ refers to the m^{th} frequency mode, N is the total number of mode pairs, $\Phi(\Omega)$ is the lineshape function, $\Delta\omega$ is the angular FSR and ω_o is the pump frequency. The entangled photons are in a superposition of N discrete frequency modes, i.e. a biphoton frequency comb. Notice that in eq. 1.4, α_m is a complex amplitude parameter, indicating a phase

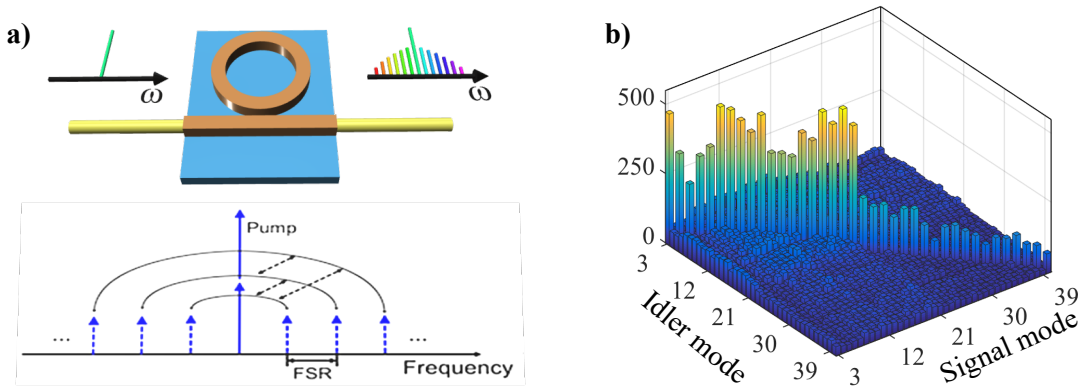

Fig. 1.5. Biphoton frequency combs. a) Two pump photons are annihilated, generating two photons in a superposition of frequencies. The solid lines indicate frequency correlation while the connecting dashed lines highlight the spectral phase coherence. b) JSI of a 50 GHz Si_3N_4 resonator [33].

coherence between different comb line pairs—an intriguing similarity to previously discussed mode-locked pulses.

To show the phase coherence and prove the high dimensional entanglement, frequency projections and state tomography can be performed using a phase modulator to mix different frequency-bins [33, 34]. An example of the joint spectral intensity (JSI) from a 50 GHz resonator is shown in Fig. 1.5b, showing frequency correlations between 40 mode pairs. This highlights the advantage of operating in the frequency domain, as simple passive elements can be used to generate 40-dimensional qudits confined within a single spatial beam. The processing of such signals can then build on well-developed, off-the-shelf equipment, and wavelength division multiplexing (WDM) techniques established for the digital communication industry. Indeed, a quantum frequency processor based on a pulse shaper sandwiched between two-phase modulators has shown versatile programmable operation, performing single photon Hadamard gates and Tritters [35], as well as two-photon Hadamard and Controlled-NOT (CNOT) gates [36]. For additional details, the interested reader can refer to this recent review article [37].

Alternatively, entangled photons can be generated using a $\chi^{(2)}$ nonlinear material such as periodically poled Lithium Niobate waveguides (PPLN), where the phase matching can be engineered to generate a broadband 'continuous' spectrum. To get a BFC, the waveguide can be enclosed within a resonator, alternatively, the spectrum can be shaped and filtered using an etalon or a pulse shaper. In many experiments, we choose to work with the latter as the programmability of the pulse shaper offers us the flexibility of setting a suitable FSR.

1.5 Thesis Outline

The thesis is a collection of multiple projects focused on the generation, processing, or applications of optical frequency combs, and can be split into two main themes: one focusing on the processing of high-dimensional entangled BFCs, while the other focuses on the applications of classical combs in microwave photonics and metrology. The quantum optic theme of the thesis is spanned by chapters 2 through 4. In chapter 2, we design a high dimensional SUM gate, prove its coherence, and subsequently use it to generate a high-dimensional four-party two-photon Greenberger-Horne-Zeilinger State (GHZ). We then build on these time-frequency processing concepts to demonstrate a qudit-based phase estimation algorithm. Finally, we observe the quantum walk dynamics of a BFC in the frequency domain and study the effects of the entanglement dimensionality. The following three chapters deal with classical OFCs. In chapter 5, we use dual electro-optic combs and utilize the Vernier effect for microwave sub-sampling and disambiguation. In chapter 6, we use Kerr combs to mitigate detrimental Brillouin scattering effects in long haul analog optical links, performing the first detailed measurements of the link metrics using dark pulses and single solitons. Finally, chapter 7 reports on our ongoing progress towards generating octave-spanning Kerr combs as part of an ambitious project aiming at integrating atomic-optical clocks. We propose novel ideas to circumvent key challenges unique

to our integrated comb source—namely the electronic readout of the comb's high repetition rate, and the low comb line powers.

2. PROCESSING OF HIGH DIMENSIONAL NON-SEPARABLE STATES

2.1 Introduction[1]

The promise of exponential speed-ups in computational time using quantum-based algorithms as well as secure communications fueled a wide-ranging interest in quantum computation, simulation, and information processing [41]. The building block of any algorithm is the quantum particle which can be in a superposition of different states—two in the case of qubits. Qubits can be generated using multiple platforms including photons [42], electron and nuclear spin [43, 44], atoms [45], trapped ions [46], superconducting electronics circuits [47,48], Quantum dots [49] and dopants in solid-state materials [50], see [51] for more details. To implement even rudimentary quantum algorithms, such building blocks are required to be robust and sufficiently long-lived. Due to their weak interaction with the environment, photons enjoy a long coherence time even when operated at room temperature [52]. As in the classical domain, photons are a leading candidate for long-range transmission and communications. Qubits can be encoded using different degrees of freedom in a photon, such as polarization [53], path [54] ,orbital angular momentum [55] and time [56], see [57] for a more exhaustive review. Until recently, the frequency degree of freedom, comparatively, attracted less attention. Surging interest in the frequency domain was excited by the demonstration of on-chip integrated time-frequency entangled photon sources, which was briefly reviewed in the introductory chapter.

[1]The results in this chapter are adapted in whole or part from the publications [38–40]

2.2 Encoding Multiple Qudits in a Single Photon

Photons' weak interaction with their surrounding is a blessing and a curse at the same time, as it makes photon-photon interactions very difficult to achieve. This renders two photon-based two-qubit gates - essential for any quantum algorithm - to be probabilistic, i.e. the gate is successful some of the time. To sidestep the challenges of probabilistic multiphoton interactions, encoding qubits in different degrees of freedom (DoFs) in a single photon has been demonstrated, where each DoF carries one qubit and, now, operations between different qubits can be made deterministic [58, 59].

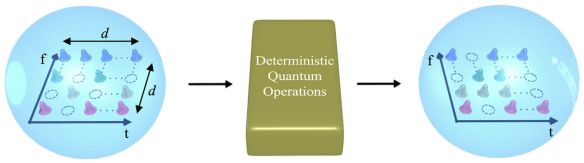

Fig. 2.1. Illustration of the scheme. Two qudits encoded in d time bins and frequency bins in a single photon, going through a deterministic quantum process. The single-photon can be encoded in an arbitrary superposition of different time and frequency bins; the unused time-frequency slots are shown with dashed circles. After the deterministic quantum process operates on the two-qudit state, the orientation of the time-frequency superpositions changes to a new two-qudit state.

In this chapter, we take advantage of the high dimensionality in two particular DoFs of a single photon—namely, time and frequency, which are both compatible with fiber optical transmission—to encode one qudit in each DoF. We consider multiple time bins and frequency bins; as long as the frequency spacing between different modes (Δf) and the time-bin spacing (Δt) are chosen such that they exceed the Fourier transform limit (i.e., $\Delta f \Delta t > 1$), we can manipulate the time and frequency DoFs independently in a hyper-encoding fashion, using concepts developed in time-division and wavelength-division multiplexing, respectively [60, 61]. In other words, each time-frequency mode pair constitutes a well-defined entity, or plaquette [60, 61], which is sufficiently separated from its neighbors to provide stable encoding (Fig. 2.1). Alternatively, this can be understood by considering bandwidth-limited plaquettes

with individual spectral linewidth δf (corresponding to temporal duration $\sim 1/\delta f$). These will not overlap in time-frequency space as long as the chosen bin separations satisfy $\Delta f > \delta f$ and $\Delta t > 1/\delta f$. Combined, then, these two equations yield the aforementioned condition $\Delta f \Delta t > 1$.

For a qudit, the Hilbert space equals d^n, where d in the dimensions and n is the number of qudits. Since our single photons can potentially be generated in a superposition of many time and frequency bins, the Hilbert space can be significantly expanded. Ultimately though, the DoFs are limited, and more importantly, they do not offer exponential scaling—the main allure of quantum computing. Nevertheless, two-qudit optical gates are useful in transmitting quantum states with higher information content per photon through qudit teleportation [62], a task that requires two-qudit gates which can operate on the different degrees of freedom of a single photon [63, 64]—precisely the functionality we demonstrate here.

To enable the realization of all single-qudit unitaries, it is sufficient to demonstrate the generalized Pauli gates X (cyclic shift) and Z (state-dependent phase), which are universal for single-qudit operations [55]. The Z gate applies a unique phase shift to each of the d basis states, which can be easily executed with a phase modulator and a pulse shaper in the time domain and frequency domain, respectively. Specifically, for the basis state $|n\rangle$ $(n = 0, 1, \ldots, d-1)$, we have $Z|n\rangle = exp(2\pi i n/d)|n\rangle$ and $X|n\rangle = |n \oplus 1\rangle$, where $\oplus$ denotes addition modulo d. An X gate in the frequency domain can be realized using a Z gate sandwiched between two high-dimensional DFT gates. Such a DFT operation has been recently demonstrated [35], completing in principle the universal gate set for single-qudit frequency-domain operations. The gate set in the time domain, was completed recently after the demonstration of the time-bin X gate done in our group [40]. Subsequently, my colleagues performed a two-qudit gate, controlled-increment (CINC) operation, where an X gate is applied to the time-bin qudit only when the frequency qudit is in the state $|1\rangle_f$. This two-qudit gate along with arbitrary single-qudit gates [which, as noted above, can be

formed from qudit X and Z operations [55]] complete a universal set for any quantum operation [65].

In the next sections, we build on this work and expand it to realize deterministic two-qudit gates, where the frequency DoF acts as the control and the time DoF is the target qudit. We implement an even more complex operation, the SUM gate—a generalized controlled-NOT gate [66]—which adds the value of the control qudit to the value of the target qudit, modulo d (where d is the dimension). We demonstrate a 16×16 SUM gate, prove its coherence, and utilize it to generate a two-photon four-party Greenberger-Horne-Zeilinger (GHZ) state.

2.3 SUM Gate

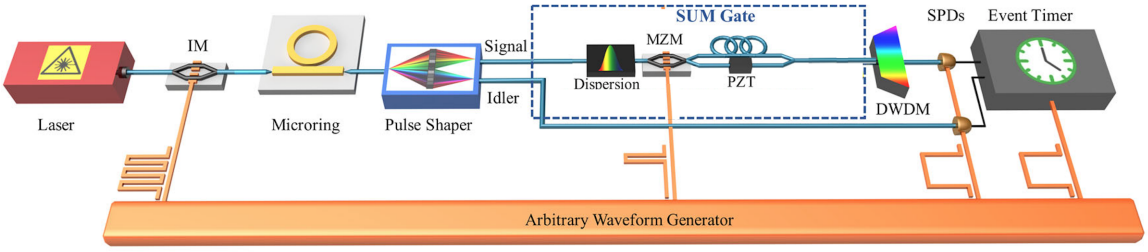

Fig. 2.2. Experimental setup for the SUM gate. IM intensity modulator, PM phase modulator, MZM Mach-Zehnder modulator, PZT piezo-electric-phase shifter, SPD single-photon detector. The MZM separates the time bins that fall outside of the computational space ($|3\rangle_t$ and $|4\rangle_t$) from the computational space time bins ($|0\rangle_t$, $|1\rangle_t$, and $|2\rangle_t$). DWDM dense wavelength-division multiplexer.

The experimental setup, shown in Fig. 2.2, can be split into three stages: state preparation, gate operation and state measurement. For the state preparation, single photons are heralded by detecting the partner photon of a frequency-bin entangled pair generated through spontaneous four-wave mixing in an on-chip silicon nitride microresonator. The time bins, defined by intensity modulation of the pump placed prior to the microring, couple into a microring resonator with a free spectral range

(FSR) Δf = 380 GHz and resonance linewidths $\delta f \simeq$ 250 MHz, generating a biphoton frequency comb.

As our time- and frequency-bins exceed the Fourier limit (ΔfΔt = 2280, $\delta f \Delta t = 1.5$), our time-frequency entangled photons can be considered hyper-entangled—that is, entangled in two fully separable DoFs. The signal and idler photons from the first three comb line pairs are then selected and separated with a commercial pulse shaper, as shown in Fig. 2.2. Now that the time bins and frequency bins are all generated in the state preparation stage, the idler photons are sent to a single-photon detector for heralding, and the signal photons are what carry the two qudits in the three time bins $\{|0\rangle_t, |1\rangle_t, |2\rangle_t\}$ and frequency bins $\left\{|0\rangle_f, |1\rangle_f, |1\rangle_f\right\}$. This procedure lets us prepare any time-bin/frequency-bin product state $|m\rangle_t |m\rangle_f$ $(m, n = 0, 1, 2)$ of the full computational basis set. In principle, we could also herald arbitrary time-frequency superposition states in this setup, by first sending the idler photon through a combination of time- or frequency-bin interferometers prior to detection in the temporal and spectral eigenbases. This more general case would permit the preparation of any two-qudit state and is an important area for further research.

To implement the SUM gate, the time bins associated with $|0\rangle_f$ are not delayed, the time bins associated with $|1\rangle_f$ experience a cyclic shift by 1 slot, and the time bins corresponding to $|2\rangle_f$ go through a cyclic shift of 2 slots. To delay the time bins dependent on their frequencies, we induce a dispersion of -2 ns/nm on the photons using a chirped fiber Bragg grating (CFBG); this imparts 6-ns (1-bin) and 12-ns (2-bin) delays for the temporal modes of $|1\rangle_f$ and $|2\rangle_f$, respectively, as required for the SUM operation. However, this delay is linear—not cyclic—so that some of the time bins are pushed outside of the computational space, to modes $|3\rangle_t$ and $|4\rangle_t$. To return these bins to overlap with the necessary $|0\rangle_t$ and $|1\rangle_t$ slots, we use a 1×2 MZM which permits access to both interferometer outputs. Accordingly this MZM is in principle lossless—as required for a unitary operation. (In practice, of course, insertion loss reduces throughput, but it should be possible in the future to significantly reduce this loss through, e.g., on-chip integration.) The two arms of

the interferometer have different path-dependent delay, returning the delayed time-bin to the computational space. Subsequently, another 1×2 MZM, operated in reverse, can be used to recombine the time bins deterministically as well. However, due to lack of equipment availability, in this proof-of-principle experiment we employ a 2×2 fiber coupler for recombination, which introduces an additional 3 dB power penalty. A pulse shaper is then used to route a frequency bin for detection using gated InGaAs single photon detectors (Aurea Technologies SPD-AT-M2). To measure the arrival times of the photons on the single-photon detectors, the time interval analyzer (PicoQuant HydraHarp 400) is used. The synchronization signal as well as the signals applied to the intensity modulators and phase modulator, are generated by an electronic arbitrary waveform generator (Tektronix AWG7122B) and adjusted to the proper level by linear amplifiers. The measured transfer matrix is shown in Fig. 2.3. The fact that this SUM gate is implemented with qudits in a single step potentially reduces the complexity and depth of quantum circuits in algorithms that require an addition operation [67].

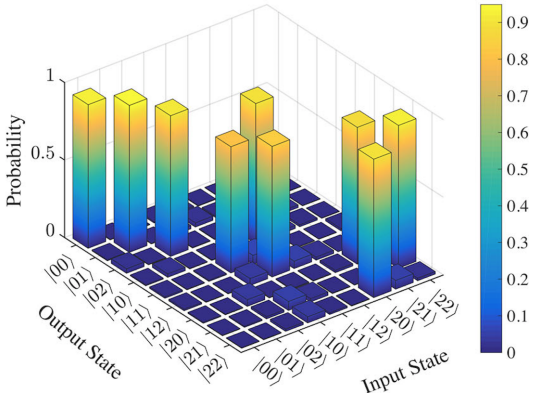

Fig. 2.3. The experimental transformation matrix of the SUM gate. The accidentals were subtracted in the transformation matrices, and the coincidence to accidentals ratio was $\sim$3.

To show the ability of our design to operate on large Hilbert spaces, we extend the dimensions of our qudits and encode two 16-dimensional quantum states in the

time and frequency DoFs of a single photon. For this demonstration, as we want to use more time bins and set a smaller frequency spacing between modes, we use a periodically poled lithium niobate (PPLN) crystal as a broadband source of time-frequency entangled photons followed by a programmable pulse shaper to set the frequency spacing and linewidth, instead of a microring with fixed frequency spacing. (We note that, in principle, one could still use an integrated source for these experiments by appropriately engineering a microrings FSR, bandwidth, and resonance linewidth to realize spectral and temporal spacings tighter than the integrated photon sources currently available to us.) In this experiment, we first shine a 773 nm CW laser on the PPLN crystal, generating entangled photons with a bandwidth of 5 THz. We then carve 16 time bins with a full width at half maximum of 200 ps and 1.2 ns spacing between them, to generate the time-bin qudits. Then, a pulse shaper is used to carve out the frequency of these entangled photons to generate sixteen 22 GHz wide frequency bins on both the signal and idler side of the spectrum, each spaced by 75 GHz from each other. Now that we have 16-dimensional qudits in both time and frequency, we send a heralded signal photon into the same SUM-gate structure. We note that after the CFBG, the individual time bins will spread to 300 ps due to their now larger (22 GHz) linewidth. While not necessary in this proof-of-principle experiment, such spreading could be reduced either by using a smaller linewidth for our frequency modes (e.g., with a Fabry-Perot etalon), or by using a dispersive element with a step-wise frequency-dependent delay profile [68–70]. To verify the operation, we send in different input two-qudit states, chosen from one of 256 basis states, and measure the output after the gate. While this yields a total of 256×256 (2^{16}) computational input/output combinations to test, we have no active frequency-shifting elements in the SUM gate to leak 75 GHz-spaced frequencies into each other, so we make the reasonable assumption that the frequency qudit remains unchanged through the operation. This is also enforced by the high extinction ratio of the pulse shaper ($\sim$40 dB), which blocks unwanted frequency bins as evident in Fig. 2.3). This allows us to focus on results in the sixteen 16×16 transfer matrices

measured in Fig. 2.4a-p (a subset with a total of 2^{12} input/output combinations). In each matrix, 16 different inputs with the same frequency and different time bins are sent into the SUM gate and the output time bins are measured. For this experiment, we use superconducting nanowire single photon detectors (SNSPDs), which allow us to report our data without accidental subtraction.

2.3.1 Gate fidelity

To assess the performance of our two-qudit quantum gates, we first focus on the computational-basis fidelity $\mathcal{F}_C$—one example of a so-called classical fidelity in the literature [71]. Defining $|n\rangle$ $(n = 0,\ 1,\ \ldots,\ N-1)$ as the set of all computational basis states and $|u_n\rangle$ as the corresponding output states for a perfect operation, we have the fidelity

$$\mathcal{F}_C = \frac{1}{N}\sum_{n=0}^{N-1} p(u_n|n) \tag{2.1}$$

where $p(u_n|n)$ is the probability of measuring the output state $|u_n\rangle$ given an input of $|n\rangle$. In the operations considered here, the ideal output states $|u_n\rangle$ are members of the computational basis as well, so there is no need to measure temporal or spectral superpositions in determination of $\mathcal{F}_C$. Given the measured counts, we retrieve the N conditional probability distributions via Bayesian mean estimation (BME) [72, 73] where our model assumes that each set of count outcomes (after accidentals subtraction) follows a multinomial distribution with to-be-determined probabilities; for simplicity, we take the prior distributions as uniform (equal weights for all outcomes). We then compute the mean and standard deviation of each value $p(u_n|n)$ and sum them to arrive at $\mathcal{F}_C$. Specifically, if $C_{u_n|n}$ signifies the counts measured for outcome u_n, and $C_{tot|n}$ the total counts over all outcomes (both for a given input state $|n\rangle$), BME predicts:

$$p\left(u_n|n\right) = \frac{1+C_{u_n|n}}{N+C_{tot|n}} \pm \sqrt{\frac{1+C_{u_n|n}}{\left(N+C_{tot|n}\right)^2}\frac{N+C_{tot|n}-C_{u_n|n}-1}{N+C_{tot|n}+1}} \tag{2.2}$$

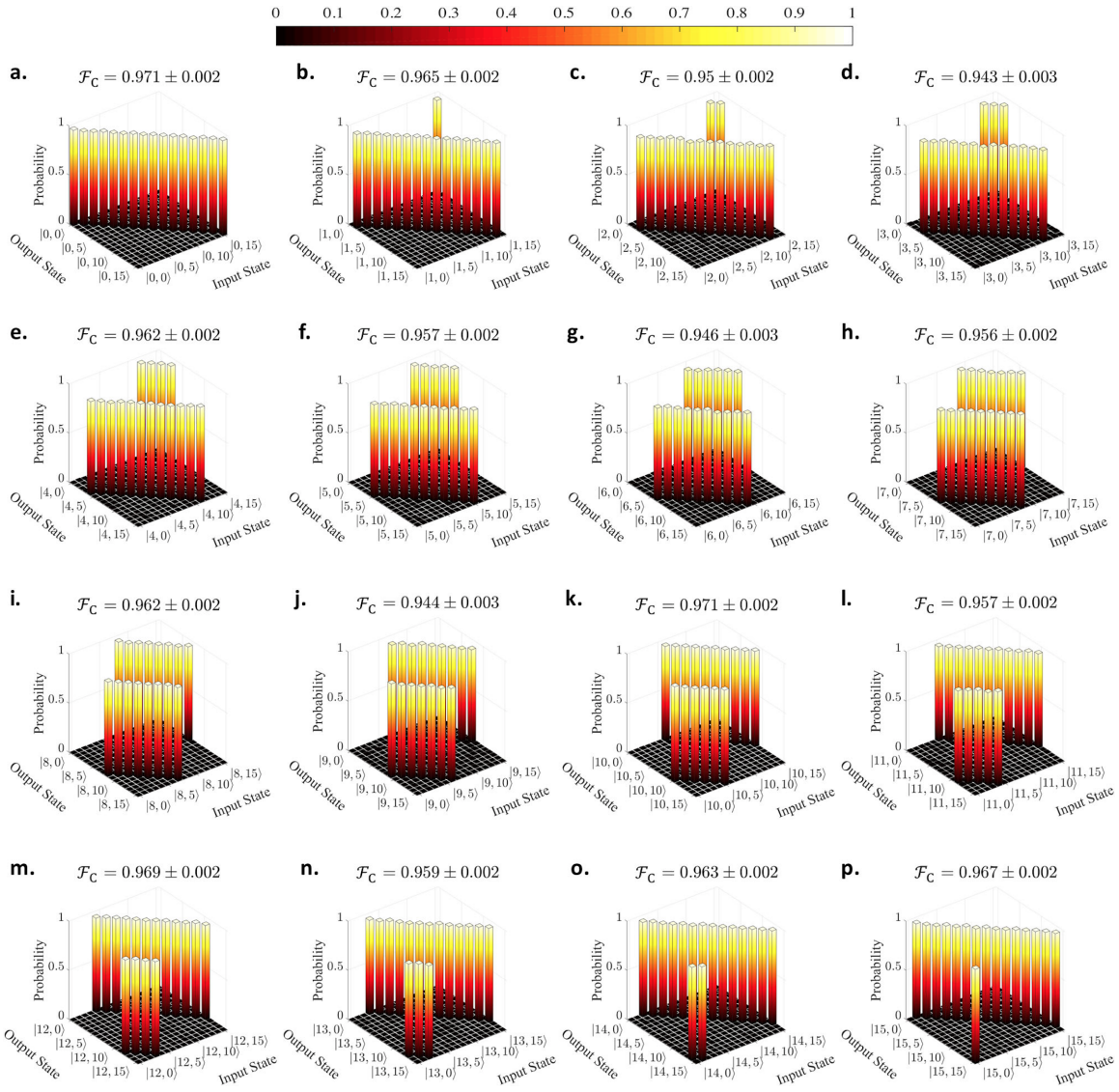

Fig. 2.4. 16×16 SUM gate. a-p) The transfer matrices corresponding to each possible time-bin output for each individual input time bin. Each matrix is specified for one frequency input, where the matched frequency output for different time bins is measured. In $|m, n\rangle$ on the x and y axis, m indicates the frequency qudit and n is the time bin qudit. The computational space fidelity of each matrix is shown on top of it. Subtraction of accidentals is not employed

where the standard deviation in the estimate is used for the error. Since the probabilities here each actually come from N different distributions, we estimate the total

error in $\mathcal{F}_C$ by adding these constituent errors in quadrature. Explicitly, we find 0.92 ± 0.01 for the 3×3 SUM gate. For the 16×16 SUM gate, the average computational space fidelity for the whole process, with the assumption that frequencies do not leak into each other, can be calculated as $\bar{\mathcal{F}}_C = 0.9589 \pm 0.0005$, which shows the high performance of our operation. This high fidelity benefits greatly from the high extinction ratio of the intensity modulator used to carve the time bins ($\sim$25 dB).

As seen by the presence of N in the denominator of Eq. 2.2, even when $C_{u_n|n} = C_{tot|n}$, the estimate $p(u_n|n)$ is not unity unless $C_{tot|n} \gg N$. In our experiments, the two-qudit tests have only $\sim 100 - 300$ total counts per input computational basis state for the 9×9 matrices (with N=9) and $\sim 500 - 800$ counts per input state for the 16×16 matrices (with N=16), thereby effectively bounding the maximum $p(u_n|n)$ and, by extension, fidelity $\mathcal{F}_C$. This behavior is actually a strength of BME, though, as it ensures that we have a conservative estimate of the fidelity that is justified by the total amount of data acquired [72].

2.3.2 SUM gate coherence

To show the coherence of our SUM gate, we generate an input state in the signal photon which is in time-bin $|0\rangle_t$ and an equi-amplitude superposition in frequency $|\psi\rangle_{in} = \frac{1}{\sqrt{3}}\left(|0\rangle_f + |1\rangle_f + |2\rangle_f\right)|0\rangle_t$. After passing this state through the SUM gate, the time-bin state of the photon is shifted based on the frequency, leaving us with a maximally non-separable state $|\psi\rangle_{out} = \frac{1}{\sqrt{3}}\left(|00\rangle_{ft} + |11\rangle_{ft} + |22\rangle_{ft}\right)$. We note that since we are starting with time-bin zero, the time bins will not fall out of the computational space; therefore, the interferometric structure is not needed for the SUM gate and a dispersion module alone can do the operation. This saves us the extra insertion loss of the interferometer, which is an important parameter due to the low photon pair rate on the detectors in this particular experiment.

To measure the 3-dimensional non-separability in $|\psi\rangle_{out}$, we must vary the phases of different signal frequency bins and time bins with a pulse shaper and phase mod-

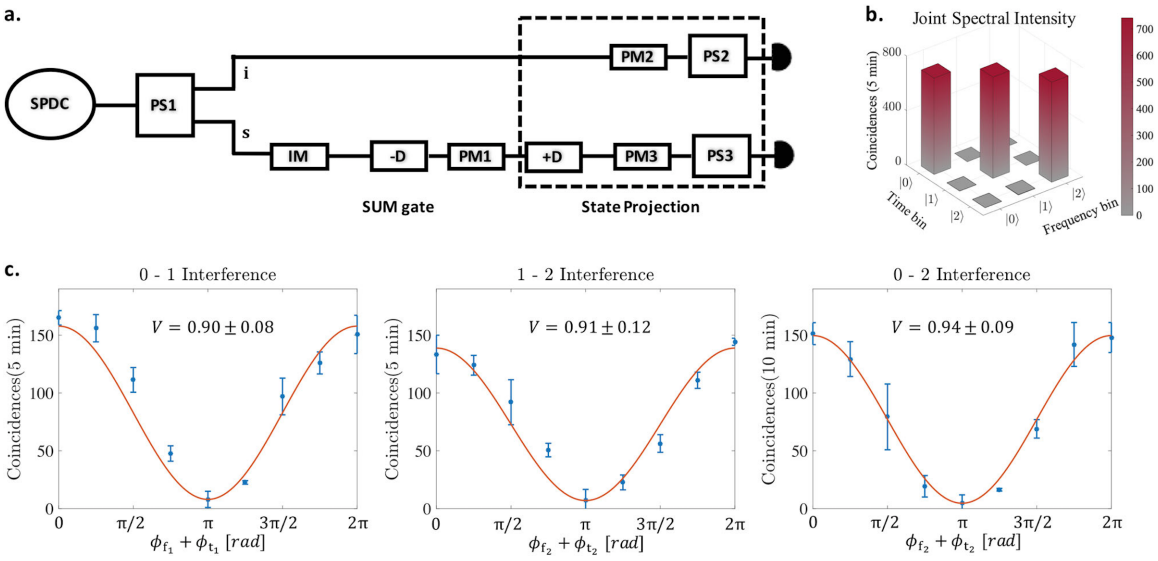

Fig. 2.5. Measurement of a three-dimensional maximally nonseparable time-frequency state. a) The experimental setup. SPDC spontaneous parametric down conversion, PS pulse shaper, IM intensity modulator, D and -D dispersion modules with $+2\ ns \cdot nm^{-1}$ and $-2\ ns \cdot nm^{-1}$, respectively, PM phase modulator. The same time-bin and frequency-bin spacings (1.2 ns, 75 GHz) as the 16-dimensional SUM gate experiment are used for these measurements. We note that in this experiment, the IM was placed only on the signal photons route to avoid its insertion loss on the idler photons. b) Joint spectral intensity of the three-dimensional nonseparable state. The accidentals were subtracted in this measurement, with a coincidence to accidentals ratio of about 30. c) Two-dimensional interference patterns showing the coherence between all three time-frequency modes of the state. The frequency-bin and time-bin phases are varied using PS1 and PM1, respectively. Both phases are swept together from 0 to π, for a total phase sweep from 0 to 2π. The data are shown with accidentals subtracted and coincidence to accidentals ratio of about 1. Since projection of frequency bins 0 and 2 on an indistinguishable frequency bin undergoes more projection loss, the coincidences between modes 0 and 2 were measured in 10 min

ulator, respectively. To observe the effect of this phase sweep with our relatively slow single-photon detectors (with $\sim$ 100 ps jitter), an indistinguishable projection of all three time bins and frequency bins should be created. In general, the time bins

can be projected on an indistinguishable state by using a cascade of interferometers. However, in our specific experiment, it is simpler to use a dispersion module with opposite dispersion to that of the module used in the SUM gate to perform the same projection. The frequency bins are then projected on an indistinguishable state using a phase modulator and pulse shaper to mix the frequencies (Fig. 2.5a)—a technique used previously in [33]. We note that our measurements on the signal photons are conditioned on heralding by idler frequency superposition states. To measure the interference between different signal frequency bins, the idler photons too have to be projected on an indistinguishable frequency bin using a phase modulator and pulse shaper (Fig. 2.5a). This projection guarantees that detection of an idler photon does not give us any information on the frequency of the signal photon. Here the phases of the idler frequency bins are held constant; only the phases of the signal frequency and time bins are varied. This is in contrast to experiments in [33], where the phases of both signal and idler frequency bins were varied.

In our experiment, three-dimensional interference measurements were not possible since mixing all three frequencies together adds extra projection loss, which we cannot afford. Therefore, we vary the phases of different time bins and frequency bins to measure two-dimensional interference patterns between all three time bins and frequency bins (Fig. 2.5c). Using the visibilities of these interference patterns along with a joint spectral intensity (JSI) measurement (Fig. 2.5b) can give us a lower bound on the amount of non-separability present in our system by measuring entanglement of formation [74, 75]. The JSI denotes the correlations between the time bins and frequency bins of a signal photon heralded by an idler photon in its computational basis. This measurement was done using the same experimental setup used in Fig. 2.5a without the equipment used for sweeping the phase of different signal time bins and projection measurements. For this measurement, the idler photons were detected after PS1, and the signal photons were detected right after the SUM gate.

Having the JSI measurement and the two-dimensional interference visibilities in hand, we have all the data needed to calculate the entanglement of formation with the assumption of having only white noise in our system, which can be expressed as:

$$E_{of} \geq -\log_2\left(1 - \frac{B^2}{2}\right) \tag{2.3}$$

where

$$B = \frac{2}{\sqrt{|C|}}\left(\sum_{(j,k)\in C} |\langle j,j|\,\rho\,|k,k\rangle| - \sqrt{\langle j,k|\,\rho\,|j,k\rangle\langle k,j|\,\rho\,|k,j\rangle}\right)_{j<k} \tag{2.4}$$

Here, C is the number of indices (j,k) used in the sum. This measurement is useful when we do not have access to all the elements of the density matrix. $\langle j,j|\,\rho\,|k,k\rangle$ $(j \neq k)$ elements indicate the coherence between modes j and k, and can be lower-bounded using the two-dimensional visibilities. The terms $\langle j,k|\,\rho\,|j,k\rangle$ can be calculated using the elements of the JSI. Using these values, we measure $E_{of} \geq 1.19 \pm 0.12$ ebits, which indicates greater than two-dimensional non-separability in our two-party system, more than one standard deviation away from the threshold.

2.4 Four-Party Two-Photon Greenberger-Horne-Zeilinger State

The demonstrated SUM gate can also be used to produce high-dimensional GHZ states [76]. GHZ states consist of more than two parties, entangled with each other in a way that measurement of one party in the computational basis determines the state of all the other parties [77]. It has been only recently that these states were demonstrated in more than two dimensions, where a three-dimensional three-party GHZ state was realized using the orbital angular momentum of optical states [76]. Here, we take advantage of our SUM gate and the large dimensionality of time-frequency states to generate a four-party GHZ state with 32 dimensions in each DoF.

To generate the 32-dimensional four-party GHZ state, the signal and idler go through the same dispersion module (-2 ns/nm). After dispersion, the signal frequency bins farther away from the center of the spectrum are delayed more, but the idler frequency bins are delayed less as we move farther away from the center. In

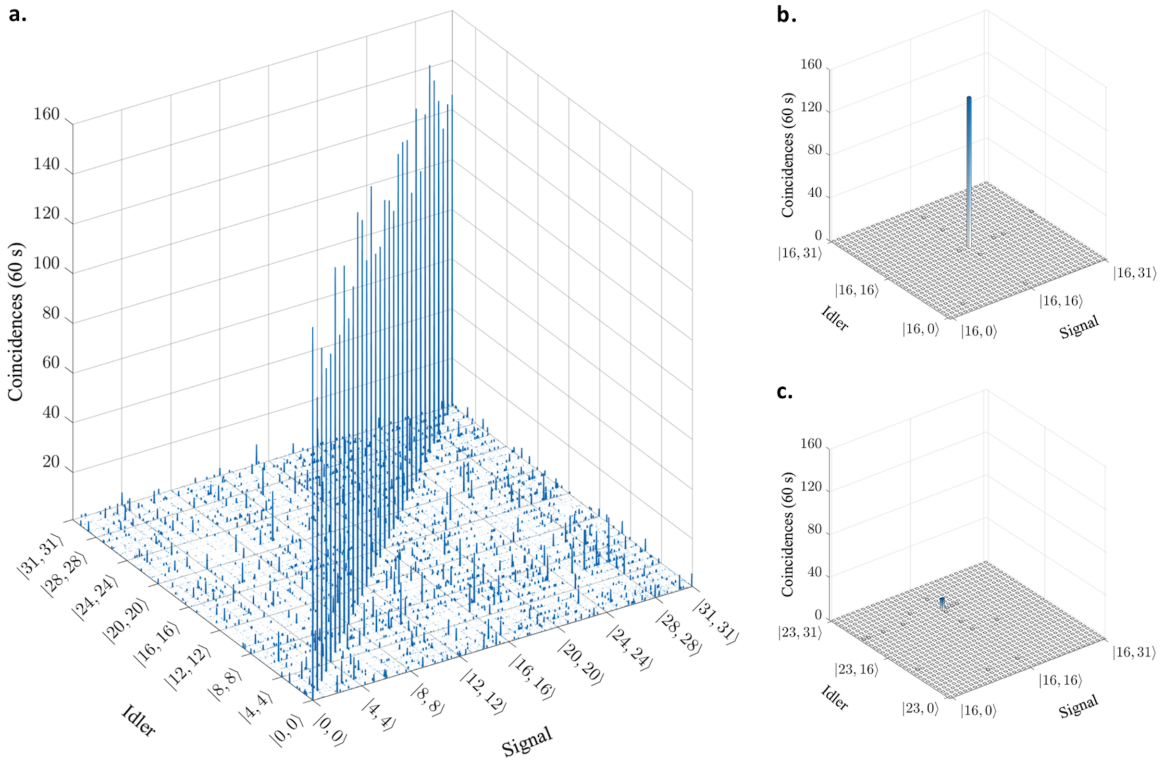

Fig. 2.6. a) Measurement of the four-party 32-dimensional GHZ state in the computational basis. The states $|m, n\rangle$ shown on the signal and idler axes correspond to frequency-bin m and time-bin n. The large coincidence peaks exist only for states with the same time-bin and frequency-bin indices for both signal and idler (32 peaks). b), c) Zoomed-in 32×32 submatrices of the matrix shown in a. Each submatrix shows coincidences for different signal and idler time bin indices for fixed signal and idler frequency bin indices. b) Matched signal and idler frequency bins: large peak is observed for $|16, 16, 16, 16\rangle_{f_s t_s f_i t_i}$. c Unmatched signal and idler frequency bins. The small peak evident at $|16, 16, 23, 23\rangle_{f_s t_s f_i t_i}$ reflects additional counts from multiphoton pair events at the time bins to which frequency bins $|16\rangle_{f_s}$ and $|23\rangle_{f_i}$ are shifted. The data are shown with accidentals subtracted (coincidence to accidentals ratio of $\sim$4)

order to write the GHZ state in the form $|\psi\rangle_{out} = \frac{1}{\sqrt{32}} \sum_{m=0}^{31} |m, m, m, m\rangle_{f_s t_s f_i t_i}$, we label the signal time bins after dispersion 0 to 31 starting from earlier time bins (time bin 0 the earliest, time bin 31 the latest), while on the idlers, we label the time bins

such that the earliest time bin is 31 and the latest time bin is 0. Another choice would be to send signal and idler through separate modules with equal but opposite dispersion, in which case we would use identical time labeling. The latter choice, however, requires adding pulse shapers before the SNSPDs to selectively route frequency bins. The added pulse shapers insertion loss would not allow measuring the state within a reasonable time-frame. To measure the state illustrated in Fig. 2.6, we individually measured coincidences for the 32 different settings of both signal and idler frequency bins (32×32 measurements). For each of these measurements, we operate the event timer in the Time-Tagged Time-Resolved mode, and assign signal and idler time bins for each coincidence, which results in a 32×32 submatrix for each signal-idler frequency setting. Therefore, we have 32^4 measurements in total. Two of the 32×32 time-bin submatrices are shown in Fig. 2.6 b-c.

We start from the state $|\psi\rangle_{in} = \frac{1}{\sqrt{32}} |0,0\rangle_{t_s t_i} \sum_{m=0}^{31} |m,m\rangle_{f_s f_i}$, which means both signal and idler photons are initialized in the first time-bin state and are maximally entangled in the frequency domain. Then, we operate deterministic SUM gates separately on both signal and idler photons, resulting in a four-party GHZ state of the form $|\psi\rangle_{out} = \frac{1}{\sqrt{32}} \sum_{m=0}^{31} |m,m,m,m\rangle_{f_s t_s f_i t_i}$. Since the initial state only consists of the zeroth time bins, the dispersion module does not shift any of the bins outside of the computational space; hence the interferometric structure used in the full SUM gate is not required when operating within this subspace. The GHZ state is measured in the computational basis (Fig. 2.6); the plot contains coincidences for all basis states in the set $|m,n,k,l\rangle_{f_s t_s f_i t_i}$; $0 \leq m,n,k,l \leq 31$. Only states whose four qudits match (i.e., $|m,m,m,m\rangle_{f_s t_s f_i t_i}$) have high counts, as expected for a GHZ state. Of course, full characterization of the state requires measurements in superposition bases as well [78], but due to the additional insertion loss associated with superposition measurements in time and frequency using interferometers and phase modulators, respectively, we were unable to measure such projections. Remarkably, the demonstrated GHZ state resides in a Hilbert space equivalent to that of 20 qubits, an impressive 1,048,576 $\left(32^4\right)$ dimensions. We emphasize that the four parties of the

demonstrated GHZ state are carried by only two photons, and hence cannot be used for genuine multi-partite GHZ applications such as demonstration of Bells theorem without inequalities [77], quantum secret sharing [79], or open-destination teleportation [80]. However, the realization of such high-dimensional GHZ states indicates the potential of our time-frequency platform for quantum technologies such as near-term quantum computation and cluster-state generation [70, 81].

In our experiments, we use bulk switches, dispersion modules, pulse shapers and phase modulators which have high insertion loss (switch: 3 dB, dispersion module: 3 dB, pulse shaper: 5 dB, phase modulator: 3 dB). Therefore, we use very bright entangled photons at the input in order to have reasonable coincidence counts on our detectors in our acquisition time. Using bright biphotons gives rise to multi-pair generation which leads to the relatively high accidental rate here.

2.5 Conclusion

High-dimensional optical states [33, 82–85] can open the door to deterministically carry out various quantum operations in relatively large Hilbert spaces [86], as well as enable higher encoding efficiency in quantum communication protocols such as quantum key distribution [87] and quantum teleportation [63, 88]. We have demonstrated deterministic single- and two-qudit gates using the time and frequency degrees of freedom of a single photon for encoding—operating on up to 256 (2^8)-dimensional Hilbert spaces—and carried out these gates with high computational-space fidelity. We have shown the application of such two-qudit gates in near-term quantum computation by using them to realize a GHZ state of four parties with 32 dimensions each, corresponding to a Hilbert space of more than one million modes. Such deterministic quantum gates add significant value to the photonic platform for quantum information processing and have direct application in, e.g., simulation of quantum many-body physics [45, 89, 90].

3. QUANTUM PHASE ESTIMATION USING QUDITS

3.1 Introduction [1]

Given a unitary U and its eigenstate $|\psi\rangle$ such that $\hat{U} = e^{i2\pi\phi}|\psi\rangle$, how can one extract the eigenphases (i.e. phases associated with the eigenvalues)? This essential problem was addressed by phase estimation algorithm (PEA), which is now a critical building block that allows quantum speedup in touted quantum algorithms such as Shor's factoring algorithm, the Harrow-Hassidim-Lloyd (HHL) algorithm for solving linear systems of equations [92, 93], and is used for finding the ground-state energy of a molecular Hamiltonian [94–97].

Experimental demonstrations of the PEA were performed on different platforms including photonic [98, 99] and superconducting transmons [100]. These demonstrations were based on a qubit (two-level) system. Scaling the problems Hilbert-space dimension requires increasing the number of interacting qubits (width), which entails an increase in the length of the gate sequence (depth), all of which is experimentally limited in current platforms due to noise, loss, and decoherence. Shifting to high-dimensional quantum states and high-dimensional multi-valued logic gates can potentially provide a reduction in both the depth and width of the quantum circuit.

In this chapter, we build on the concepts developed in chapter 2 to realize a proof-of-principle qudit-based PEA on a photonic platform by encoding two qutrits in a single photon, where the frequency DoF carries one qutrit as the control register, and the time DoF carries another qutrit as the target register. We test our qutrit-based implementation on a diagonal 3×3 unitary matrix performing two measurements, one with a unitary having eigenphases that match the phase markers of the implemented PEA, and a second unitary that with non-matching eigenphases. Using the photon

[1] The results in this chapter are adapted in whole or part from the publication [91]

statistics, we fit the measurements to the theoretical distribution to retrieve the phase within an error equal to or less than 7.1% .

3.2 Theory and Concept

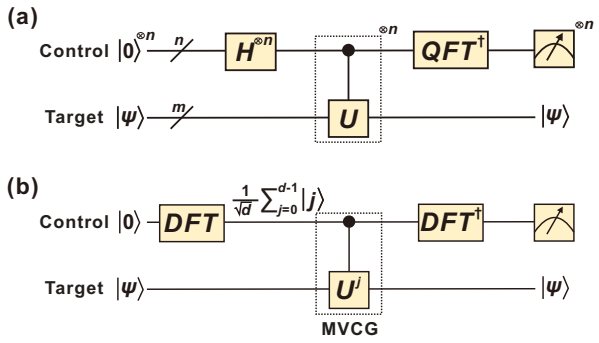

Fig. 3.1. (a) Schematic for a general qubit-based PEA using n-qubit control and m-qubit target states. $H^{\otimes n}$ is a set of Hadamard gates acting on n qubits in parallel. U is a unitary operator operating on the target state. n control-U gates, one for each control rail, are present. $QFT^{\dagger}$ is the inverse quantum Fourier transform on the n-qubit control register. (b) Schematic for a single-qudit-based PEA. d-point discrete Fourier transform (DFT) is a Hadamard gate generalized to d-dimensional state (See Eq. (3.4)). A multi-value-controlled-gate (MVCG) applies $\hat{U}^j$ to the target when the control is in the $|j\rangle$ state.

The PEA diagram is illustrated in Figure 3.1(a) where the top rail is the control register, and the bottom rail is the target register with an input $|\psi\rangle$ which is an eigenstate of a unitary operator $\hat{U}$. The dimension of the target register defines or limits the Hilbert-space dimension of the problem of interest, while the control registers set the precision of the retrieved phase [101]. Using n d-dimensional qudits for the control register, the phase ϕ can be evaluated with a precision of $2\pi/d^n$. A Hilbert space of dimension $N = 2^m = d^n$ can be represented either by m qubits ($d = 2$) or n qudits ($d > 2$), therefore, a qudit-based PEA represents the same ψ with a $\log_2(d)$ reduction of the circuit width (number of qudits).

For a qubit based operation, the algorithm procedure can be summarized as follows: Using an eigenstate $|u\rangle$, a black box performing a controlled U^j operation, and n control qubits, we start with the circuit in an initial state of $|0\rangle |u\rangle$. The Hadamard gates create a superposition of the control register

$$\rightarrow \frac{1}{\sqrt{2^n}} \sum_{j=0}^{2^n-1} |j\rangle |u\rangle \tag{3.1}$$

subsequently, we apply the controlled-U^j operation which attaches the phase to the control qubits

$$\rightarrow \frac{1}{\sqrt{2^n}} \sum_{j=0}^{2^n-1} |j\rangle U^j |u\rangle = \frac{1}{\sqrt{2^n}} \sum_{j=0}^{2^n-1} e^{2\pi i j\phi} |j\rangle |u\rangle. \tag{3.2}$$

The final stage applies an inverse quantum Fourier transform (QFT), where the QFT is defined as a linear operator performing the following transformation

$$|j\rangle \rightarrow \frac{1}{\sqrt{2^n}} \sum_{j=0}^{2^n-1} e^{2\pi i j\phi} |j\rangle |u\rangle. \tag{3.3}$$

Measuring the output state of the first register after the inverse QFT gives $|\hat{\phi}\rangle |u\rangle$ where the state $|\hat{\phi}\rangle$ is an estimate of ϕ. For a more detailed description and analysis of success probability and error, we refer the reader to [101].

Qudit-based PEA

The quantum circuit for a qudit based PEA [102] generalizes the two-value controlled-$\hat{U}$ gate for the qubit case to a multi-value-controlled-gate (MVCG) that applies $\hat{U}^j$ to the target register when the control register is in the $|j\rangle$ state ($j = 0, 1, ..., d-1$). The functionalities of the n two-qubit controlled gates utilized in the conventional qubit-based PEA circuit [101] can be realized with a single MVCG having 2^n controlled values, thus reducing the depth of our PEA circuit.

Figure 3.1(b) shows the schematic of a qudit-based PEA. The DFT gate here is a d-point discrete Fourier transform (DFT) defined as $DFT^{(d)} |j\rangle = \frac{1}{\sqrt{d}} \sum_{k=0}^{d-1} e^{2\pi i(jk/d)} |k\rangle$. The DFT gate can be understood as a qudit generalization of the Hadamard gate to dimensions beyond $d = 2$ [35, 103]. When operating on a single qudit, both the Hadamard gates and the QFT in Figure 3(a) are reduced to a single DFT gate. We

would like to emphasize that, in this work we use the "DFT" to denote a *single*, high-dimensional gate capable of applying the discrete Fourier transform to a single qudit state, while the "QFT" denotes the standard quantum algorithm of applying the discrete Fourier transform to a multi-qubit state. Different from the DFT, the QFT often requires a sequence of single-qubit and two-qubit gates to implement. The MVCG then applies $\hat{U}^j$ on the target state conditional on the control state $|j\rangle$ (i.e., $|j\rangle|\psi\rangle \rightarrow |j\rangle \hat{U}^j |\psi\rangle$). Finally, the phase kickback mechanism in the PEA [101] allows us to evaluate the ϕ by applying an inverse DFT on the control register and performing measurements in the computational basis. The quantum circuit can deterministically evaluate the eigenphase ϕ for each eigenstate of $\hat{U}$, insofar as ϕ can be written exactly with the given precision. Instead, if the input state is in a superposition of eigenstates, performing measurements on the control register yields probabilistic results, and one can obtain the correct statistics of ϕ. As a proof-of-concept implementation, here we limit our dimension to $d = 3$ (qutrit) for both the control and target registers, capable of retrieving the eigenphase of a given three-dimensional unitary with $2\pi/3$ precision. We introduce the three-point DFT gate in its matrix form,

$$DFT^{(3)} = \frac{1}{\sqrt{3}} \begin{pmatrix} 1 & 1 & 1 \\ 1 & e^{2\pi i/3} & e^{4\pi i/3} \\ 1 & e^{4\pi i/3} & e^{2\pi i/3} \end{pmatrix}. \tag{3.4}$$

and the unitary ($\hat{U}_1$) of interest in our first demonstration is simply a Pauli-Z gate generalized to the qutrit space:

$$\hat{U}_1 = \begin{pmatrix} 1 & 0 & 0 \\ 0 & e^{2\pi i/3} & 0 \\ 0 & 0 & e^{4\pi i/3} \end{pmatrix} \tag{3.5}$$

where the eigenphases 0, $2\pi/3$, and $4\pi/3$ can be exactly represented with a single ternary digit expansion.

3.3 Experimental Results

In this experiment, we leverage the well-established techniques and fiber-optic components developed for optical communication and wavelength division multiplexing to create and manipulate high dimensional quantum states for PEA implementation. Figure 3.2(a) provides a schematic of the setup, which can be decomposed into three stages: state preparation, high-dimensional controlled operation, and measurement on the control qudit.

To prepare an equi-amplitude superposition of frequency qutrit as the control register, we send a continuous-wave (CW) laser source operating in the C-band through a phase modulator (PM1) driven at 18 GHz, which creates a total number of $\sim$10 frequency bins with a spacing of 18 GHz. Subsequently, a pulse shaper (PS1) is programmed to filter out all but three equi-amplitude frequency bins, now with a frequency spacing (Δf) of 54 GHz. Note that since the controlled gate in our proposed setup is a one-photon operation, the input photon number statistics have no impact on the operation, thus coherent states can be used instead of true single photons as the input.

To prepare the target qutrit state, we employ an intensity modulator (IM) driven by an arbitrary waveform generator (AWG), and carve out three narrow time bins each with a 6 ns spacing, a 24 ns repetition period, and a full width at half maximum of $\sim$0.2 ns which broadens the frequency-bin line-width to 2.2 GHz. As our unitary matrix of interest (Eq 3.5) is diagonal, the target qutrit eigenstates are single time bins. Thus, we choose to treat each time bin as an independent eigenstate. Each experimental trial can be thought of as three separate measurements made in quick (6 ns) succession. Considering only one of the time bins (eigenstates) at a time, the state after the state preparation stage can be written as:

$$|\psi\rangle_{in} \propto \sum_{j=0}^{2} |j\rangle_f \otimes |\tau\rangle_t \tag{3.6}$$

where $\tau = \{0, 1, 2\}$ denotes which time bin is chosen to operate. The controlled gate itself consists of a phase modulator (PM2) sandwiched between two chirped

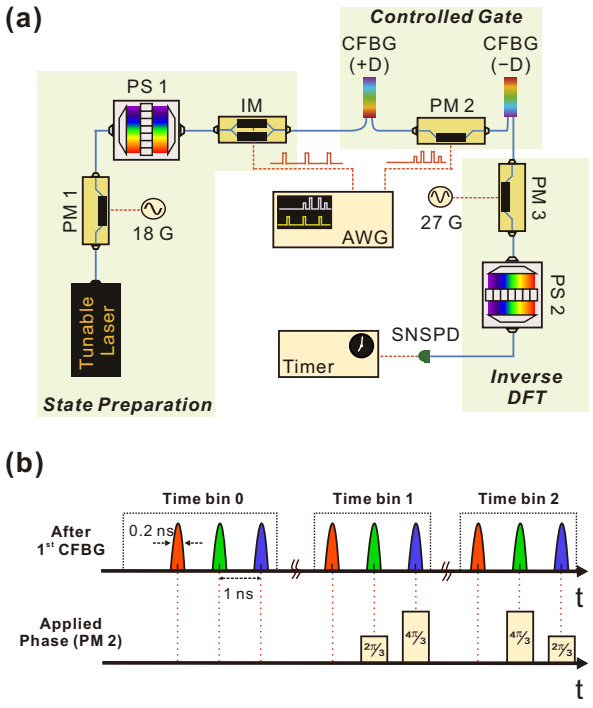

Fig. 3.2. (a) Experimental setup. (b) Implementation of controlled-phase gate. See text for details. (PM/IM: Electro-optic phase/intensity modulator; PS: Fourier-transform pulse shaper; CFBG: Chirped fiber bragg grating; SNSPD: Superconducting nanowire single-photon detector; AWG: Arbitrary waveform generator. Both radio-frequency oscillators (18 and 27 GHz) are synchronized to the 10 MHz reference clock of the AWG.)

fiber Bragg grating (CFBG). The first CFBG has a dispersion of 2 ns/nm imparting a frequency-dependent delay which splits each time bin into 3 daughter time bins, each of which corresponds to one frequency mode [red, green, and blue pulses in Figure 3.2(b)]. The spacing between daughter time bins (Δt) is 0.9 ns, which is larger than the time-bin coherence time ($\sim$0.2 ns) and its product with the frequency-bin spacing (54 GHz) exceeds the Fourier transform limit (i.e., $\Delta f \Delta t > 1$), allowing independent manipulation of the time and frequency DoFs. Using the AWG, we program the phase modulator to apply the unitary U^j defined in Eq. (3.5) to time-bin states conditional on the frequency-bin state $|j\rangle_f$. The second CFBG with an opposite dispersion of -2 ns/nm cancels the first dispersion module and recombines the three daughter time bins back into a single indistinguishable time bin. After the application of MVCG, we can obtain an output state

$$|\psi\rangle_{out} \propto \sum_{j=0}^{2} e^{\frac{i2\pi j\tau}{3}} |j\rangle_f \otimes |\tau\rangle_t \tag{3.7}$$

Note that the phases applied to the time-bin state are now attached to the control register, a process called "phase kickback."

An ideal three-point inverse DFT gate performs the following transformation:

$$\frac{1}{\sqrt{3}} \sum_{j=0}^{2} e^{\frac{i2\pi j\tau}{3}} |j\rangle_f \xrightarrow{DFT^{-1}} |\tau\rangle_f \tag{3.8}$$

and thus applying inverse DFT on the control state allows us to read out the phase based on the detection pattern in the logical basis. Detection in output state $|\tau\rangle_f$ indicates the retrieved phase $\tilde{\phi}$ equals to $2\pi\tau/3$ ($2\pi \times 0.\tau_3$ in ternary expression). Recently a near-deterministic, three-dimensional DFT for frequency-encoded qutrit has been demonstrated with near-unity fidelity, utilizing a quantum frequency processor circuit [104] consisting of two electro-optic phase modulators and one pulse shaper. Due to equipment availability, we elect to implement a simpler, probabilistic version of inverse DFT using a single phase modulator (PM3), capable of performing the equivalent functions in a multi-shot fashion. The control state, consisting of three frequency bins with 54 GHz spacing, is phase modulated by a 27 GHz sine waves

to create frequency sidebands. We fine-tune the modulation index to 1.843 rad such that each frequency bin projects onto the central bin $|1\rangle_f$ with equal probability. We utilize another pulse shaper (PS2) as a bandpass filter to pick out this overlapped bin, and then route to a superconducting nanowire single-photon detector (SNSPD) for measurement. Since the output now consists of projections from all three frequency bins, the measured counts will reflect the relative phases due to interference.

Given a control register in the state $\propto \sum_{j=0}^{2} |j\rangle_f$ (LHS of Eq. (3.8) when $\tau = 0$) as the input of the PM3, after frequency mixing we have maximum photon counts in the overlapped bin due to constructive interference. The other two orthogonal states will instead experience destructive interference and thus contribute no photon counts. This operation is equivalent to the transformation described in Eq. (3.8) for $\tau = 0$, namely the projection onto $|0\rangle_f$. We can also tune the delays between the input photons and the electrical drive on PM3, such that the other two transformations (Eq. (3.8) for $\tau = 1, 2$) can be achieved. Different delay settings can be achieved by introducing an additional pulse shaper prior to frequency mixing, or a radio-frequency phase shifter to impart the required delay. Here we choose to lump this function into PS1 in the state preparation stage to reduce the insertion loss and the complexity of the system. To avoid any confusion, hereon, we name the three delay settings required to realize the equivalent inverse DFT functions simply as "projection onto $|0\rangle_f$, $|1\rangle_f$ and $|2\rangle_f$", respectively.

Under each delay setting, we measure the photon counts in three time-bins recorded over 1 second. We note that these time bins are widely spaced and do not interfere, hence, this measurement can be considered as three independent measurements of each eigenstate in series. As shown in Eq. 3.7, the phase attached to the control register after the MVCG matches the inverse DFT transformation described in Eq. 3.8, thus we have

$$\sum_{j=0}^{2} e^{\frac{i2\pi j\tau}{3}} |j\rangle_f \otimes |\tau\rangle_t \xrightarrow{DFT^{-1}\otimes I} |\tau\rangle_f \otimes |\tau\rangle_t \tag{3.9}$$

which shows for time-bin $|\tau\rangle_t$ as the input target, ideally we will only obtain photon counts after projecting the control register onto $|\tau\rangle_f$. Figure 3.3(a) shows the exper-

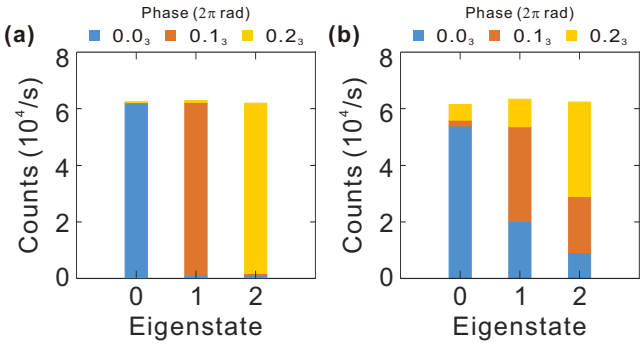

Fig. 3.3. Experimental results for implementing (a) $\hat{U}_1$ (Eq. 3.5), and (b) $\hat{U}_2$ (Eq 3.10). Color of the bars corresponds to number of photon counts registered after inverse DFT projection onto $|0\rangle_f$ (blue), $|1\rangle_f$ (red), and $|2\rangle_f$ (yellow). Photon counts are recorded over 1 second.

imental results for estimating the eigenphase of $\hat{U}_1$. For each target eigenstate, we stack three color-coded vertical bars in a single slot to represent the registered counts for different frequency projections. The total number of counts remain stable across three successive measurements, and most of the counts for eigenstate $|\tau\rangle_t$ are recorded after projection onto $|\tau\rangle_f$. The results match our prediction, as all three eigenphases for $\hat{U}_1$ can be represented with exactly one ternary digit, and thus the phase can be retrieved deterministically. The fidelity of this measurement, here defined as the ratio of photon counts registered at the correct output to the total number of received photons, is $98 \pm 1\%$.

For the second part of the experiment, we reprogram our MVCG operation by applying a different temporal phase mask imparted by the AWG to implement another unitary $\hat{U}_2$:

$$\hat{U}_2 = \begin{pmatrix} 1 & 0 & 0 \\ 0 & e^{i0.351\pi} & 0 \\ 0 & 0 & e^{i1.045\pi} \end{pmatrix}. \tag{3.10}$$

Note that two of the eigenphases are no longer integer multiples of $2\pi/3$, or namely, the phase attached onto the control frequency bins (after phase kickback mechanism)

does not match the inverse DFT to transform into a single logical state. Figure 3.3(b) shows the measured counts for all eigenstates under different inverse DFT settings. For the first eigenstate, its corresponding phase is 0 and hence most of the counts are still registered in $|0\rangle_f$. The other two eigenstates, as discussed above, possess phases that cannot be accurately retrieved given a single ternary digit precision, and thus the counts are distributed over different projections. Following the conventional PEA approach, we report the retrieved phase ($\tilde{\phi}$) based on the projection with the highest number of counts. For eigenphases ϕ equal to 0.351π and 1.045π, the corresponding $\tilde{\phi}$ are $2\pi/3$ and $4\pi/3$, respectively. In the following section, we will discuss whether more information can be extracted from the counts' distribution shown in Figure 3.3, given (i) the input state is already prepared in the eigenstate, and (ii) an ample amount of counts are registered for further analysis.

Phase retrieval of $\hat{U}_2$

When the input target register of a PEA circuit is an eigenstate with a corresponding eigenphase ϕ, the probability for the qutrit output control state to collapse to $|n\rangle$, where $n = \{0, 1, 2\}$, is

$$C(n, \phi) = \frac{1}{9}\left|1 + e^{i(\phi - \frac{n2\pi}{3})} + e^{i2(\phi - \frac{n2\pi}{3})}\right|^2. \tag{3.11}$$

All three $C(n, \phi)$, for $n = \{0, 1, 2\}$, are plotted in Figure 3.4. Observe that for each ϕ, the ordered set $\{C(0, \phi), C(1, \phi), C(2, \phi)\}$ is unique. Now let E_0, E_1, and E_2 be the measured, normalized ($\sum E_n = 1$) photon counts projected, respectively, onto $|0\rangle_f$, $|1\rangle_f$, and $|2\rangle_f$. The phase we estimate from our measurement, denoted $\tilde{\phi}$, is the phase which minimizes the mean squared error between the measured and theoretical probabilities:

$$\min_{\tilde{\phi}} \sum_{n=0}^{2} (E_n - C(n, \tilde{\phi}))^2 \tag{3.12}$$

The estimated phases for $\hat{U}_1$ (Eq. 3.5) and $\hat{U}_2$ (Eq. 3.10) are shown in Table 3.1. The results for $\hat{U}_2$ are plotted in Figure 3.4 alongside the three $C(n, \phi)$ curves of Eq. 3.11. The largest error in $\tilde{\phi}$ is 7.1%, and the error is less than 3% in all other cases. Our photonic system's ability to execute a large number of trials enables this statistical

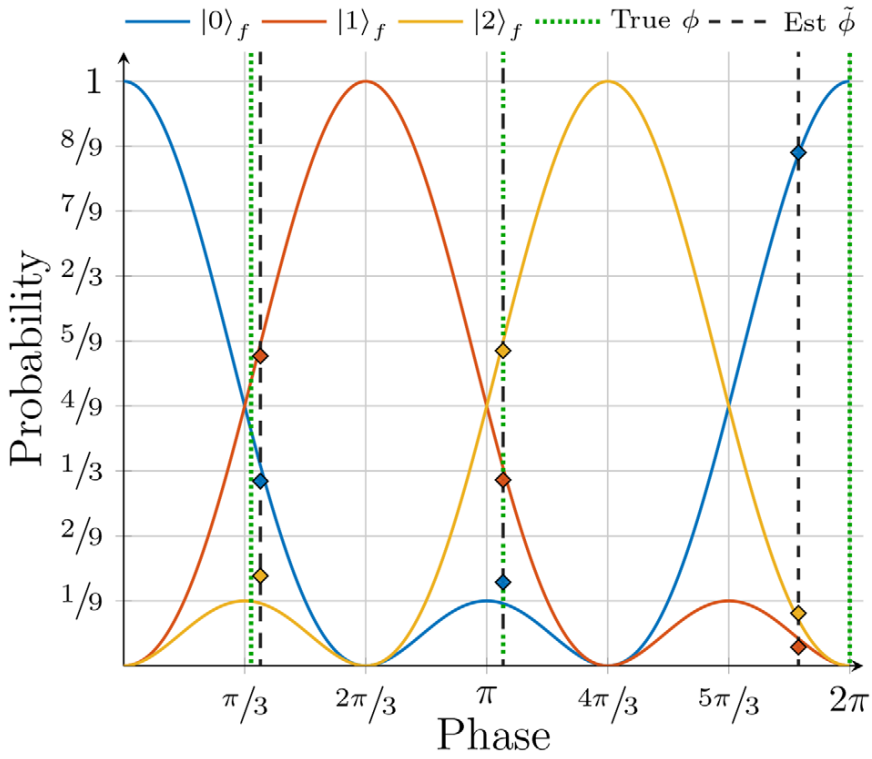

Fig. 3.4. The three curves represent the probability of the control qutrit collapsing to bin $|n\rangle_f$ for $n = \{0(\text{blue}), 1(\text{red}), 2(\text{yellow})\}$ for any eigenphase corresponding to the eigenstate input of a PEA circuit. The normalized experimental photon counts for all three eigenstates of $\hat{U}_2$ are fitted to – and plotted at – the estimated phase ($\tilde{\phi}$) which minimizes mean squared error (Eq 3.12). $\tilde{\phi}$ is denoted by the position of the markers and the black dashed line; the location of the true phase (ϕ) for each eigenstate is noted with a green dashed line. The curves are described by Eq 3.11; the plotted values can be found in Table 3.1.

approach to phase estimation. Agreement between estimated and true phase can be used to quantify the error in the experimental setup; however, because the statistical approach requires an eigenstate input, it should not be viewed as a standalone method for determining an unknown phase.

Table 3.1.
Normalized photon counts and comparison of true phase ϕ and experimentally estimated phase ϕ' for each eigenstate of $\hat{U}_1$ (Eq. 3.5) AND $\hat{U}_2$ (Eq. 3.10). Photon counts normalized from results in Figure 3.3.

$\hat{U}_1$			
Eigenstate	$\|\mathbf{0}\rangle_t$	$\|\mathbf{1}\rangle_t$	$\|\mathbf{2}\rangle_t$
$\boldsymbol{E_0}$	$.9948 \pm .0004$	$.0101 \pm .0004$	$.0122 \pm .0005$
$\boldsymbol{E_1}$	$.0023 \pm .0002$	$.9805 \pm .0009$	$.0120 \pm .0005$
$\boldsymbol{E_2}$	$.0029 \pm .0002$	$.0094 \pm .0004$	$.9758 \pm .0010$
True Phase, ϕ	0	$2\pi/3$	$4\pi/3$
Est. Phase, $\tilde{\phi}$	1.972π	$.612\pi$	1.394π
Error, $\frac{\lvert\phi-\tilde{\phi}\rvert}{2\pi}$	1.4%	2.7%	3.0%
$\hat{U}_2$			
Eigenstate	$\|\mathbf{0}\rangle_t$	$\|\mathbf{1}\rangle_t$	$\|\mathbf{2}\rangle_t$
$\boldsymbol{E_0}$	$.878 \pm .002$	$.316 \pm .003$	$.143 \pm .002$
$\boldsymbol{E_1}$	$.032 \pm .001$	$.530 \pm .003$	$.318 \pm .003$
$\boldsymbol{E_2}$	$.090 \pm .002$	$.154 \pm .002$	$.539 \pm .003$
True Phase, ϕ	0	$.3511\pi$	1.045π
Est. Phase, $\tilde{\phi}$	1.859π	$.377\pi$	1.045π
Error, $\frac{\lvert\phi-\tilde{\phi}\rvert}{2\pi}$	7.1%	1.3%	0.0%

3.4 Conclusion

In this chapter, we successfully demonstrate the first proof-of-principle qudit-based PEA implemented in a photonics-based platform. Using the time and frequency DoFs as the target and control register, respectively, we implement a deterministic two-qudit gate utilizing standard optical communication equipment. The large ensemble of measurements facilitated by the photonic platform enables the retrieval of eigenphases with an error equal to or less than 7.1% .

The current implementation of the MVCG can only perform trivial diagonal unitary operations, which is a major shortcoming in this demonstration. Nevertheless, a near-term path to implementing near arbitrary unitary operations using reasonable experimental resources is clear: using the time, path, or polarization DoF of a single photon as the control register, the frequency DoF can be reserved to the represent the target register, where now a more diverse set of unitaries can be implemented using a programmable quantum frequency processor [105]. The use of polarization as a control qubit offers simple implementation of projective measurements but limits the Hilbert-space dimension, thus the precision. Using an iterative PEA approach [106], the precision or accuracy can be arbitrarily increased.

Finally, to address interesting real-world problems, the biggest remaining challenge is to increase the dimension of the target's Hilbert-space. While a 32-dimensional SUM gate was demonstrated in chapter 2, we have no clear pathway to extend this to arbitrary unitaries. The most rational approach is to decompose this arbitrary d-dimensional unitary into a set of a qubit or qutrit-based operations that we can implement using the frequency DoF. Nevertheless, practical demonstrations are currently hindered by the loss of bulk equipment used to implement the gates. Advances in integrated photonics are key to realizing such an approach.

4. QUANTUM WALKS OF BIPHOTON COMBS IN THE FREQUENCY DOMAIN

4.1 Introduction [1]

Imagine a ball impinging on a network of nodes with a certain depth. At each node, the particle is scattered either to the left or to the right. Repeating the experiments many times results in a binomial distribution. This is the simplest form of well-know random walks and is often demonstrated using the Galton board[2]. These random walks provide basic building blocks of algorithms applied in economics and genetic evolution analysis. If the ball is a quantum particle, the distribution is markedly different. Now, the particle is in a superposition of all modes and the probability of the wave-function collapsing to a single-mode depends on the interference between the probability amplitudes. Another unique feature is that the initial superposition state of the particle affects the behavior and output of the quantum walk. Note that the walk can evolve either continuously by tunneling to neighboring modes or in discrete "coin-flip" steps. Following Feynman's insights, such well-controlled quantum systems can be used to simulate complex quantum many-body physical systems. Additionally, analogous to its classical counterparts, quantum walks inspired quantum algorithms with exponential speed-up in certain computations [108] and quadratic speed-up in database search [109] as well as tests of graph isomorphism [110].

Quantum walks have been demonstrated in matter-based platforms [111] as well as optical photons. In photons, a particle can "walk" in its spatial [112–117], temporal [118, 119], orbital angular momentum [120] and spectral degree of freedom [121–123]. In these previous demonstrations, tuning the depth of the walk required physical

[1] The results in this chapter are adapted in whole or part from the publication [107]

[2] Sometimes referred to as the "Bean machine."

modification to the physical layout of the circuit. Here, we demonstrate a tunable quantum walk of two entangled photons walking in the frequency domain. Walks of entangled particles lead to an exotic behavior that depends on the initial state of high dimensionally entangled biphoton frequency comb (BFC) [Fig. 4.1B]. By manipulating the input state's spectral phase, we observed enhanced ballistic transport and bound energy states. We provide a time-domain description that hints at the possibility of using such walks to probe and verify the degree of high-dimensional entanglement.

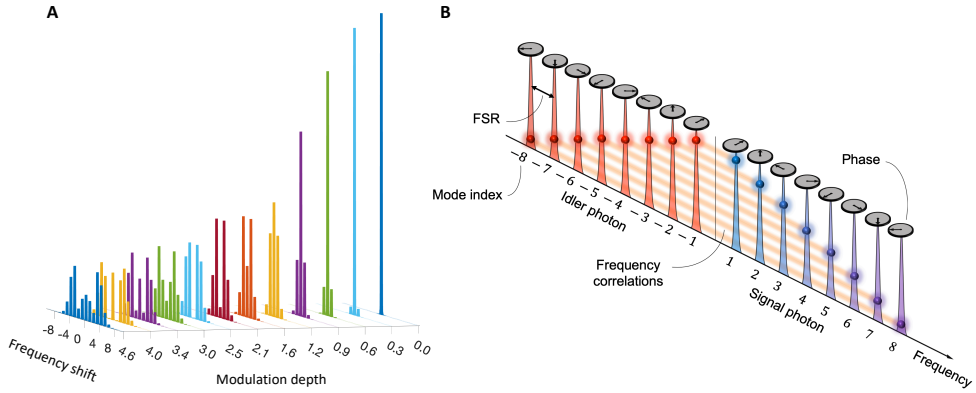

Fig. 4.1. Frequency domain mode splitting and biphoton frequency comb. (A) Experimental data showing the effect of phase modulation on a single frequency mode for various modulation depths. These spectra were acquired with classical light but also serve as an illustration of how every single mode, even in the quantum regime, is scattered by a phase modulator. The modulation speed was chosen to match the mode separation in our quantum source, and therefore, frequency shifts are presented in terms of the BFC mode index. (B) Illustration of a BFC in frequency space. Each photon of the entangled pair is in a superposition of eight distinct frequency modes with pairwise correlations about the center of the biphoton spectrum. This two-photon state has the form $|\psi\rangle = \frac{1}{\sqrt{8}} \sum_{m=1}^{8} |m, -m\rangle_{SI}$, and orange lines in the figure highlight correlations between each frequency pair. A pulse shaper is used to manipulate the phase on each frequency mode before the quantum walk.

4.2 Concept and Experimental Setup

In the case of a quantum walk in the frequency domain, the coupling is mediated by a periodic (temporal) modulation of the waveguide refractive index. Such coupling, or mode-splitting, can be realized in electro-optic phase modulators driven with a single sinusoidal radio-frequency (RF) tone. The effect of this perturbation is that the wavefunction of a photon traversing the waveguide picks up a factor of $e^{i\delta \cos \omega_m t}$. Here, δ corresponds to the strength of the modulating RF field, and ω_m denotes the frequency of this RF modulation. Viewed from the perspective of the frequency domain, phase modulation scatters a single frequency into a comb-like spectrum with adjacent frequency modes separated by ω_m in frequency (Fig. 4.1A). The amplitude of a comb line a distance $n\omega_m$ away from the original frequency is given by nth-order Bessel function $J_n(\delta)$. In analogy to quantum walks based on path encoding, the depth of such a frequency domain quantum walk can be incremented simply by cascading one modulator after another. However, a particular strength of the frequency domain approach is that a cascade of n identical phase modulators is equivalent to increasing the strength of the modulating RF field in a single modulator by this factor of n. In other words, the depth of the walk can be tuned over a continuous range by simply modifying the strength of the modulating RF field. This is in contrast to quantum walks in the spatial domain where the evolution of the state is determined by propagation length [112, 113].

Figure 4.1A shows results from quantum walks of a single photon that starts out in a single-frequency mode. As the strength of the modulating RF field (δ) increases, the extent to which the input mode scatters to outer frequency modes also increases. In Fig. 4.1A, the output photon distribution is plotted as a function of modulation strength δ, which, in our platform, is equivalent to the effective walk duration. The "rabbit ears" observed in this distribution signify the presence of ballistic energy transport–a signature of random walks with quantum systems. In particular, the

standard deviation (SD) of the output photon distribution grows linearly with δ [124], while for a classical random walk, the transport grows only as $\sqrt{\delta}$ [124].

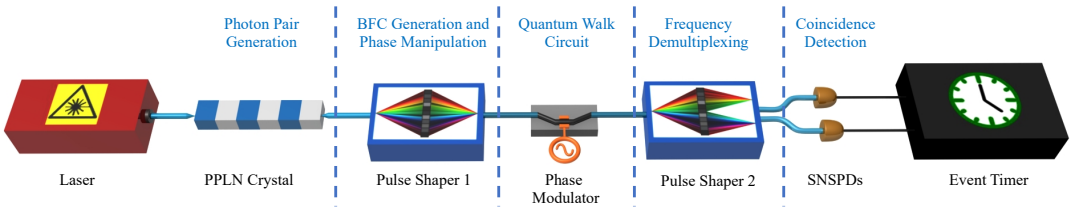

Fig. 4.2. The experimental setup of the frequency-domain quantum walk.

The experimental setup is depicted in Fig. 4.2. A continuous-wave 775-nm laser with about 1-mW power shining on a PPLN crystal generates broadband time-frequency entangled photons with about 40-nm (5-THz) bandwidth, with a power of about 5 nW. A pulse shaper is then used to carve this spectrum to make a BFC with 25-GHz frequency spacing between the bins and about 9-GHz linewidth. The pulse shaper is used to manipulate the amplitude of the biphoton spectrum and its phase prior to any quantum walk. Once the desired state has been prepared, it is sent to an electro-optic phase modulator that implements the mode-mixing operations which give rise to a quantum walk. Our modulator is driven with a 25 GHz sinusoidal RF waveform, identical to the free spectral range (FSR) of the BFC, with the RF power tunable over a continuous range. For the equipment used in our experiments, this index was $\sim$5. With small upgrades to our equipment (cabling and amplifiers rated to 25 GHz) or by cascading more phase modulators in series, higher modulation depths can be readily achieved. Downstream of the modulator is a second pulse shaper, which selects a pair of output frequencies and routes each one to a superconducting nanowire single-photon detector (SNSPD) (Quantum Opus). The relative arrival time of photons on the SNSPD pair is then monitored using an event timer (PicoQuant HydraHarp 400). Two-photon events between different frequency modes are identified by correlations in their arrival time and this data is used to construct a measurement of the joint spectral intensity (JSI) of the BFC – a two-photon

correlation map that illustrates the effects of a quantum walk in energy (frequency) space.

4.3 Results

4.3.1 Enhanced ballistic energy transport and energy bound states

One hallmark of a quantum walk is the observation of ballistic energy transport of the quantum state across modes of the system. We demonstrate even stronger transport for the case of a BFC entangled across eight dimensions and having the form $|\psi\rangle = \frac{1}{\sqrt{8}} \sum_{m=1}^{8} |m, -m\rangle_{SI}$, where S and I denote the signal (high-frequency) and idler (low-frequency) photons, respectively. The JSI of this state, i.e., in the absence of any RF modulation, is completely anticorrelated in frequency(Fig. 4.3A). Each pixel on the antidiagonal corresponds to the same two-photon energy, i.e., the sum of mode indices of any pixel on this line is zero. Note that the sum of the mode indices on any line parallel to the antidiagonal is a constant and corresponds to a different value for the total energy of the two-photon state. The diagonal terms $|i, i\rangle_{AB}$ were measured by splitting frequency mode i between detector channels A and B and are measured after all the off-diagonal elements. The acquisition time for diagonal elements was twice as long since there is a 50% probability that both photons end up at the same detector and, consequently, fail to register coincidences.

In Fig. 4.3B we show the JSI of this state after a quantum walk when the modulator is driven to a depth $\delta = 4.6$. Experimental data clearly show diffusion, or transport, of two-photon correlations away from the original JSI, which matches results expected from theory. Transport perpendicular to the sum-frequency axis (antidiagonal) and toward the top right corner of the JSI corresponds to events where the overall energy of the biphoton increases, i.e., the modulator transfers energy to the two-photon state. The converse, when the biphoton transfers energy to the modulator, manifests as transport toward the lower-left corner of the JSI. In other words, what we observe is two photons experiencing the same frequency shift, which resembles,

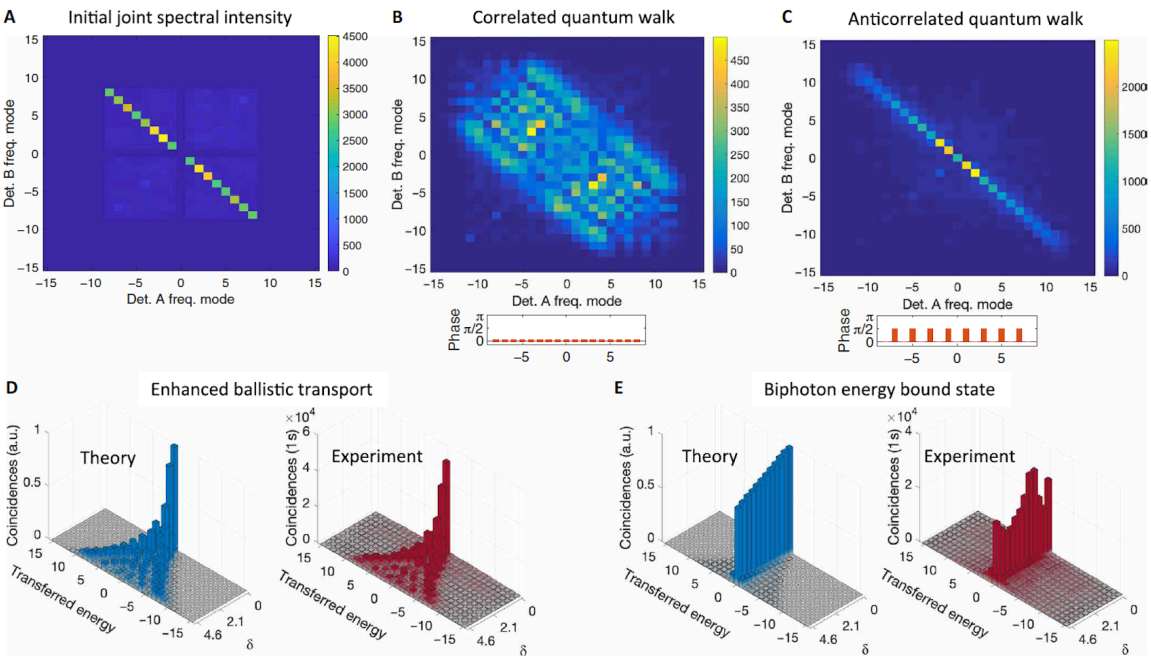

Fig. 4.3. (A) The anticorrelated JSI for an eight-dimensional BFC before the quantum walk. (B) JSI for a BFC after a quantum walk for the case when no additional phase is applied before the walk. This results in two-photon events where mode indices move in the same direction, i.e., we have bunching of photons in energy space. (C) Antibunching (mode indices of two-photon events move in opposite directions) is observed when adjacent modes start out with a π phase difference relative to one another. (D and E) Energy transferred from the phase modulator to the total biphoton state. The correlated quantum walk exhibits enhanced ballistic energy transport, and we see strong energy confinement for the anticorrelated walk. Energy transfer in these plots is presented in units of $h\nu$, where $\nu = 25\ GHz (h\nu = 1.656 \times 10^{23} J)$. All the JSI elements are coincidences measured in 1 s. a.u., arbitrary units.

but is qualitatively different from, bosonic bunching (Hong-Ou-Mandel interference) in the frequency domain [125].

To quantify this energy transfer, we tabulate the total number of events along the antidiagonal and along each line parallel to the antidiagonal, to determine the probability of a biphoton exiting the system with a particular total energy. Energy

transfer between the quantum circuit and the two-photon state, expressed in terms of the sum of photon mode indices, is plotted in Fig. 4.3D as a function of modulation depth. A similar walk for a fixed circuit depth was previously demonstrated with high-dimensional, path-entangled photon pairs [114].

By modifying the spectral phase of the BFC to create a state of the form $|\psi\rangle = \frac{1}{\sqrt{8}} \sum_{m=1}^{8} e^{im\pi} |m, -m\rangle_{SI}$, i.e., a state in which adjacent modes have a π phase with respect to one another, we demonstrate strong confinement of the biphoton energy. This operation can be viewed as a linear spectral phase ramp, which is equivalent to delaying one photon with respect to its entangled counterpart by half the modulation period. As a result of this delay, photons in an entangled pair acquire equal but opposite frequency shifts. This is clearly illustrated in the JSI measurement after a quantum walk (Fig. 4.3C), which shows that frequency correlations remain largely confined to the antidiagonal of the JSI measurement. In other words, the energy of the two-photon state is mostly unchanged. As the duration of the walk (modulation depth) increases, frequency correlations merely propagate outward along the antidiagonal to include new combinations of high- and low-photon energies. However, this energy gain or loss is correlated within a photon pair. If the idler gains some energy, then the signal loses that same amount of energy with the result that the total energy of the state is preserved. The variation in the coincidence rates shown in Fig. 4.3E is due to fluctuations of the photon flux in our entangled pair source.

4.3.2 Time domain perspective

The evolution of the biphoton, as depicted by two-photon correlation maps (Fig. 4.3, B and C), can also be understood from a time-domain illustration of the quantum walk that considers the effect of electro-optic phase modulation on the time correlation function of entangled photons. In Fig. 4.4, the strength of the modulating RF waveform is shown in black as a function of time. A signal photon (blue arrow) arrives at the modulator at random times owing to the nature of the photon pair generation

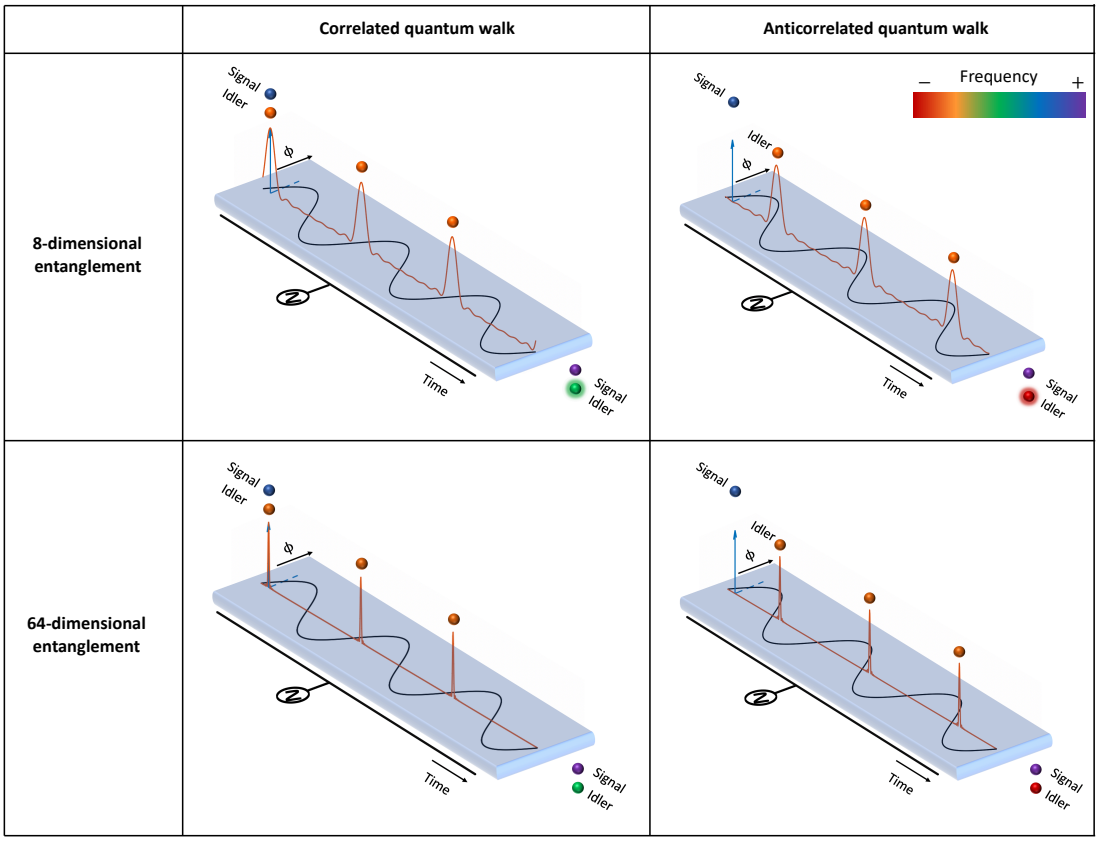

Fig. 4.4. Time-domain picture. Time-domain illustration of phase modulation for four different conditions (correlated or anticorrelated quantum walk, 8- or 64-dimensional entanglement). The strength of the modulating RF waveform is shown with the black sinusoid. The change in the color of output photons reflects their frequency shifts. The cloud around the idler photon in the eight-dimensional entangled case illustrates the wider range of possible frequency shifts due to wider time-correlation function pulse features.

process. Here, for example, the signal reaches the modulator when the phase of the modulating RF waveform is $\pi/6$. While the idler photon also reaches the modulator at a random time, its arrival is highly correlated with that of the signal photon. This correlation is characterized by a distribution of possible values for the delay between signal and idler. The distribution, in delay space, is given by the Fourier transform of the complex biphoton spectrum [126]. Consequently, for a narrowband biphoton spectrum with entanglement across a limited number of dimensions ("8-dimensional

entanglement" in Fig. 4.4), there is a wide range of possible values for the relative delay between signal and idler. As the entanglement dimensionality of the state increases, i.e., as the biphoton spectrum gets broader, the distribution of possible delays gets narrower ("64-dimensional entanglement" in Fig. 4.4). The discretization of the biphoton spectrum in frequency space, owing to its comb-like structure, results in a distribution of relative arrival times that repeats at integer multiples of the inverse comb FSR. Since the spacing between comb lines matches the frequency of the RF waveform, this repetition of the distribution in arrival times occurs at integer multiples of the modulation period. The net effect is that both photons experience nearly the same phase modulation slope ($d\phi/dt$), which means they experience correlated instantaneous frequency shifts ("correlated quantum walk" in Fig. 4.4).

For the energy bound state, the situation is slightly different. Here, there is a π phase difference between adjacent comb lines, which corresponds to a linear spectral phase ramp or simply a time delay. This time delay corresponds to exactly half the RF modulation period. In other words, the distribution in the relative arrival of signal and idler is now spaced at half-integer multiples of the modulation period. Here, unlike in the case of enhanced ballistic transport described earlier, photons in an entangled pair experience anticorrelated instantaneous frequency shifts ("anticorrelated quantum walk" in Fig. 4.4), which manifests through confinement of two-photon correlations to the antidiagonal (sum-frequency axis) of a JSI measurement.

4.3.3 Effects of high-dimensional entanglement

The critical role played by spectral phase hints at strong differences between quantum walks featuring coherent superpositions of multiple frequency pairs $|m, -m\rangle_{SI}$, as compared to mixtures of those same frequency pairs. While both states possess identical frequency correlations, in the latter, the relative phase between any two basis states ($|m, -m\rangle_{SI}$ and $|m\prime, -m\prime\rangle_{SI}$, for $m \neq m\prime$) is completely random. To simulate the effect of this random phase, we construct a JSI measurement of the mixed

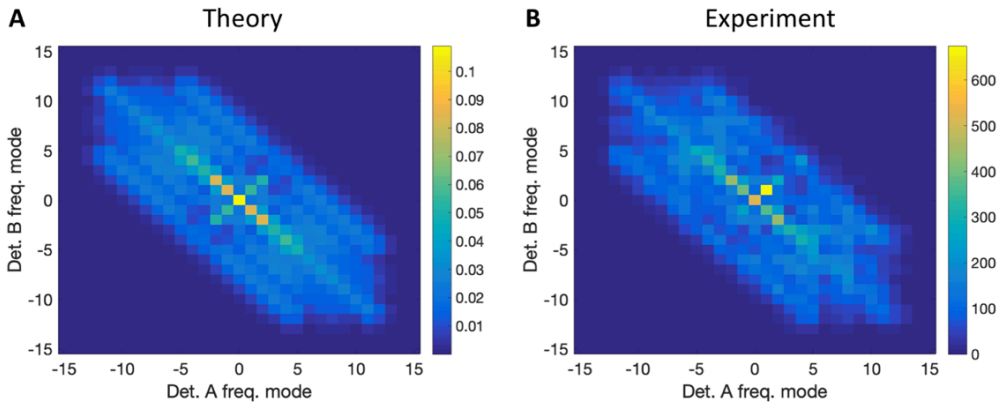

Fig. 4.5. Adding the JSI's of states $|m, -m\rangle$ for $m = 1, \ldots, 8$. The experimental results (b), match with theoretical simulations (a).

state by adding together JSI measurements resulting from quantum walks of individual frequency pairs $|m, -m\rangle_{SI}$, for $m = 1, , 8$. A clear effect of incoherence is that two-photon correlations are smeared out without any sharp or well-defined features (Fig. 4.5).

These results, together with walks presented earlier, suggest that the total energy of the two-photon state after a quantum walk can serve as an indicium of the coherence between frequency mode pairs. One metric to quantify this is the SD of biphoton energy measured at the output. This is presented in terms of the mode index (single-photon case) and the sum of mode indices (two-photon case), as a function of walk duration, in Fig. 4.6. We see a clear indication of enhanced energy transfer for the two-photon state. In the limit of infinite multilevel entanglement, energy transfer increases at twice the rate for two-photon correlations compared to the single-photon quantum walk since both photons experience exactly the same frequency shift. To elucidate the effect of the entanglement dimensionality, we present data for biphoton energy transfer in the cases of enhanced ballistic scattering (Fig. 4.6C) and strong energy confinement (Fig. 4.6D). Figure 4.6B shows how the SD of the output biphoton energy changes as the degree of multilevel entanglement increases for a fixed walk depth ($\delta = 6.1$). The clear change in the distribution of biphoton energies as a

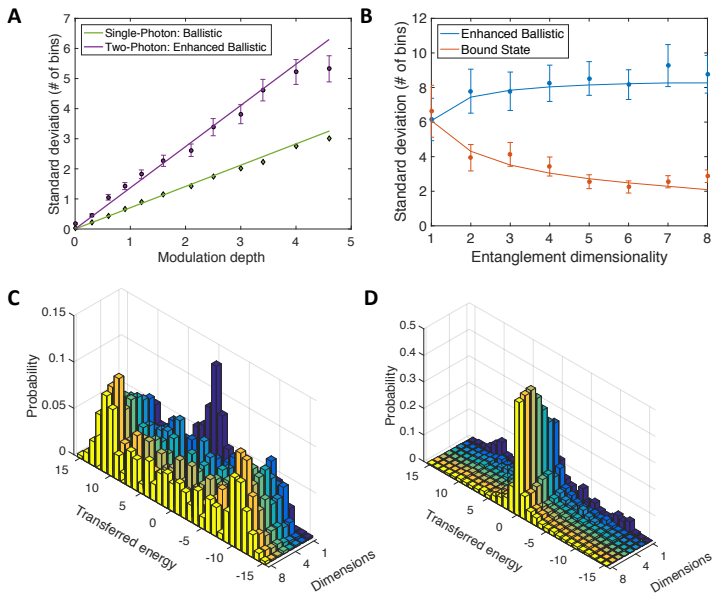

Fig. 4.6. Effects of entanglement dimensionality on quantum walks. (A) SD of single- and two-photon energy transport. In particular, the two-photon case considers an eight-dimensional, maximally entangled photon pair. Experimental data (purple and green markers) are plotted alongside results expected from theory (solid lines). Plot points are extracted from results in Figs. 4.1A and 4.3D. The SD grows linearly with the modulation index in both cases. However, the slope is roughly twice as steep for the two-photon case. (B) SD of the energy transfer (output mode) distribution as a function of entanglement dimensionality for the case of enhanced ballistic transport and energy confinement when $\delta = 6.1$. Theoretical predictions are represented by solid lines, and the markers correspond to experimental data extracted from (C) and (D). In (A) and (B), the SD is computed after background subtraction (coincidence-to-accidental ratio, ~ 50) and the error bars are calculated assuming Poissonian statistics. The error bars for single-photon energy transport in (A) are not shown since the experiment was carried out using classical light. (C and D) Energy transferred to the biphoton as a function of entanglement dimensionality for enhanced ballistic transport and the bound state, respectively. In (C), the "rabbit ears" grow as the entanglement dimensionality increases, resulting in a slight increase in SD, as shown in (B). In (D), increasing entanglement dimensionality reduces the occurrence of any net energy transport between the modulator and the BFC. Consequently, frequency correlations remain confined to the constant energy axis, i.e., the antidiagonal of the JSI shown in Fig. 2C, for example.

function of entanglement dimensionality, especially in the case of the energy bound state, points to how these results can potentially be used to certify, or even quantify, high-dimensional frequency-bin entanglement [33, 82].

4.4 Conclusion

In this chapter, we have used an electro-optic modulator as a tunable quantum walk circuit that couples and scatters frequency modes of a high-dimensionally frequency-bin entangled photon pair. By manipulating the superposition state of the input wavefunction, we demonstrate enhanced ballistic energy transport and energy bound states. The distinction between the quantum walk distribution of the correlated, anticorrelated, and the incoherent case becomes more evident when looking at the JSI (Fig. 4.7) in the limit of high modulation depth ($\delta = 200$). The correlated walk spreads diagonally while the anticorrelated walk spreads antidiagonally, resembling quasi-bosonic bunching and quasi-fermionic antibunching behavior, respectively. Furthermore, by setting the linear spectral phase of the input biphoton state to a slope of $\pi/2$, we observe quasi-anyonic behavior (Fig. 4.7c). Even though the wavefunction is anti-symmetric in the anticorrelated case, the electro-optic modulator operating on the state disturbs the anti-symmetry, resulting in deviations from true fermionic behavior. To simulate true fermionic behavior, a secondary degree of freedom can be used to prepare an anti-symmetric wavefunction and preserve it after the frequency domain walk [127, 128]. This can be done using a polarization-entangled source and a polarization diversity phase modulator, or with time-bins and interferometers.

In addition to the behaviour observed, other phenomena such as Bloch oscillation [111, 129], and Anderson localization [130] may be observed by controlling the RF field experienced by each lattice point (frequency-bin), i.e. adding an inhomogeneity to the circuit. Such effects can be induced, for example, by using more complex setups such as resonant electro-optic modulator [122], or a modulator in a loop using low-loss fast-switching integrated photonics. Even more interesting is to observe the

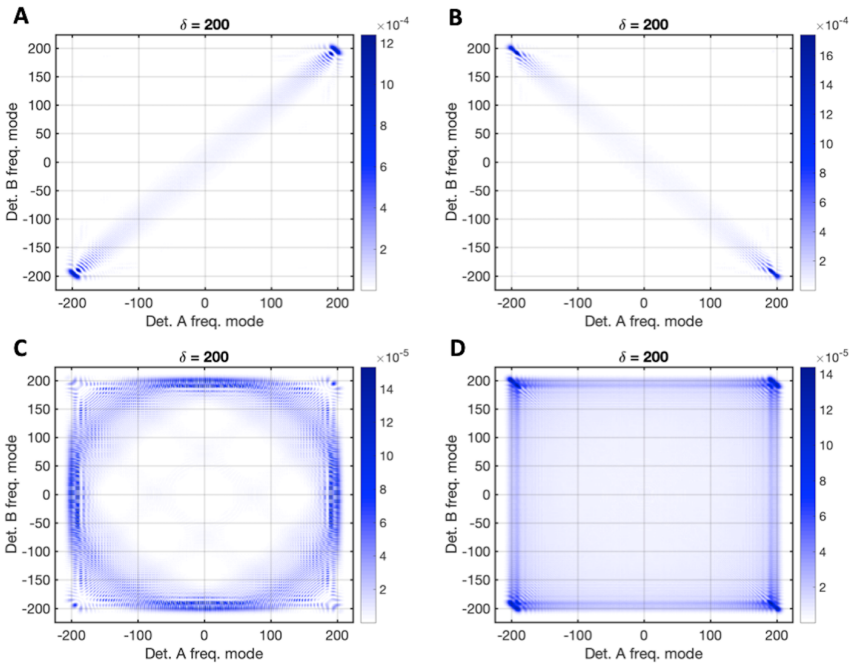

Fig. 4.7. Output JSI in the limit of high modulation depth ($\delta = 200$). a, correlated, b, anticorrelated, c, uncorrelated energy transfer and d, incoherent case, all simulated. a, and b, in the limit of high modulation clearly show bunching and antibunching effects, respectively, whereas in c, the biphotons relative delay is quarter-integer multiple of the modulation period resulting in a quasi-circular pattern. In d, the photons are less correlated with each other.

effects of multipartite high-dimensional states and identify any quantum behaviour unique to such states [131], as well as testing the resilience of various superpositions of two-photon states to disorder in the system [132].

Finally, the dependence of energy transport, especially in the bound energy state, signals the possibility of using such walks to verify the multi-level entanglement of the input BFC state. In principle, the degree of entanglement, assuming a symmetric noise model, can be certified by direct measurement of the time correlation function, however, the typical jitter of SNSPDs ($\sim 60 - 80$ ps) prevents such measurement. An alternative approach is frequency projection methods [133] such as those adopted in chapter. 2, nevertheless, such projections become laborious with increasing dimen-

sions. Certainly, a more rigorous proof [134] is needed to set tight bounds on the SD of energy transport.

5. RAPID RF SUB-SAMPLING AND DISAMBIGUATION USING DUAL COMBS

5.1 Introduction[1]

Radio frequency communications has profoundly transformed the way societies communicate and its impact is evident in our daily lives. Spectral sharing to satisfy a large number of applications and users, in addition to growing systems' complexity, has exacerbated the demand for wideband frequency sensing across tens to hundreds of gigahertz. Analog to digital converters (ADC), however, have not been keeping pace with this growing spectral demand due to limitations in sampling rate and analog bandwidth. Furthermore, in some radar and telecommunication applications, the signal is transmitted over a wide bandwidth but has sparse content. Direct digitization of such signals, if possible, is often inefficient and generates high streams of data, complicating the processing and storage of information. Compressive sensing and Nyquist folding receivers have emerged as an alternative solution in which wideband RF signals are folded to a smaller band [136]. Photonic based downconverters are immune to electromagnetic interference and are better suited for wideband operation. These downconverters can be classified into two general methods. The first is based on translating the signal from the original carrier frequency to an IF band accessible to ADCs [137, 138]. The tunability of such systems is often limited by the speed of thermally tuned fiber Bragg grating filters. The second method uses spectral folding thru sub-sampling with intentionally induced jitter to disambiguate over a multitude of multi-octave aliasing bands [139–141].

Using dual electro-optic combs, we demonstrate rapid disambiguation over 10 Nyquist bands (10 GHz Bandwidth). This technique can be directly extended to cover

[1]The results in this chapter are partially adapted from the publication [135]

K to W bands. This scheme has similarities to sub-sampled links with perturbed sampling rates [140]. Compared to previously demonstrated Vernier comb based disambiguation [141], the implementation demonstrated here is more focused toward on-chip integration. The setup does not require any frequency shifting stages or optical filtering. Furthermore, no pulse compression stage is required. The setup can be readily integrated using existing technology thereby offering important advantages in size, weight, and power.

5.2 Concept and Experimental Setup

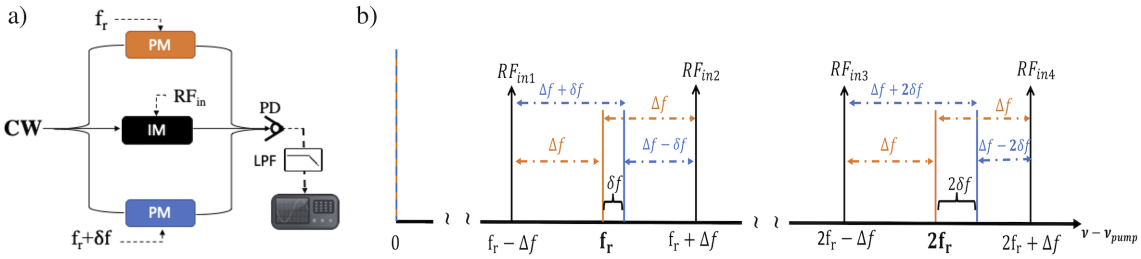

Fig. 5.1. (a) The experimental setup; continuous-wave (CW), phase modulator (PM), intensity modulator (IM), photodetector (PD), low pass filter (LPF). (b) Illustration of the scheme, the orange lines are the comb lines of the 'f_r' phase modulator and the blue lines are the comb lines of the '$f_r + \delta f$' phase modulator. The black lines represent the input RF signal for different cases.

The experimental setup is shown in Fig. 5.1. A continuous-wave laser (CW) laser is split to feed three arms. Two arms have phase modulators driven by locked RF sinusoids: f_r for one arm and $f_r + \delta f$ for the other, where δf is a small offset frequency. A third arm contains a quadrature biased intensity or Mach-Zehnder modulator (MZM) driven by the RF signal of interest. The branches are combined and detected by an amplified 1.5 GHz InGaAs photodetector followed by a low pass filter and an oscilloscope with 2 GHz bandwidth. The signal is digitally filtered to

pass only a bandwidth of 1 GHz (f_r). The operating principle is depicted in Fig.1b. An RF input signal at either $f_r + \Delta f$ or $f_r - \Delta f$ beat with the comb modulated at f_r resulting in a beat-note at Δf. More generally, this is also the case for all input RF signals $m \cdot f_r \pm \Delta f$ where m is the aliasing band. With only one comb, the aliasing band is ambiguous. However, the addition of a second comb with $f_r + \delta f$ repetition rate results in a second beat spaced $\pm m \cdot \delta f$ away from the first beat, thereby disambiguating the signal's aliasing band. The sign of the second beat spacing ($\pm m \cdot \delta f$) resolves the ambiguity of the signal's position relative to the nearest 'f_r' comb line. If the sign is positive, the signal is on the low side and vice versa, on the high side for a negative spacing. The previous discussion assumes that we know which comb produced which beat note. In practice; however, this is not the case. An input signal at $m \cdot (f_r + \delta f) \pm \Delta f$ also produces a beat-note at Δf and a second beat spaced $\pm m \cdot \delta f$ away from the first beat. To resolve this ambiguity, we can vary the amplitude of one comb or use different powers for each EO comb. Alternatively, if we extend the electrical detection window up to f_r, we obtain a second set of beat-notes in the region $[f_r/2, f_r]$, where the two beat-notes for each input RF signal do not overlap, and the ambiguity can be resolved solely based on the frequency of the beat-notes (see Fig. 2c).

Experimental results are shown in Fig. 5.1 The 'f_r' phase modulator is driven with a 1 GHz sinusoid and the 'offset modulator' is driven at 1.002 GHz (δf = 2 MHz). A 20 μs trace (40 interferograms) is shown in Fig. 5.2a. For an input RF signal at 6.7 GHz, the power spectral density of the trace is shown in Fig. 5.2b. Two beats are seen, one centered at 300 MHz and the second is 14 MHz ($7 \cdot \delta f$) higher. Therefore, the original signal is deduced to be at $7f_r - \Delta f$, which is 6.7 GHz as expected. Fig. 5.2d overlays all input RF signals at $m \cdot f_r \pm 300$ MHz for 10 aliasing bands (20 different input signals, one at a time, representing all 20 Nyquist zones). Each signal produces a beat at 300 MHz, and a secondary beat which disambiguates the Nyquist zone, potentially allowing simultaneous detection. The amplitude disparity between different Nyquist zones depends on the spectral envelope of the simple EO

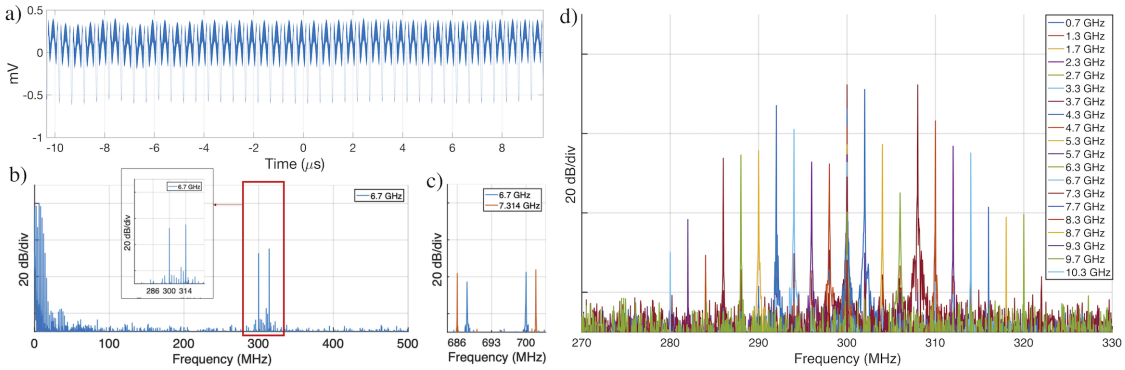

Fig. 5.2. (a) 20 μs temporal trace (40 interferograms) with a 6.7 GHz input signal. (b) Power spectral density of the 20 μs trace. (c) beat-notes for 6.7 GHz and 7.314 GHz input signals in the region $[f_r/2, f_r]$. (d) Overlaid zoomed view of beat-notes for multiple input signals at (m $\cdot$ 1 GHz $\pm$ 300 MHz) independently measured, where m is swept from 1 to 10. Note that all of these input generate a beat-note at 300 MHz and another at a separate frequency.

combs that showed a Bessel function spectral profile. Flat EO combs are expected to yield a flatter sensing bandwidth. As discussed previously, for the case of the 6.7 GHz signal, an input signal at 7.314 GHz also produces two beat-notes at 314 MHz and 300 MHz. This ambiguity can be resolved if the two comb lines have different powers, or by extending the detection window up to f_r, as shown in Fig. 5.2c. In addition to the large variation in conversion efficiency, a careful analysis of each signal reveals strong harmonic distortion. To address these concerns, we develop a theoretical model and provide analytical expressions for the harmonic distortion terms as well as the conversion efficiency. Our analysis, detailed in the next section, shows that it is possible to operate the link at a third-order limited operational point.

5.3 Theoretical model and RF link metrics

We start by writing the total electric field at the photodetector as

$$e_T(t) = \sqrt{2\ P_{in,o}} cos(\omega_o t) \left(\sqrt{\ell_{PM_1}} e^{i\delta cos(\omega_1 t)} + \sqrt{\ell_{PM_2}} e^{i\delta cos(\omega_2 t)} + \sqrt{\ell_{MZM}} MZM \right) \tag{5.1}$$

where $P_{in,o}, \omega_o, \omega_1, \omega_2, \delta$, are the input optical power, optical carrier radial frequency, the first and second PMs' driving frequency ($\omega_2 = \omega_1 + \Delta\omega$) and the PM's modulation depth, respectively. The first two exponentials inside the parenthesis represent the phase modulators. The factor ℓ represents the total loss, i.e. photon loss or splitting ratio, for each branch. Throughout this chapter, we'll assume that losses in the phase modulators' branch are equal, i.e. $\ell_{PM1} = \ell_{PM2} = \ell_{PM}$. The last term is the MZM's transfer function. The current at the photodetector $I_d = \mathcal{R}|e_T|^2$, can be expanded as

$$\begin{aligned} I_d = \mathcal{R} P_{in,o} \left(1 + cos(2\omega_o t)\right)\ \times \\ \Bigg(2\ell_{PM} + 2\ell_{PM}\ cos\Big(\delta\left[cos(\omega_1 t) - cos(\omega_2 t)\right]\Big) + \ell_{MZM}|MZM|^2 + \\ 2\ \Re\Big\{ \sqrt{\ell_{PM}\ell_{MZM}}\ MZM\left[e^{-i\delta cos(\omega_1 t)} + e^{-i\delta cos(\omega_2 t)}\right]\Big\} \Bigg) \end{aligned} \tag{5.2}$$

where $\mathcal{R}, H_{pd}$ is the photodetector's responsivity. The last term represents the mixing terms that convert the signal of interest to baseband and the symbol $\Re$ refers to the real part of the expression. Using a balanced dual branch push-pull MZM, we can write its transfer function as

$$MZM = \frac{1}{2}\left(e^{i\phi(t)/2} - e^{-i\phi(t)/2}\right) \tag{5.3}$$

where $\phi(t) = \phi_{dc} + \phi_{rf}\ cos(\omega_{rf} t)$ and $\phi_{rf} = \sqrt{2R_i P_{rf,in}}\frac{\pi}{V_\pi}$. Here, $\omega_{rf}, P_{rf,in}, R_i, V_\pi$ is the input RF signal, the input RF power, input resistance and the MZM's π voltage, respectively. Substituting the following identities in the MZM's expression

$$cos\left(\phi\ cos\Omega\right) = J_o(\phi) + 2\sum_{n=1}^{\infty}(-1)^n J_n(\phi)\ cos(2n\Omega) \tag{5.4}$$

$$sin\left(\phi\ cos\Omega\right) = -\,2\sum_{n=0}^{\infty}(-1)^n J_{2n+1}(\phi)\ cos\Big((2n+1)\Omega\Big) \tag{5.5}$$

and using the Jacobi-Anger expansion

$$e^{i\phi cos(\Omega)} = J_o(\phi) + 2\sum_{n=1}^{\infty} i^n J_n(\phi) cos(n\Omega) \tag{5.6}$$

where J_n is the nth order Bessel function of the first kind, we expand eq. 5.2 focusing on the mixing terms to obtain

$$I_d = \cdots + 8\sqrt{\ell_{PM}\ell_{MZM}} P_{in,o} \mathcal{R} \sum_{k=1}^{\infty} i^{2k} J_{2k-1}(-\delta) \left[cos\big((2k-1)\omega_1 t\big) + cos\big((2k-1)\omega_2 t\big)\right] \times \left[cos(\phi_{dc}/2) \sum_{n=0}^{\infty} (-1)^{n+1} J_{2n+1}(\phi_{rf}/2)\ cos\big((2n+1)\omega_{rf} t\big) + sin(\phi_{dc}/2) \sum_{n=1}^{\infty} (-1)^n J_{2n}(\phi_{rf}/2)\ cos(2n\omega_{rf} t)\right] \tag{5.7}$$

The first summation represents the comb lines of the two phase modulators. Notice that the summation now is with respect to '2k-1', i.e. only the odd phase modulators' comb sideband pairs contribute to the downconverted terms in the sub-sampling process. This arises mathematically from the real signal constraint in eq. 5.2, thereby necessitating the detection bandwidth to be equal to or greater than ω_1. The other summation terms arise from the MZM transfer function. Notice that the even-order harmonics can be suppressed at null-bias operation, this is in contrast to IMDD links which are third-order limited at quadrature bias.

The RF photocurrent corresponding to the input RF signal downconverted to baseband from beating with a single phase modulator can be obtained from

$$I_{d,\omega_{rf}-\tilde{k}\omega_1} = -8\sqrt{\ell_{PM}\ell_{MZM}}\ \mathcal{R} P_{in,o} \times i^{2k}\ J_{\tilde{k}}(-\delta)\ J_1(\phi_{rf}/2)\ cos(\phi_{dc}/2)\ cos\big(\omega_{rf} t\big)\ cos\big(\tilde{k}\omega_1 t\big) \tag{5.8}$$

where $\tilde{k}$ is an odd integer representing the comb's sideband number that downconverts the signal to baseband. Using the small-signal approximation for the Bessel function,

$J_n(\phi_{rf}) \approx \phi^n/2^n n!$, for $\phi_{rf} \ll 1$, we calculate the average RF output power per beat-note as

$$P_{\omega_{rf}-\tilde{k}\omega_1} = \left\langle I^2_{d,\omega_{rf}-\tilde{k}\omega_1} \right\rangle R_o |H_{pd}|^2$$
$$= \ell_{PM}\ell_{MZM}R_oR_iP_{in,rf} \left(\mathcal{R}P_{in,o}|H_{pd}|\ cos(\phi_{dc}/2)\ |J_{\tilde{k}}(-\delta)|\frac{\pi}{V_\pi}\right)^2 \quad (5.9)$$

where $< \cdot >$ denotes the time average, and H_{pd} is the photodetector's response function. Similarly, the average RF output power per beat-note for the higher-order

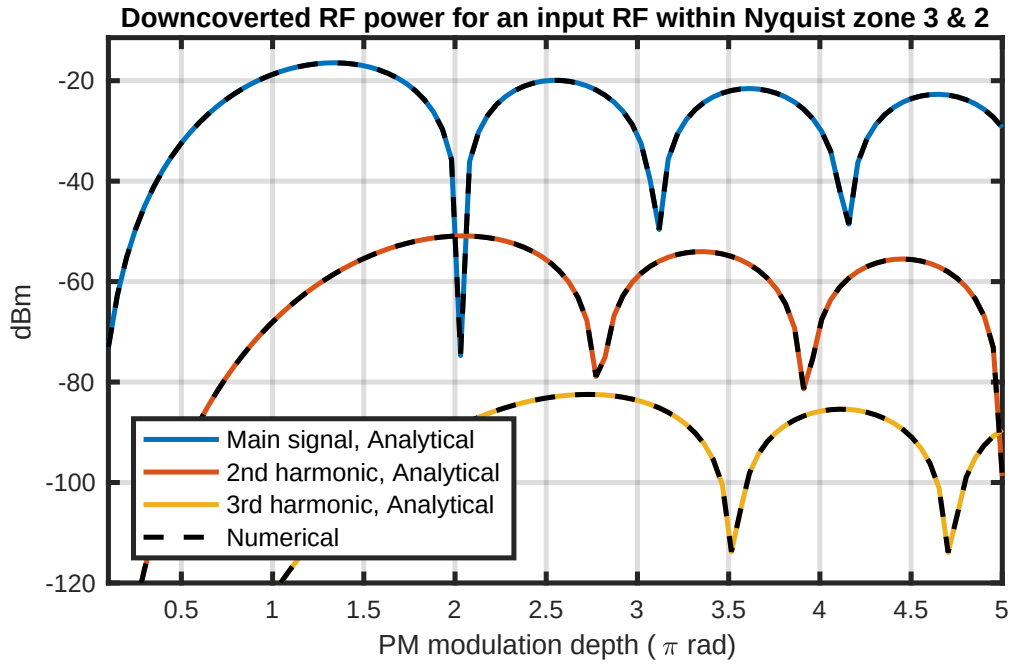

Fig. 5.3. RF power of the downconverted signal and its harmonics. The colored lines are obtained from the analytical expressions while the dashed lines are obtained from direct numerical computation of eq. 5.1.

harmonic distortions can be calculated using eq. 5.7 as

$$P_{2\omega_{rf}-\tilde{k}_2\omega_1} = \frac{\ell_{PM}\ell_{MZM}R_o}{2^5} \times$$
$$\left(\mathcal{R}P_{in,o}|H_{pd}|\ sin(\phi_{dc}/2)\ |J_{\tilde{k}_2}(-\delta)|\ R_iP_{in,rf}\right)^2 \left(\frac{\pi}{V_\pi}\right)^4 \quad (5.10)$$

$$P_{3\omega_{rf}-\tilde{k}_3\omega_1} = \frac{\ell_{PM}\ell_{MZM}R_o}{2304} \times \left(\mathcal{R}P_{in,o}|H_{pd}|\ cos(\phi_{dc}/2)\ |J_{\tilde{k}_3}(-\delta)|\frac{\pi}{V_\pi}\right)^2 (R_iP_{in,rf})^3 \quad (5.11)$$

where the subscript $\tilde{k}_2$ ($\tilde{k}_3$) is an odd integer representing the comb's sideband number that downconverts the second (third) harmonic to baseband. Fig. 5.3 compares the direct numerical computation of eq. 5.1 to the obtained analytical expressions showing excellent overlap. Having obtained the fundamental and harmonics power, the next step is to use these expressions to compute the link's analog metrics. Throughout this chapter, we'll assume that the input power is first split by half into two branches, one goes to the MZM while the other half is split again between the two phase modulators, so $\ell_{MZM} = 2\ell_{PM1} = 2\ell_{PM2} = 2\ell_{PM} = 1/2$. Unless otherwise specified, Table. 5.1 shows the values used in any forthcoming calculation.

5.3.1 Link Metrics

Gain and noise figure

The small signal RF gain (or conversion efficiency) per beat-note can be readily found using

$$\begin{aligned} G_{RF} &= \frac{P_{\omega_{rf}-\tilde{k}\omega_1}}{P_{in,rf}} \\ &= \ell_{PM}\ell_{MZM}R_oR_i\ \left(\mathcal{R}P_{in,o}|H_{pd}|\ cos(\phi_{dc}/2)\ |J_{\tilde{k}}(-\delta)|\frac{\pi}{V_\pi}\right)^2 \end{aligned} \quad (5.12)$$

The RF gain at null-bias (third-order limited sub-sampled link) is shown in Fig. 5.5. As in the typical intensity-modulated direct-detection (IMMD) link,the gain is proportional to the square of the $(P_{in,o}/V_\pi)$ ratio. Unlike typical sampled analog optical links where all of the sampling comb spectral lines have sidebands which add up coherently at the photodetector, here, the signal of interest is downconverted to baseband by beating with only a single sideband pair. Therefore, the gain drops as the PM's modulation depth is increased—a result of the aforementioned sideband pair

Table 5.1.
Sub-sampled link parameters.

	Symbol	value [unit]
PM_1 frequency	$\omega_1/2\pi$	1 GHz
PM_2 frequency	$\omega_1/2\pi$	1.002 GHz
Offset frequency	$\Delta\omega/2\pi$	2 MHz
Input optical power	$P_{in,o}$	50 mW
Combined loss/splitting ratio in the MZM branch	ℓ_{MZM}	1/2
Combined loss/splitting ratio in the PM_x branch	ℓ_{PM_x}	1/4
PM Modulation depth	δ	varied
MZM's π voltage	V_π	4 V
Input RF power	$P_{rf,in}$	0 dBm
Input Resistance	R_i	50 Ω
Output Resistance	R_o	50 Ω
Photodiode circuit filter function	H_{pd}	1/2
Photodiode responsivity	$\mathcal{R}$	1 A/W

sharing a smaller fraction of the comb's optical power as its bandwidth is increased. This ultimately constitutes a trade-off between gain and the detection bandwidth (i.e. number of Nyquist zones). The fades or nulls in the gain profile are a result of the PM's spectra following a Bessel distribution. Since the link will be operated at a fixed modulation depth, this doesn't constitute a serious problem. However, for each Nyquist zone, these nulls occur at different modulation depths as shown in Fig. 5.5. Therefore, the modulation depth must be chosen carefully. For example, using a modulation depth of 4.6π, 16 Nyquist zones can be detected with only $\sim 8\ dB$ of gain variation—see the right panel of Fig. 5.5.

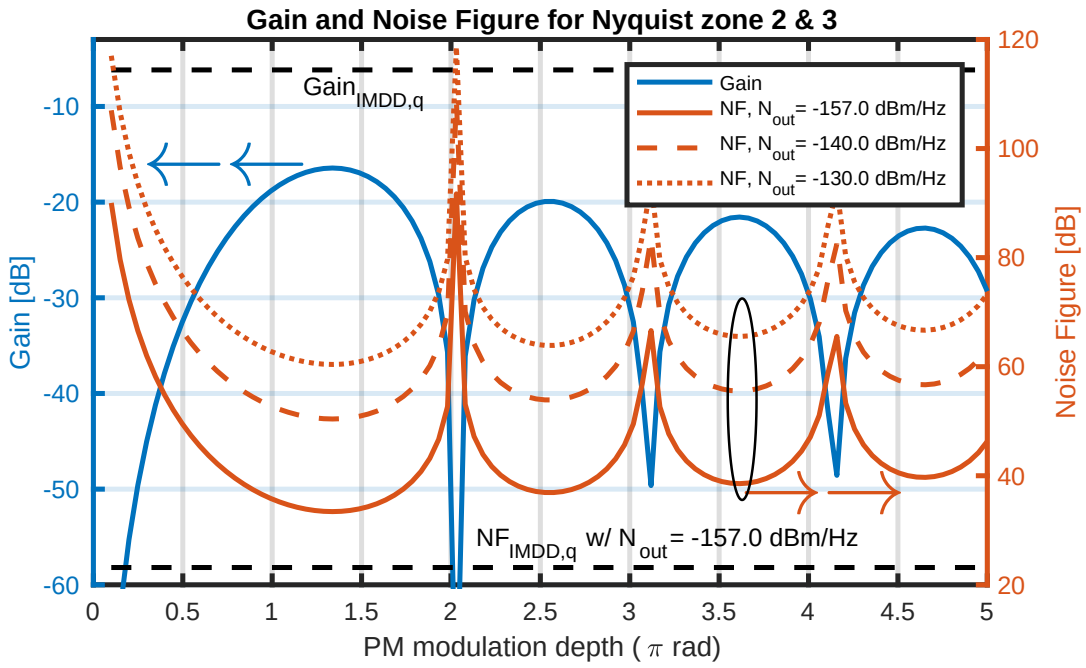

Fig. 5.4. The sub-sampled link RF gain and noise figure assuming three different noise levels for an input signal within Nyquist zone 2 or 3. The dashed lines show the gain assuming a quadrature-biased IMDD link.

Finally, we use the gain to compute the link's noise figure

$$NF = \frac{N_{out}}{G_{RF}\ k_B T} \tag{5.13}$$

where $k_B T$ represents the thermal noise contribution (k_B is Boltzmann's constant and $T = 290$ K), and N_{out} it the total electrical noise power spectral density at the link output. The results are plotted in Fig. 5.4 assuming three different levels of noise. Compared to a quadrature biased IMDD link with the same level of noise, the sub-sampled NF is 10-15 dB higher—a result of lower link gain. While the NF levels are high (≥ 33 dB) compared to their electronic counterparts, this is generally a challenge for all analog photonic processors. A radical improvement in NF requires a breakthrough in improving the V_π and high power handling photodetectors. For this link in particular, since the downconverted beat-note pairs arise independently of

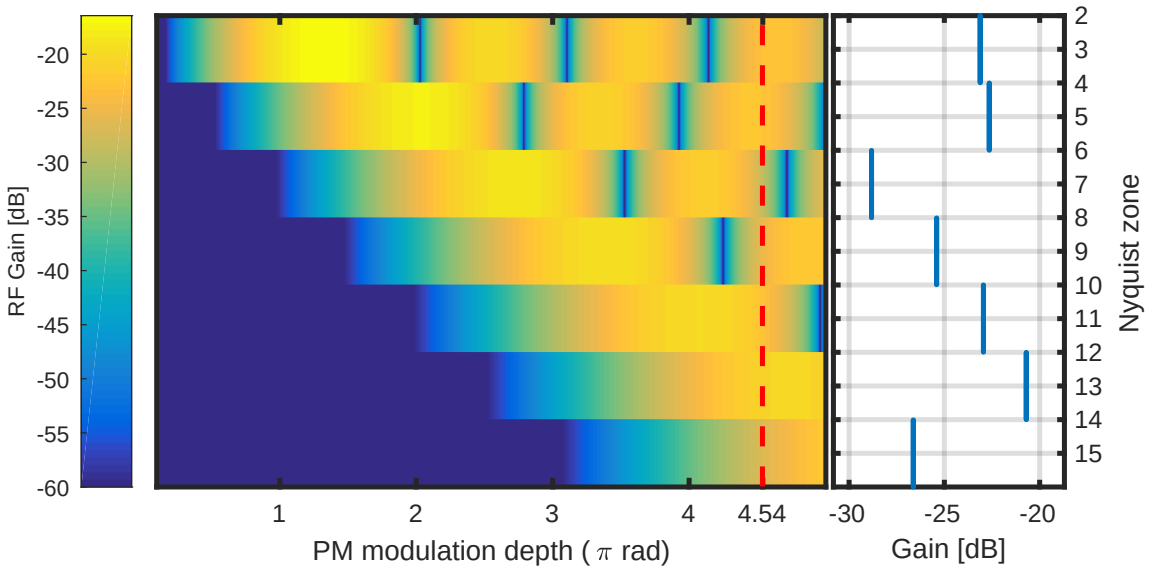

Fig. 5.5. RF Gain for different Nyquist zones. The dashed red line is expanded in the right panel.

each other, combining the outputs of the two PMs is not necessary. Instead, the MZM output can be split by half, each combined with a PM followed by a balanced photodetector. Such balanced detectors can cancel common noise, and increase the gain. Additionally, the reduced detection bandwidth offered by the sub-sampled link makes the design of efficient and high-current handling photodetectors less demanding.

Dynamic range and intercept points

By equating the RF output powers, eq. 5.9 with eq. 5.10 or eq. 5.11, we can find the 2^{nd} and 3^{rd} order input intercept point (IIP)

$$IIP_2 = \frac{2^5}{R_i}\left(\frac{cos(\phi_{dc}/2)\ |J_{\tilde{k}}(-\delta)|\ V_\pi}{sin(\phi_{dc}/2)\ |J_{\tilde{k}_2}(-\delta)|\ \pi}\right)^2 \tag{5.14}$$

$$IIP_3 = \frac{48\ |J_{\tilde{k}}(-\delta)|\ V_\pi^2}{R_i\ |J_{\tilde{k}_3}(-\delta)|\ \pi^2} \tag{5.15}$$

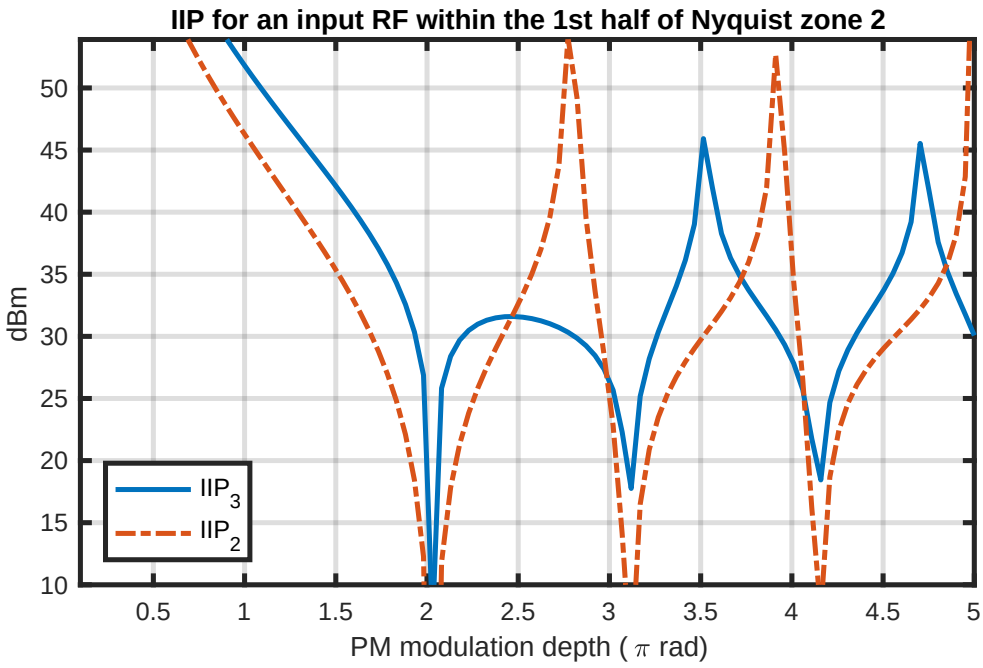

Fig. 5.6. Second order (at quadrature bias) and third-order (at null-bias) limited IIP for an input signal within the first half of Nyquist zone 2.

These equations are plotted in Fig. 5.6. As expected, the IIPs are a function of V_π^2 and are independent of the input optical power. Substituting these expression back in eq. 5.9, we get

$$OIP_2 = 2^5 \ell_{PM} \ell_{MZM} R_o \left(\mathcal{R} P_{in,o} |H_{pd}| \right)^2 \frac{cos(\phi_{dc}/2)^4 \ |J_{\tilde{k}}(-\delta)|^4}{sin(\phi_{dc}/2)^2 \ |J_{\tilde{k}_2}(-\delta)|^2} \tag{5.16}$$

$$OIP_3 = 48 \ell_{PM} \ell_{MZM} R_o \left(\mathcal{R} P_{in,o} |H_{pd}| cos(\phi_{dc}/2) \right)^2 \left[\frac{|J_{\tilde{k}}(-\delta)|^3}{|J_{\tilde{k}_3}(-\delta)|} \right]. \tag{5.17}$$

Notice that the output intercept points (OIP), on the other hand, are independent of the MZM's V_π and are proportional to $P_{in,o}^2$, as is the case for the IMMD link architecture. The Bessel factors result in the deep fades shown in Fig. 5.17. Such operational points must be avoided as discussed previously.

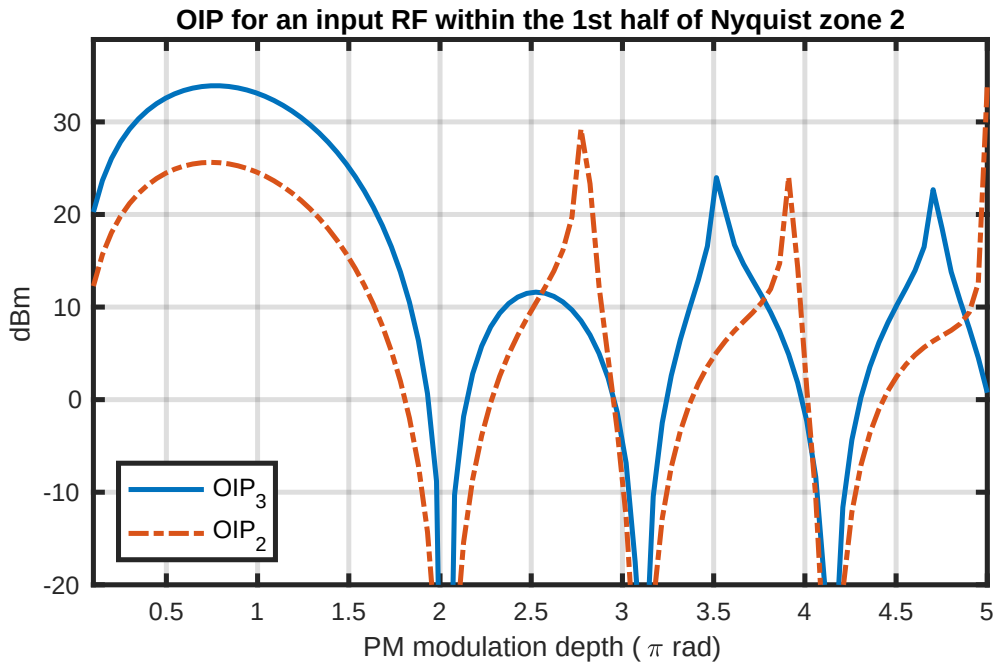

Fig. 5.7. Second order (at quadrature bias) and third-order (at null bias) OIP for an input signal within the first half of Nyquist zone 2.

Having calculated $OIP3_n$, the spurious-free dynamic range (SFDR) can be readily calculated using the following relationship

$$SFDR_n = \left(\frac{OIP_n}{N_{out}}\right)^{(n-1)/n} \tag{5.18}$$

The second-order, at quadrature bias, and third-order limited SFDR, at null bias, are plotted in Fig. 5.8 for an input signal within the first half of Nyquist zone 2. By setting the operational point to third-order limited regime, we can increase the SFDR by 30-35 dB—more than a 1000 fold improvement in dynamic range. Even with an output noise level as high as -130 dBm, SFDRs $\sim$ 100 dB can be achieved. Note that, typically, the SFDRs are calculated based on the two-tone test and the intermodulation distortion (IMD) points—as was done in the chapter 6. This is usually adopted since higher harmonics fall out of the detection window, and the system is limited by the IMD. However, in our case, the system - by design - detects

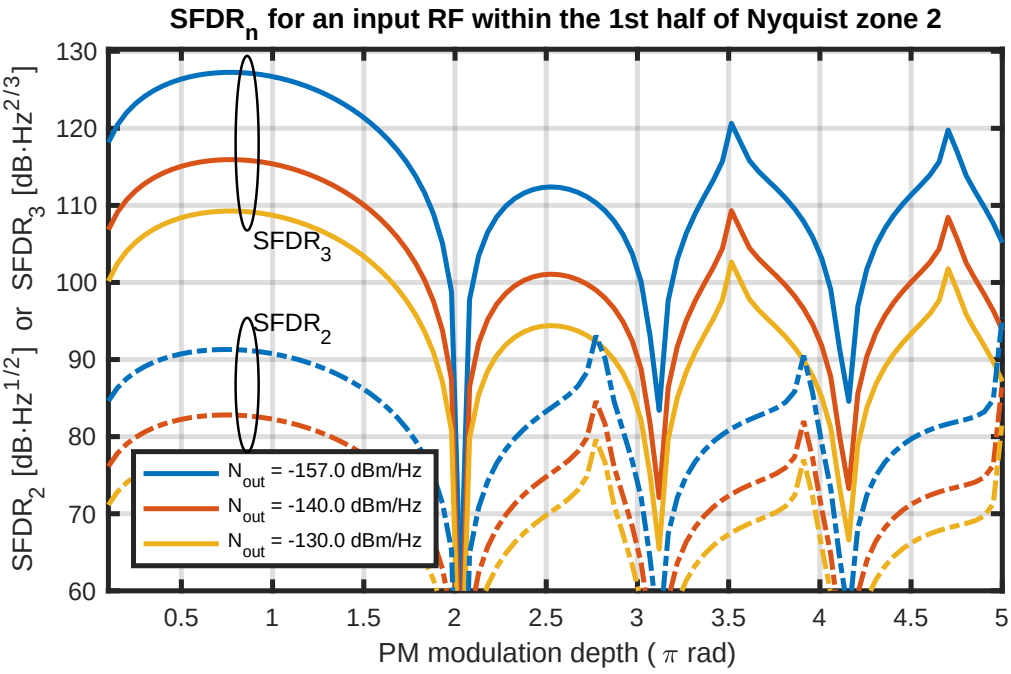

Fig. 5.8. The third-order limited SFDR at null biased and the second-order limited SFDR at quadrature bias (dashed lines) at three different output noise levels for an input signal within the first half of Nyquist zone 2.

several Nyquist zones, so the dynamic range for the lower Nyquist zones will be limited by the harmonic distortion. Thus, the SFDRs are calculated based on these harmonics. For higher Nyquist zones, the SFDR increases as the harmonics fall out of the detection window, and the IMD becomes the limiting distortion.

The Effect of the Modulator's Chirp

In the experimental results, we observe that the RF signal beats with both the even and order comb sidebands—see Fig. 5.2 b and c. However, the theoretical model shows that the RF signal of interest beats with only the odd comb sideband pairs. This apparent discrepancy between experiment and theory is a result of the MZM chirp. The MZM used in the experiment is a Z-cut (EOspace AZ-0k5-20-PFU-PFU-

UL) modulator with a vendor specified chirp factor of ~ 0.7 [142]. This leads to an asymmetric voltage drive between the two branches of the MZM, resulting in residual phase modulation. Using the expressions in [143], we can write the asymmetric drive as

$$MZM = \frac{1}{2}\left(e^{i(\phi_{dc}+\phi_{rf1}\ cos(\omega_{rf}t))/2} - e^{-i(\phi_{dc}+\phi_{rf2}\ cos(\omega_{rf}t))/2}\right) \tag{5.19}$$

where $\phi_{rf_1} = 0.18\ \phi_{rf_2}$. Fig 5.9 shows the simulation with the asymmetric drive taken into account and the MZM bias at quadrature; as was done experimentally. The results show that indeed two pairs of beat-notes (and others resulting from the harmonics) are obtained within the 1 GHz detection bandwidth, corresponding to the input RF signal beating with both the even and the odd sidebands of the phase modulator. Note that even at null bias, the second harmonic distortion is not suppressed in this case. Therefore, it is critical that future designs are based on a zero-chirp (e.g. X-Cut $LiNbO_3$) modulator in order to achieve a third-order limited operational regime.

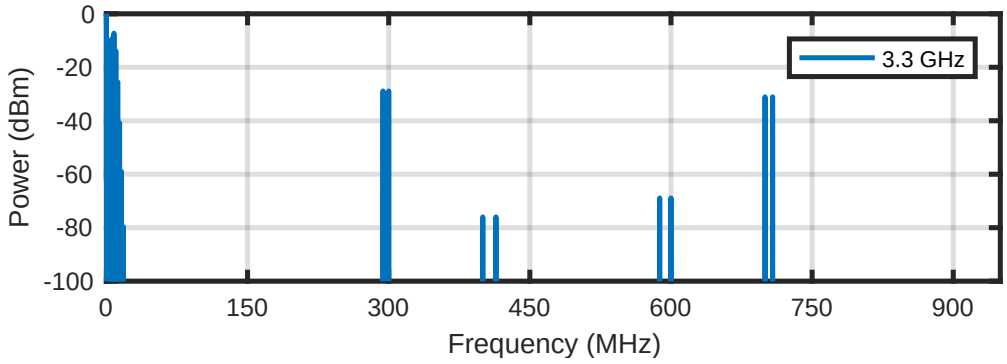

Fig. 5.9. Output beat-notes at baseband using a non-zero chirp MZM. The RF input (3.3 GHz) beats with both the third and fourth comb sidebands generating two pairs of beat-notes (at 300 MHz & 296 MHz, and 700 MHz & 708 MHz). The beat-note pairs at 600 MHz and 400 MHz arise from the second harmonic distortion.

5.4 Conclusion

We have demonstrated proof of principle experiments of a sub-sampling scheme that disambiguates over 10 Nyquist zones. The scheme can be easily tuned to cover ∼100 GHz by changing the drive frequency of the phase modulators to 10 GHz. The main limiting factor will be the frequency response of the employed intensity modulators. The tunability extends to the measurement time, which is ultimately set by the interferogram refresh time ($1/\delta f$). This implementation is optimized to enable potential integration of the setup. Using thin-film lithium niobate technology [8], substantial improvements in size, weight, and power consumption can be attained.

We have derived a theoretical model and obtain expressions for the analog link metrics. Our analysis shows that operating the link at null-bias eliminates second harmonic distortions, providing more than a 1000 fold improvement (30-35 dB) in SFDR. Analytical expressions for the conversion efficiency shows that it is possible to disambiguate over 16 Nyquist zones with a gain variation of only $\sim$ 8 dB using a modulation depth of 4.6π.

6. STIMULATED BRILLOUIN SCATTERING MITIGATION USING KERR COMBS FOR LONG-HAUL ANALOG OPTICAL LINKS

6.1 Introduction [1]

The emerging next generation cellular network (5G) revived an increasing interest in radio over fiber (RoF) solutions. To enable higher bandwidths and data rates, a shift towards new frequency bands centered at few GHz up to millimeter-Waves ($\geq$ 24 GHz) is being pursued. Backhauling/Fronthauling of such frequencies is a challenge, and RoF is a leading candidate. In addition to 5G networks, long-haul analog optical links are of interest to a variety of applications. In radio astronomy, analog photonic links are used for antenna remoting [145] and for the distribution of local oscillator to telescopes consisting of a large number of antenna array elements [146,147]. Other applications utilizing long fiber spools include military systems [148] and a host of optical processing techniques of RF signals [149]. Many of these applications have stringent phase noise requirements rendering midspan amplification not possible. It can be shown that the link noise performance and dynamic range improve with increased optical launch power at the photodiode (average photocurrent). However, for links exceeding a few kilometers, the link input optical launch is limited by stimulated Brillouin scattering (SBS), severely degrading the link performance.

SBS is an inelastic photon-phonon interaction with a low threshold nonlinearity. Exceeding the threshold results in an avalanche increase in scattered light and saturates the output power. In single mode fiber, SBS has a narrow gain linewidth ($\sim$16 MHz) and the phonon frequency is typically $\sim$ 11 GHz [150]. Techniques to circumvent SBS include concatenating fibers with different SBS frequencies [151], the use of

[1] The results in this chapter are adapted in whole or part from the publication [144]

few mode fibers [152] and frequency comb sources [153]. The frequency comb-based approach relies on the fact that SBS is narrowband effect. If the comb spacing exceeds the SBS gain bandwidth, the optical launch power can be increased by redistributing the average power over multiple spectral lines. As long as the power spectral density (PSD) within the SBS gain bandwidth is lower than the threshold, SBS can be mitigated. This technique allows increasing the link's optical launch power, thereby improving the RF link metrics at the expense of increased optical bandwidth.

As the understanding of Kerr combs is approaching maturity, their applications are increasingly expanding. Coherent digital optical communication is one example where Kerr combs have potential impact. In particular, recent experiments utilized Kerr combs for massively parallel wavelength-division multiplexing [154] and higher order 64-quadrature amplitude modulation coherent communication [155]. With growing interest in integrated RF photonics [156], analog microwave photonics, too, can benefit from Kerr combs. Recent investigations of microwave beamforming using microcomb-based true time delay networks [157, 158], illustrate that integrated Kerr combs are a valuable tool for next generation analog photonic links.

Here, we discuss the use of soliton Kerr combs for the mitigation of Brillouin scattering providing a careful comparison of soliton and dark pulse Kerr combs for Brillouin mitigation and characterize the RF link performance. In the first demonstration of comb-based Brillouin mitigation [153], an Electro-optic frequency comb based on cascaded intensity and phase modulators was used. However, low noise and highly stable broadband Kerr combs, fabricated in CMOS compatible processes, are an attractive alternative to EO-combs for multiple reasons. Reducing the footprint is a clear advantage. Additionally, since the link is operated as a sampled analog link, Nyquist sampling must be satisfied ($f_{RF,max} < f_{rep}/2$) in order to avoid aliasing. The electro-optic comb in [153] utilized a comb with 3 GHz comb spacing, which limited the Nyquist zone to 1.5 GHz. While bandwidths up to a few tens of GHz are common for commercial modulators, the halfwave voltage (V_π) for mmWaves significantly increases even with the state-of-the-art commercial modulators. This significantly in-

creases the power consumption which does not bode well for applications entailing a massive number of connected nodes, such as 5G and antenna remoting of telescope arrays. Recent advancements in thin film Lithium niobate (LiNbO3) are quite interesting, offering small footprints with reduced V_π and a wider RF bandwidth [8]. Nevertheless, they are still required to be driven by an amplified RF oscillator. Additionally, the bandwidth of the optical pulse scales linearly with the modulation index or RF-voltage. On the other hand, Kerr combs can have significantly larger bandwidth by engineering the dispersion, reaching an octave span [159]. Furthermore, scaling up the repetition of Kerr combs is actually easier, and combs with hundreds of GHz to 1-THz repetition rates have been achieved, enabling analog photonic links operating without aliasing at RF frequencies up to hundreds of GHz.

6.2 Experimental Setup

The experimental setup is shown in Fig. 6.1(a). A continuous wave (CW) pump laser is amplified by an Erbium doped fiber amplifier (EDFA). Dense Wavelength Division Multiplexing filters (DWDM) are used to filter the ASE. Lensed fibers are used to couple in and out of the microring. Another set of DWDM filters are used after the microring to block the strong pump line. Subsequently, the generated comb is modulated by an intensity modulator (IM) which is biased at quadrature and driven by the RF signal of interest. The IM is followed by a pulse shaper and a pre-link EDFA. The pulse shaper is used for amplitude shaping and spectrum flattening. No spectral phase mask is applied. The link consists of a 25 Km spool of single mode fiber (SMF) followed by a commercial dispersion compensating fiber module (DCF). We place a circulator before the link to measure the reflected power. After the link, a photodiode (PD) converts the signal back to the electric domain.

In this paper, we use two different silicon nitride (Si_3N_4) microring resonators. The first microring resonator has a radius of 100 μm corresponding to free spectral range (FSR) of $\sim$227.5 GHz. The ring's waveguide width is 2 μm, supporting two

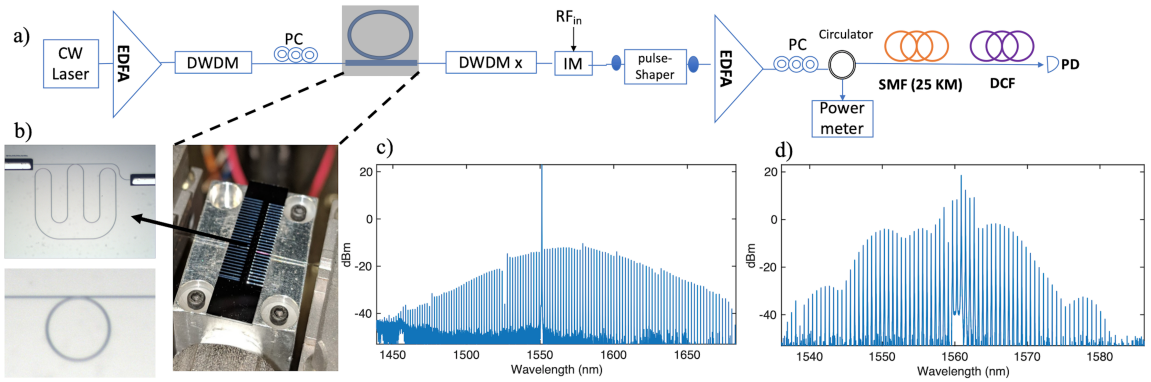

Fig. 6.1. (a) The experimental setup:- CW: Continuous wave, EDFA: Erbium doped fiber amplifier, DWDM: Dense Wavelength Division Multiplexing Filters, IM: Intensity Modulator. SMF: Single Mode Fiber. DCF: Dispersion Compensating Fiber. (b) Microscope images of the resonator and the chip mounted on the stage. (c) The spectrum of the soliton. (d) The spectrum of the dark pulse.

spatial modes, and its thickness is 790 nm leading to anomalous dispersion. The loaded quality factor of the resonance is 1 million. The wavelength of pump laser at 1551 nm is increased to tune into the resonance from the lower wavelength side initiating a chaotic high noise comb. The detuning is increased until a single soliton is formed. The average power in the fiber before the microring was 470 mW and the total fiber to fiber insertion loss was ∼3.8 dB. The spectrum of the soliton directly after the microring is shown in Fig. 1(c). The soliton's spectrum has a sech^2 envelope. The shift in the center of the soliton's spectrum towards higher wavelengths is a well-known signature of Raman soliton self- frequency shift [160]. Due to the soliton's low conversion efficiency, a prominent pump line is noticeable. We can define the pump conversion efficiency (η) as

$$\eta = \frac{P_{out,comb}}{P_{in,pump}} \tag{6.1}$$

where $P_{in,pump}$ is the is the pump power in the input waveguide and $P_{out,comb}$ is the power of the other comb lines (i.e., excluding the pump) at the waveguide output. Note that 100% conversion efficiency corresponds to a fully depleted pump and no

loss. For the single soliton, the measured pump conversion efficiency is 0.76%, which experimentally corresponds to a power of 2.5 mW in the new comb lines at the output fiber. A second microring, with a 73 GHz FSR, is used to generate a dark pulse. The ring has a width of 2 μm and a thickness of 600 nm leading to a global normal dispersion. The pumped resonance at 1561 nm has a loaded quality factor of 1.4 million and the fiber to fiber insertion loss was $\sim$3.8 dB. The pump is amplified to 600 mw in the fiber before the microring and tuned to generate a dark pulse that is mediated through mode interaction [161]. The pumped resonance was a single FSR away from the mode interaction region. This avoided mode crossing region shifts the resonance frequency resulting in an abrupt change in the dispersion profile which eventually leads to a local narrow anomalous dispersion region close to the pumped resonance, paving the way for the modulation instability process to occur and initiate comb generation. If the resonance that is two FSRs away from the mode interaction region is pumped, we observe two FSR spaced combs being generated. This is often referred to as mode-pining and is a typical signature of mode-interaction [162]. The dark pulse has considerably larger pump conversion efficiency: 10.31%, corresponding to 43 mw of power in the comb lines at the output fiber. The spectrum of the dark pulse directly after the microring is shown in Fig. 6.1(d). Note that the pump line power level is close to the newly generated comb lines. Dark pulses with even higher conversion have been achieved in [163], demonstrating 50 GHz dark pulses with 34% conversion efficiency.

6.3 Results

Herein, we compare the link metrics, namely: the increased SBS threshold power, the gain, third order intercept points, noise figure, relative intensity noise (RIN) and spurious free dynamic range (SFDR) for both the dark pulse and soliton with and without spectral flattening.

6.3.1 Stimulated Brillouin scattering threshold power

As mentioned earlier, Brillouin scattering is a narrowband effect. The effective SBS threshold power can be increased by redistributing the power over multiple spectral lines with a frequency spacing larger than the SBS gain bandwidth. Fig. 6.2 shows the average backscattered power at the reflection port of the circulator versus the link input power. With a CW input, the threshold power (P_{th}) is measured to be 6 dBm. Using the dark pulse and the soliton directly (with no flattening), the threshold power increases to 10.24 dBm and 14.88 dBm, respectively. When the spectrum is equalized to get a flatter envelope, the P_{th} of the flattened soliton increases to 16.69 dBm while the P_{th} of the flattened dark pulse increases to 19.23 dBm. The amplified flattened spectra at the link input are shown in Fig. 6.3. Due to the soliton's low conversion efficiency, the flattened soliton doesn't saturate the pre-link EDFA, which leads to a degraded optical signal to noise ratio (OSNR). From the acquired spectrum, we estimate that ∼13.5% of the total average power is ASE. On the other hand, the ASE constitutes only ∼ 0.1% of average power in the dark pulse.

The average output power at the end of the link (after the DCM in Fig. 6.1(a)), shown in Fig. 6.2, also scales with the number of spectral lines. For a CW input, the output power begins to saturate when the input power exceeds P_{th} by 2 to 3 dB. However, the situation differs for the other cases. Taking the direct dark pulse as an example; as the lines with stronger amplitude reach the Brillouin threshold, the weaker lines can still be amplified and pass through the link without experiencing SBS. Therefore; the output power does not saturate immediately after the P_{th}. To predict the increase in P_{th}, ref [153] defines an effective number of lines (N) as

$$N = 1 + \frac{\Delta f_{rms}}{f_{rep}} \tag{6.2}$$

where Δf_{rms} is the full root-mean-square (rms) bandwidth of the comb envelope and f_{rep} is the FSR. The SBS threshold power was modeled to scale linearly with N. The prediction from this model are accurate for combs with smooth envelopes. But for non-smooth envelopes such as the direct dark pulse, the predictions are far from the

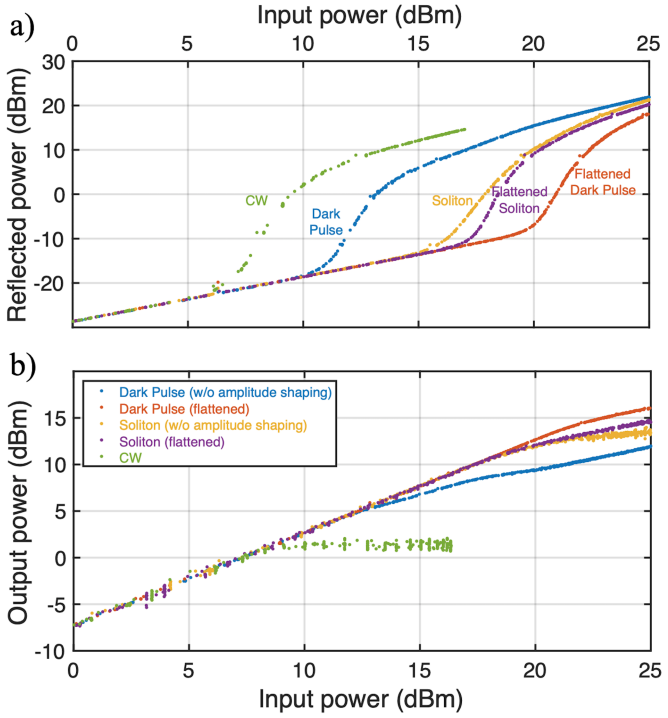

Fig. 6.2. (a) The reflected power and (b) the output power versus the link input power.

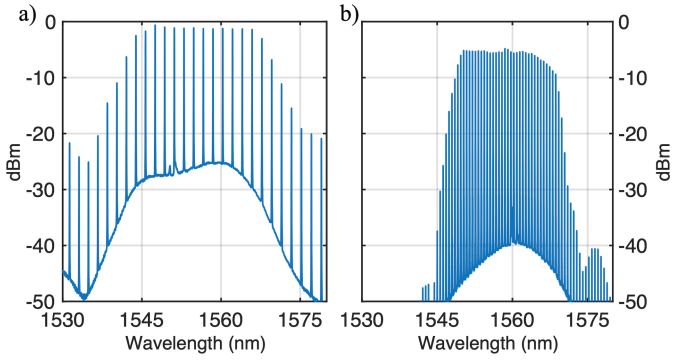

Fig. 6.3. The flattened spectrum of: (a) the soliton and (b) the dark pulse.

measured values. Alternatively, we use a different model based on the power spectral density in which

$$\Delta P_{th} = -10 \ \log \alpha \tag{6.3}$$

where α represents the fraction of the total average power in the spectral line with maximum amplitude. This model predicts a ΔP_{th} of 4.27 dB for the Dark pulse, which agrees well with the measured 4.24 dB. For flattened spectra, this model gives results that closely agree with measured values but becomes sensitive to the optical spectrum analyzer's power accuracy and to the variations in the EDFA spectral gain distribution. On the other hand, the method based on the rms bandwidth averages out these fluctuations and gives better predictions.

Table. 6.1 summarizes the results. Note that the FSR of the soliton is ∼3 times higher than the dark pulse. Ideally the comparison would be better with equivalent FSRs. However, achieving ∼70 GHz cavity solitons with conventional CW pumping, while theoretically possible, is practically still challenging. The increased losses and stimulated Raman effect reduce the soliton existence range. Combined with thermal effects, these make the generation of and locking to the single soliton state challenging. An order of magnitude improvement in the quality factor to tens of millions can substantially expand the soliton existence range, potentially paving the way for solitons at microwave rates [164].

Table 6.1.
Increase in SBS threshold.

	Measured P_{th} (dBm)	Measured ΔP_{th} (dB)	$\Delta P_{th} = 10 \log N$	$\Delta P_{th} = -10 \log \alpha$
CW	6	-	-	-
Soliton	14.88	8.88	8.99	8.53
Soliton (flattened)	16.69	10.69	10.17	11.53
Dark Pulse	10.24	4.24	8.88	4.27
Dark Pulse (flattened)	19.23	13.23	13.24	14.21

6.3.2 RF gain and 3rd-order intercept points

For an externally intensity-modulated direct-detection link architecture, it is well known that the gain and third order output intercept point (OIP_3) improve with increased average photocurrent (I_{dc}). By allowing higher power at the photodetector, the increased P_{th} directly improves the link performance. The links here are operated at 1-dB below the corresponding SBS threshold for each comb source used. This results in an average photocurrent of 8 mA, 5.1 mA and 3.2 mA for the flattened dark pulse, flattened soliton and direct soliton, respectively. Note that for the direct soliton, we bypass the pulse shaper to avoid the unnecessary $\sim$ 7 dB insertion loss.

We measure the OIP_3 by the conventional two-tone test at a frequency f_1 of 5 GHz and a second tone at $f_2 = 5.01$ GHz. The fundamental tone output versus the input RF average power is plotted in Fig. 6.4 alongside the 3^{rd} order intermodulation distortion (IMD) at ($2f_2 - f_1 = 5.02$ GHz). In all cases, the fundamental tone has a slope of 1 while the IMD's slope is 3 as expected. The intersection of two linear fits defines the OIP3 and the 3rd order input intercept point (IIP3). Theoretically, the IIP3 depends on the modulator's frequency-dependent halfwave voltage V_π and is independent of the average photocurrent [150], and can be expressed as

$$IIP_3\ [dBm] = 10\ \log\left(\frac{4{V_\pi}^2}{R_i\pi^2}\right) + 30 \tag{6.4}$$

where R_i is the input resistance of the intensity modulator (50 Ω). The OIP_3, on the other hand, depends on the average photocurrent current but not V_π , and can be found using

$$OIP_3\ [dBm] = 10\ \log\left(4R_oH_{pd}^2I_{dc}^2\right) + 30 \tag{6.5}$$

where Ro is the load resistance (50 Ω) and $H_{pd} = 1/2$ is the photodiode response function included to account for the matching circuit. The measured IIP3 for all three cases is $\sim$22.5 dBm, which is in close agreement with theoretically expected 22.08 dBm given $V_\pi = 4.46$ V. For the flattened dark pulse and the direct soliton, the measured OIP_3s of 4.1 dBm and -4 dBm are in good agreement with the theoretically

expected values: 5.05 dBm and -2.9 dBm. The flattened soliton has an OIP_3 of -2.27 dBm which is 1.14 dB lower than the expected value.

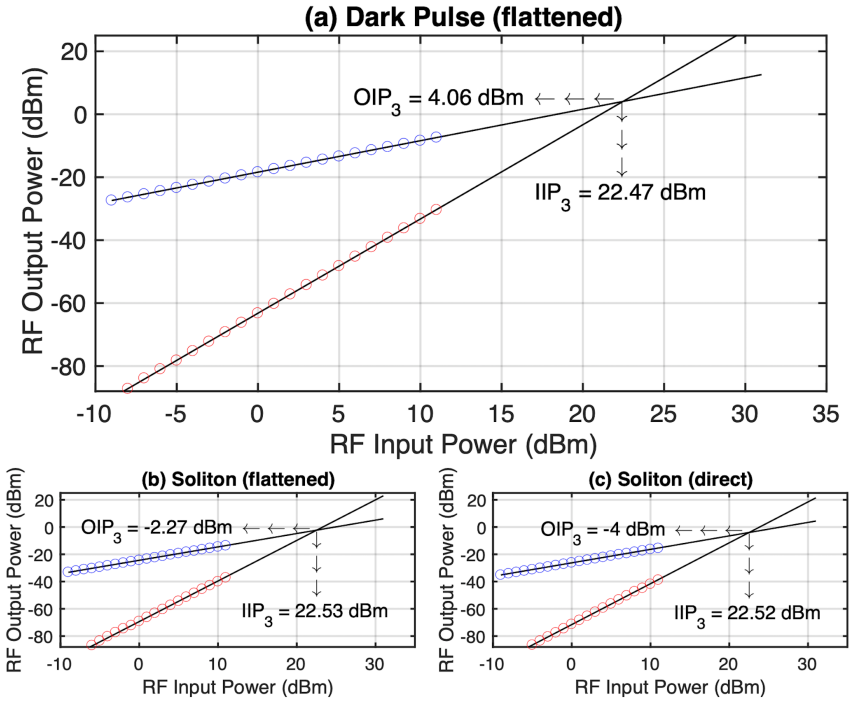

Fig. 6.4. Measured fundamental (blue) and IMD (red) powers at 5 GHz. The black lines are a fit to the measured data and their intersection defines the 3^{rd} order intercept points.

The gain in an intensity-modulated direct-detection (IMDD) link is proportional to the square of I_{dc}/V_π ratio. Ref [153] shows that the same expression applies for an IMDD sampled analog link assuming the pulses at the IM are transform limited and given that any subsequent chromatic dispersion is compensated. If not compensated, chromatic dispersion can induce filtering and tapped delay line effects [165], in addition to even-order harmonic distortion [153]. The gain can be found using

$$Gain\ [dB] = 10\ \log\left(R_i R_o \left(\frac{\pi H_{pd} I_{dc}}{V_\pi}\right)^2\right) \tag{6.6}$$

Fig. 6.5 shows the measured link RF gain across an 18 GHz bandwidth. In sampled analog links, if larger SBS thresholds and larger RF bandwidth are needed, requiring larger optical bandwidths and larger FSRs, residual dispersion becomes important. In

our setup, the commercial DCF module is designed to cancel the 2_{nd} order dispersion but not the 3^{rd} order dispersion. To separate the dispersion-based roll-off in gain from the instrument (IM and PD) response, we also measure and plot the normalized instrument response. The flattened and direct soliton have the same roll off profile with roughly 6 dB of additional roll off in gain at 18 GHz arising from residual dispersion. At 5 GHz, the measured -27.3 dB RF gain of the direct soliton is close to the expected -25 dB, while the flattened soliton case results in a RF gain of -25 dB, 4 dB lower than the expected theoretical value. This deviation is likely in part due to the fact that the ASE constitute a nonnegligible 13% of the total optical power, which we expect to account for a drop of 1.2 dB in gain. The rest of the roll-off is mostly due to residual dispersion. The dispersion-based gain roll-off of the dark pulse is less than the soliton due to its relatively smaller bandwidth. The dark pulse's measured response mostly follows the instrument response with a deviation of ~2.7 dB around 10 GHz. The measured gain at 5 GHz, -19.4 dB, is close to the theoretically expected -17 dB.

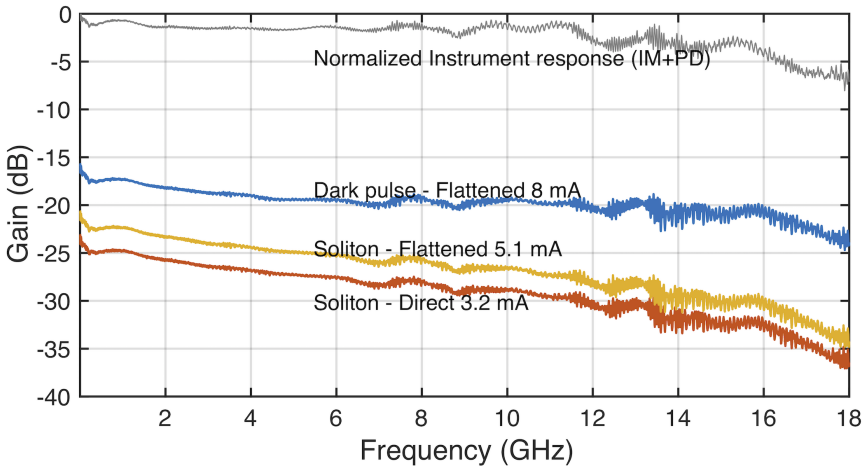

Fig. 6.5. The measured link RF gain.

With increasing bandwidth (both optical and RF), more precise dispersion compensation will become desirable. This can be achieved by using dispersion compensating fiber with optimized dispersion slope. Residual higher order dispersion can

be cancelled using line by line pulse shaping. Ref [166] demonstrates the ability of pulse shaping to compensate for residual higher order dispersion over a 50 Km link compressing a pulse to its transform limited duration of 500 fs, more than sufficient for microwave photonic applications. This shows that while dispersion should not be neglected, it need not be a limiting factor. Note that if the full dispersion is left uncompensated, the link then becomes essentially a comb-based RF photonic filter [165]. The Brillouin suppression effect observed here should also occur in such comb-based RF photonic filtering experiments, contributing to favorable RF metrics.

6.3.3 Relative intensity noise and noise figure

To determine the link dynamic range and noise figure, we need to quantify the noise performance. The link noise includes contributions from thermal noise, shot noise, laser relative intensity noise and EDFA added noise. At frequencies higher than 100 MHz, the noise is typically limited by the signal-ASE beat noise. The signal-ASE beat noise decreases as the required gain of the EDFA decreases [167]. Therefore, we expect the Kerr comb conversion efficiency to have a direct effect on the noise performance. Indeed, as shown in Fig. 6.6, the flattened dark pulse RIN is 3 to 4.5 dB lower than that of the direct soliton. While the flattened soliton has a higher SBS threshold and gain than the direct soliton, a hefty price is paid in noise performance. The soliton's low conversion and losses arising from flattening and the pulse shaper's insertion loss leave insufficient optical power to saturate the EDFA. On average, the flattened soliton RIN is $\sim$7.5 dB larger than the direct soliton, reaching -131 dBc/Hz at 5 GHz.

Although some links have been operated above the SBS threshold [168], the general practice - which we so far adopt - is to operate below the threshold. The rationale behind this is the following: for the CW case, as the input power is increased by a couple of dBs above the threshold, the output power is clamped at certain value. In other words, the loss increases; thereby increasing the noise figure. Nevertheless, this

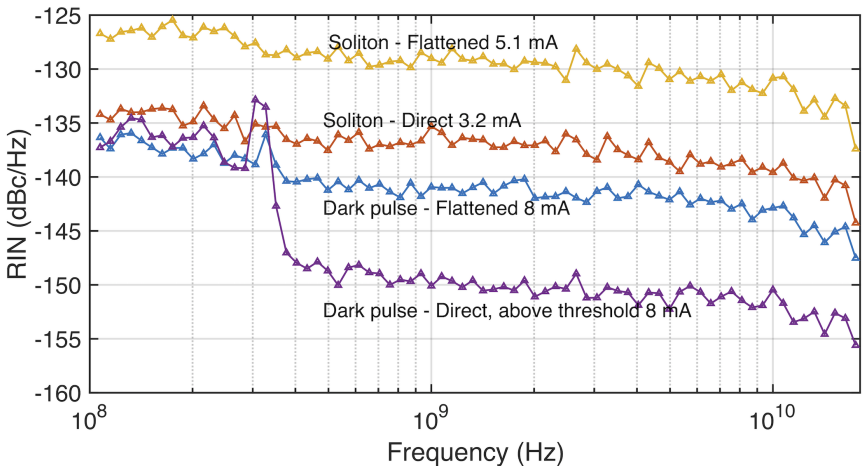

Fig. 6.6. The link output noise density displayed as RIN.

is not always the case. As previously mentioned, for a non-uniform spectrum, such as the direct dark pulse, with FSRs exceeding the narrow SBS gain bandwidth, the power of the few spectral lines exceeding the SBS threshold gets saturated, but other weaker spectral lines pass the link without experiencing SBS; thereby achieving an overall net gain. To test this, we operate the link using the direct dark pulse above the threshold. To compare it with flattened dark pulse, we operate both cases with optical powers resulting in 8 mA of average photocurrent. At frequencies lower than 300 MHz, both cases have similar RIN levels. However, the direct dark pulse RIN level decreases by 7.5 to 10 dB at frequencies higher than 400 MHz. We also notice a peak at $\sim$ 310 MHz in the dark pulse response. Kerr combs are known to have a peak at a relaxation frequency which is on the order of the resonance linewidth [169]. Pump amplitude and phase noise conversion in Kerr combs through the four-wave-mixing (FWM) process may contribute to the noise observed below 300 MHz [170]. While not within the scope of this paper, a detailed comparison of the pump amplitude and phase noise conversion between dark pulses and solitons is of interest. Conversion of phase noise to intensity noise arising from SBS [171], which intensifies above the threshold, may be acting in concert with the pump noise conversion in Kerr combs leading to the marginal increase in the direct dark pulse RIN at lower frequencies.

Additional care must be taken for the X-band when operating above the threshold. The backscattered stokes wave that is frequency-shifted by the Brillouin frequency (∼11 GHz) can experience Rayleigh scattering and co-propagate with the original beam resulting in increased noise at ∼11 GHz [172]. While we don't observe increased noise levels at that region, our sampling points aren't dense enough to conclusively determine its absence.

Now that we have the RF gain and noise measured, we calculate the noise figure using

$$NF = \frac{N_{out}}{G_{RF}\ k_B T} \tag{6.7}$$

where $k_B T$ represents the thermal noise contribution (k_B is Boltzmann's constant and $T = 290$ K), G_{RF} is the RF gain and N_{out} it the total electrical noise power spectral density at the link output. The results are shown in Fig. 6.7. The flattened soliton has a mediocre noise figure exceeding 61.5 dB across all the frequency band. The direct soliton also has flat noise figure of $\sim$ 53.6 dB at 5 GHz; significantly higher than the shot noise limited noise figure by 21.4 dB. Note, shot noise-limited performance is typically desired in high-performance analog optical link applications. The flattened dark pulse noise figure is ∼3.6 dB lower than the direct soliton. Nevertheless, this is still 21.9 dB higher than the shot noise limited noise figure. Using the direct dark pulse operated above the threshold, the NF significantly drops at high frequencies by ∼13 dB. The resulting level is only 11.75 dB short above the shot noise limited noise figure at 5 GHz. Common noise cancellation using balanced detection can suppress the frequency comb's RIN. If the EDFA is placed before the modulator, the sig-ASE noise becomes common-mode and can be suppressed, potentially reducing the noise figure to the shot noise limited regime [173].

6.3.4 Spurious-free dynamic range

The SFDR is defined as the range of input powers over which the output signal power of the fundamental exceeds the output noise floor and all other third-order

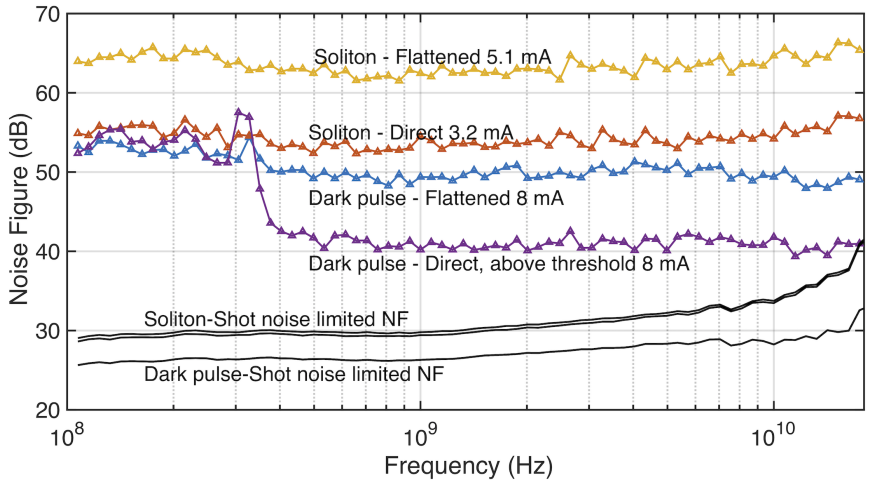

Fig. 6.7. The measured link noise figure.

spurious signals (which are close to the fundamental and cannot be filtered out) are less than or equal to the noise floor [150]. The dynamic range in a quadrature-biased IMDD link is 3^{rd} order limited. Given that the OIP_3 depends on the average photocurrent and theoretically is frequency independent, we use the measured gain and noise to calculate the $SFDR_3$ using

$$SFDR_3 = \left(\frac{OIP_3}{N_{tot}\ B_e} \right)^{2/3} \tag{6.8}$$

where B_e is the electrical bandwidth of the noise measurement (set to 1 Hz). At 5 GHz, the flattened dark pulse has a $SFDR_3$ of 98 $dB \cdot Hz^{2/3}$, 9 dB higher than the flattened soliton. The direct dark pulse at frequencies higher than 400 MHz has the highest $SFDR_3$ and achieves a 104.8 $dB \cdot Hz^{2/3}$ $SFDR_3$ at 5 GHz, matching the performance of the well-established electro-optic combs [153]. The SFDR3 increases at high frequencies (∼18 GHz) reaching 107 $dB \cdot Hz^{2/3}$. These results constitute one of the few demonstrations of chip-based RF-photonic platforms exceeding 100 $dB \cdot Hz^{2/3}$ SFDRs [156].

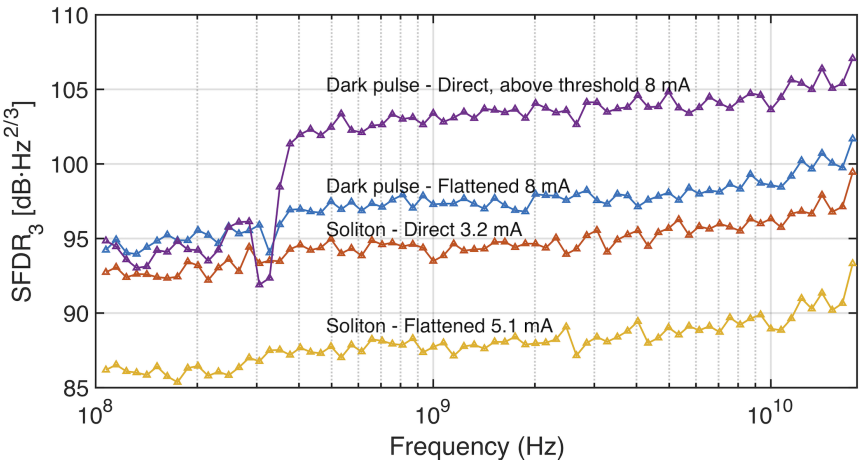

Fig. 6.8. The extracted spurious free dynamic range.

6.4 Conclusion

By mitigating SBS using Kerr combs in an IMDD sampled analog optical link architecture, we demonstrate long-haul transmission in a 25 Km link achieving high SFDR_3. The pump conversion efficiency of different Kerr combs shows a direct effect on the link noise figure. The flattened dark pulse increases P_{th} by 13.2 dB, while the direct soliton achieves a ΔP_{th} of ∼10.7 dB. Although the dark pulse conversion efficiency is an order of magnitude higher than the single soliton, the losses in the flattening stage make the improvement in dynamic range smaller ($\Delta\mathrm{SFDR}_3 \approx$ 2.4 dB). While in this paper we compare single solitons and higher order dark pulses, a plethora of other Kerr comb solutions exist. In particular, the lowest order dark soliton has a smooth spectrum and a ∼10% pump conversion efficiency [174]; thereby circumventing the need for a flattening stage and potentially achieving a dynamic range equal to or exceeding ∼105 $dB \cdot Hz^{2/3}$. Higher order dark pulses with 30% conversion efficiency have been demonstrated as well [174]. If pump reject filters and the IM are integrated with the microresonator well within reach of existing technology the loss in the system will decrease, and the optical signal can potentially be sent directly to link operating at or slightly above threshold as demonstrated. The EDFA

can then be moved after the link operating at its full power. Paired with high photocurrent handling balanced detectors, such a setup promises dramatic improvements in RF gain and dynamic range.

7. INTEGRATED ATOMIC-OPTICAL CLOCKS

The clock is ticking! But have you ever paused to think about what defines time and how accurately can you measure it? As societies grew more complex, their schedules needed to be ordered and synchronized. Naturally, early attempts relied on the sun as a source of measurements, eventually leading to the development of sundials. As the earth rotates around its axis - or the sun appears to move along the sky - its shadow trail can be divided into a standard of 12 markers or hours. Of course, such counting systems will lead to different cycles or times at different latitudes, moreover, it can't be used during nighttime! Motivated by the need of various religions to coordinate and measure prayer times, various time counting methods were developed over the centuries. Water clocks and sandglasses relied on the calibrated flow of water or sand from on container to the other. In the 17^{th} century, Galileo's realization that the oscillation period of a pendulum depends on its length paved the way for Huygens to develop the first pendulum clock. Later in the 20^{th} century, the discovery of the piezoelectric effect led to its rapid utilization in radio broadcasting and ultimately timekeeping.

Each of these clock counting methods has a different inaccuracy level, which over time builds up to noticeable differences. In fact, this is the origin of the phrase 'o'clock", i.e. "of the clock"—a phrase that was used to distinguish time measured based on mechanical clocks from sundial clocks. The trend of developments in clocks shows a quest for a source with a natural or intrinsic oscillation that is universal and independent of fabrication or size. Secondly, it was clear that a shift towards a higher oscillation frequency gives better inaccuracies; miscounting one cycle of a 1 Hz oscillator leads to an error of 1 second compared to 1 ns for a 1 GHz clock. Clocks based on the measurement of atomic transitions satisfied both criteria. Cesium (Cs) clocks have led to frequency standards with unprecedented accuracy and instability

so much so that in 1967, the SI second was redefined as the "duration of 9,192,631,770 periods of the radiation corresponding to the transition between the two hyperfine levels of the unperturbed ground state of the Cesium atom." Current state-of-the-art Cs fountain clocks can reach an instability level of 0.01 ns per day ($\sim 10^{-16}$). Furthermore, moving to atoms or ions with optical transitions has led to far more superior clocks approaching an instability 10^{-17} within seconds! However, these clocks came with a big challenge: how can you count the cycles of a clock oscillating $\sim 100s \times 10^{12}$ times in a second? This dilemma was solved by introducing fully stabilized optical frequency combs as we will explain in this chapter. Using such a method, a recent work successfully transferred the optical stability to a 10 GHz signal in the electrical domain, yielding a fractional instability of 1×10^{-18} in 44,000 seconds [175].

The importance of timekeeping and its applications are so ubiquitous that we take it for granted every day. From the 1-Hz ticks of your analog clock to the 60-Hz power grid signal charging your electronics and the wireless communication networks, they all rely on tight synchronization to function properly. Another major technological breakthrough is the global positioning system (GPS), which relies on synchronized atomic clocks placed on multiple satellites broadcasting precisely timed signals, allowing the user to triangulate his location. The unprecedented stability offered by atomic clocks opens the doors to tests of general and special relativity [176–178], measurements of fundamental constants [179], radio astronomy by long-baseline interferometry [180], geodesy [181] and gravitational wave detection [182].

Current atomic-optical clock apparatuses are based on bench-top setups, involving complicated laser-based setups for atomic trapping, cooling, and interrogation, as well as a stabilized OFC for frequency division. In this chapter, we report on our *ongoing progress* in an ambitious project aiming to develop a fully integrated atomic-optical clock as part of a larger team led by Sandia National Laboratory. Sandia will take up the gauntlet of integrating a Ytterbium (Yb) ion trap including all the optical assembly required for trapping and probing the ~ 435.5 nm quadrupole transition in $^{171}Yb^{+}$. A 'clock' laser at 871 nm based on a low-linewidth based on a self-injection

technique with a whispering gallery mode technique will be developed by OE waves, and subsequently, frequency-doubled using thin-film LN waveguide developed by the group of Prof. Hong Tang at Yale.

At the end of phase 2, the program targets a clock system with a power consumption of 10 W or less that fits with half a liter of volume. Only one free space element is allowed, and the clock's output frequency should be within 10 MHz - 20 GHz with a fractional instability of $10^{-14}/\sqrt{\tau}_{av}$ where τ_{av} is the averaging time. Our focus at Purdue is the development of an integrated OFC system capable of coherently dividing the clock laser within the requirements of the program. The OFC is based on a Si_3N_4 Kerr comb fabricated at Purdue by the group of Prof. Minghao Qi. Additionally, we have collaborated with Prof. Victor Torres-Company at Chalmers to fabricate some devices using their optimized subtractive process [26]. I will first briefly introduce the concept of f-2f stabilization and using dispersion engineering to generate octave-spanning combs. I'll then discuss initiating a soliton and mitigating destabilizing thermal effects. Subsequently, I'll propose a novel method to optically divide and detect the repetition rate of a large FSR Kerr comb using dual Vernier combs. Afterward, I will discuss multiple schemes to stabilize and lock the comb to the clock laser and propose one for phase-2 of the project that overcomes the low comb line power limitations using Kerr combs. Finally, I'll conclude by listing the remaining challenges and possible remedies.

7.1 f-2f Stabilization

As previously introduced, a remarkable feature of OFCs is that each optical comb line is defined by two microwave frequencies: f_{ceo} and f_{rep}. This facilitates the readout of clock lasers locked to atomic transitions. By optically heterodyning and locking a comb line to the clock laser, and stabilizing f_{ceo}, the comb divides the clock laser down to f_{rep}, which is typically obtained by photodetecting the pulse train. The

comb provides a phase-coherent link connecting the optical domain to the microwave domain.

Locking of f_{ceo} is commonly accomplished by the f-2f scheme. Having an octave-spanning comb containing the following comb lines

$$\nu_n = f_{ceo} + nf_{rep} \tag{7.1}$$

$$\nu_{2n} = f_{ceo} + 2nf_{rep}, \tag{7.2}$$

doubling of the low-frequency line (ν_n) then heterodyning it with ν_{2n} leads to

$$\begin{aligned} 2\nu_n - \nu_{2n} &= 2f_{ceo} + 2nf_{rep} - f_{ceo} - 2nf_{rep} \\ &= f_{ceo} \end{aligned}$$

After detection, the CEO frequency is compared to and locked to a frequency reference (e.g. Rubidium or Quartz oscillator) through a feedback phase-locked loop (PLL). The general stabilization setup is shown in Fig. 7.1, the CEO beat note is mixed with a stable rf reference. Since most rf references are at a low frequency, a frequency divider preceding the rf mixer is typically needed. After the mixer, a phase-frequency-detector followed by a charge pump generates an electrical signal that serves as the error signal to a laser servo. This proportional-integral-derivative (PID) controller servo generates a feedback signal to stabilize the OFC. Typically, for mode-locked lasers, this feedback signal controls either the pump laser's intensity or modifies the cavity's length using a piezo-actuated mirror. For Kerr microcombs, this feedback signal controls either the power of the pump laser or the detuning of the pump laser (e.g. by controlling the laser frequency) [159, 183, 184].

Note that, generally, an ambiguity in the frequency sign exists, and can be resolved by dithering the repetition rate and observing whether the f_{ceo} frequency increases or decreases. Other schemes to detect the CEO include the 2f-3f locking scheme which adds another frequency conversion stage but requires two-thirds of an octave [185]. To fully stabilize the comb, a second lock is needed to either stabilize the repetition rate or to lock a comb line to a stable optical reference.

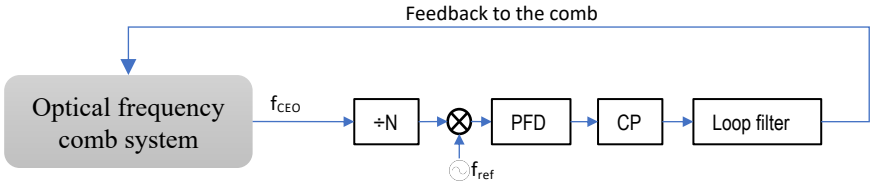

Fig. 7.1. Schematic of an optical phase locked loop circuit, where PFD stand for phase frequency detector and CP is charge pump.

7.2 Octave-Spanning Kerr Combs

From the last section, we see that the first step of f-2f stabilization is to acquire an octave-spanning comb. Most demonstrated Kerr combs typically span ≤ 400 nm. For a cold cavity microring with dominant second-order dispersion, the dispersion shifts the periodicity of the resonance frequencies causing a gradual slip away from an equidistant grid. Eventually, the energy conservation and phase-matching condition can't be simultaneously satisfied, thereby limiting the comb's bandwidth. The dispersion coefficient typically used in the ultrafast optics literature can be converted to

$$D_n = \frac{-\beta_n v_g}{(-D_1)^n} \tag{7.3}$$

such that the cavity's resonance angular frequencies can be expressed as

$$\omega_\mu = \omega_{\mu_o} + \sum_{n=1}^{N} \frac{D_n}{n!}\mu^n \tag{7.4}$$

where v_g is the group velocity, $D_1 = 2\pi \cdot FSR$, ω_{μ_o} is the angular frequency of the pumped resonance, μ is an integer representing the resonance mode number relative to the pumped resonance.

In general, the cavity dispersion arises from two components: the intrinsic material dispersion, and the waveguide dispersion. By carefully engineering the waveguide dimension - thus the dispersion - the higher-order dispersion terms can 'bend' the curve causing the shifted resonance modes to approach the equidistant grid again. An example is shown in Fig. 7.2, where two zero-crossings can be seen. At these

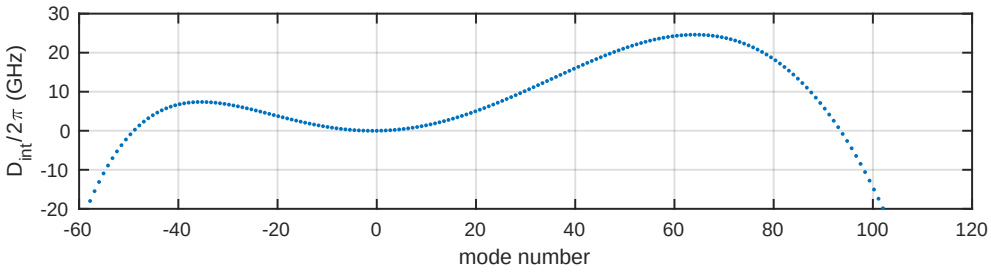

Fig. 7.2. Dispersion engineering to achieve two zero crossing points generating dispersive waves that make f-2f locking possible. Dispersion profile was simulated by Cong Wang.

crossing, the resonance coincides with the equidistant grid (relative to the pump resonance), satisfying the phase-matching condition and emitting a 'dispersive wave' extending the spectrum's wavelength span.

The dispersion profile shown is based on a waveguide dispersion simulation of a ring with 25 μm radius corresponding to a FSR of $\sim$ 903 GHz, and a width and thickness of 1600 nm and 740 nm, respectively. The simulated dispersion is based on refractive index measurements obtained from our collaborators at Chalmers. Using the LLE equation (eq.1.3), we simulate the nonlinear dynamics of soliton generation taking into account the full dispersion curve and assuming critical coupling with a loaded quality factor of 1 million and a CW pump power of 75 mW at the bus waveguide. The simulation includes Raman effects as well [186]. Tuning into the resonance from the low wavelength side, the detuning is increased linearly until a stable soliton is obtained at a final detuning of 1.96 GHz. The spectrum of the single soliton is shown in Fig. 7.3. Two distinct spectral peaks at $\sim$ 2.1 μm and $\sim$ 1.05 μm extending the soliton's spectra to an octave. These dispersive waves can enhance the spectral power by more than 20 dB, making f_{ceo} locking through the f-2f scheme a viable option.

The spectrum shown in Fig. 7.3 is the *intracavity* spectrum, however, extracting this octave onto the bus waveguide is a challenge. The evanescent coupling to

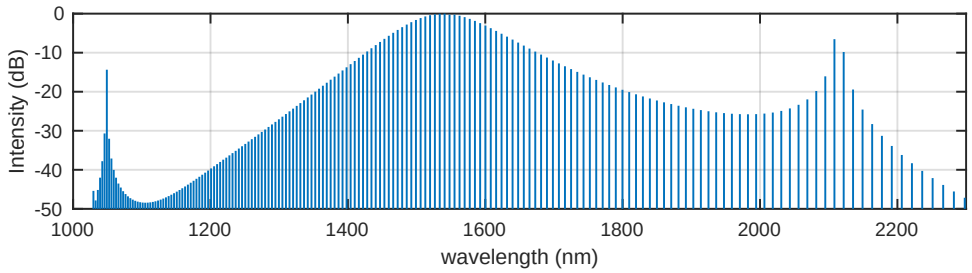

Fig. 7.3. LLE simulation of the an octave-spanning Kerr comb with two dispersive waves.

the bus waveguide depends on the gap between the bus and ring waveguide, and is heavily wavelength dependent. The typical coupler section design involves a straight waveguide with a fixed gap chosen to satisfy the desired coupling condition (i.e. critical, undercoupled, or overcoupled). However, straight waveguide couplers suffer from poor extraction of short wavelengths. Instead, using a pulley structure–where the bus waveguide is curved around the ring–increases the interaction length, thereby allowing improved coupling of shorter wavelengths [187].

7.2.1 Experimental results

Dispersion engineering is easier said than done. The process requires exquisite control of the fabrication process, repeatability, and on top of all, a very accurate measure of the films' refractive index—both the oxide cladding and the Si_3N_4 film. That said, statistical variations in deposited film thickness and quality are inevitable even at the industrial foundry level, let alone shared academic clean-room facilities. To overcome these variations, fine sweeps of the design parameters are needed. Of course, wafer-scale fabrication requires wafer-scale characterization! A significant portion of the project was dedicated for process development, which entails multiple fabrication runs separated by linear characterization (i.e. insertion loss, coupling, and quality factor measurements) as well as nonlinear characterization (comb generation),

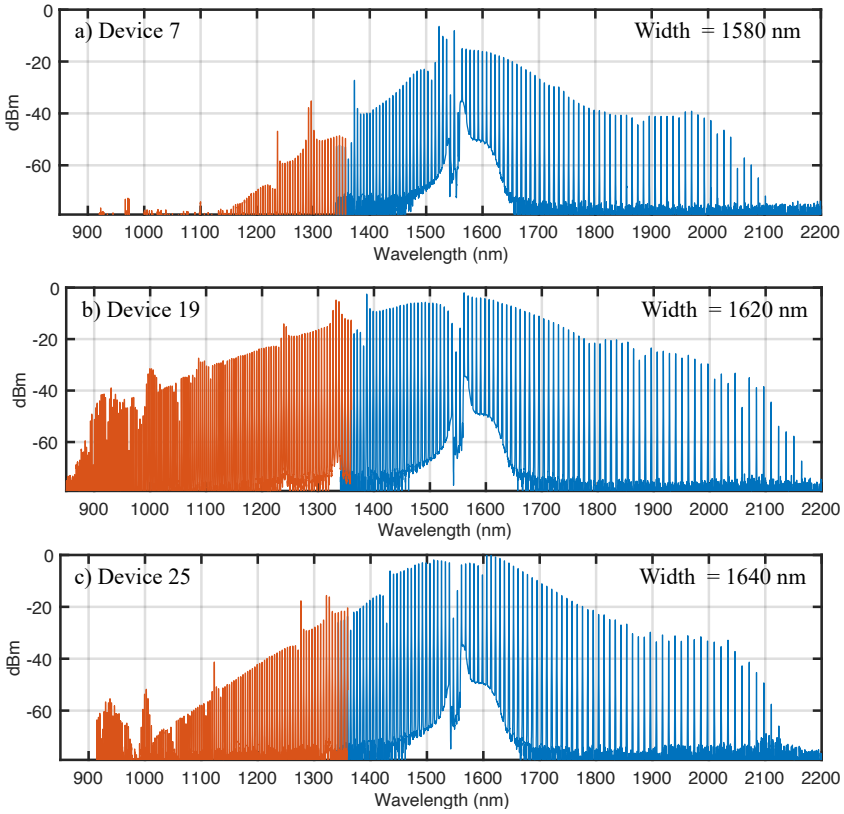

Fig. 7.4. Dispersion engineering: Effect of fine sweeps in ring-width on the soliton spectrum. The ring's waveguide width in a), b) and c) is 1580 nm, 1620 nm, and 1640 nm, respectively. The spectra were acquired using two different optical spectrum analyzer highlighted by a different color.

which in turn guide the designs and feed back to the fabrication process. Several designs were considered focusing on generating $\sim$ 1 THz and 500 GHz rings for pumping wavelengths of $1.55\mu m$ and $1\mu m$. The best results have been achieved using the $\sim$ 1 THz rings at $1.55\mu m$. My intention here is not to survey the results of the performed fabrications; instead, I will focus on the successful results that we have obtained and I will try to -hopefully- convey the sensitivity of the process to the fabrication and waveguide dimensions.

One of the first parameters to vary is the ring-width. The comb's bandwidth shows a strong and clear dependence on the ring-width as expected from dispersion

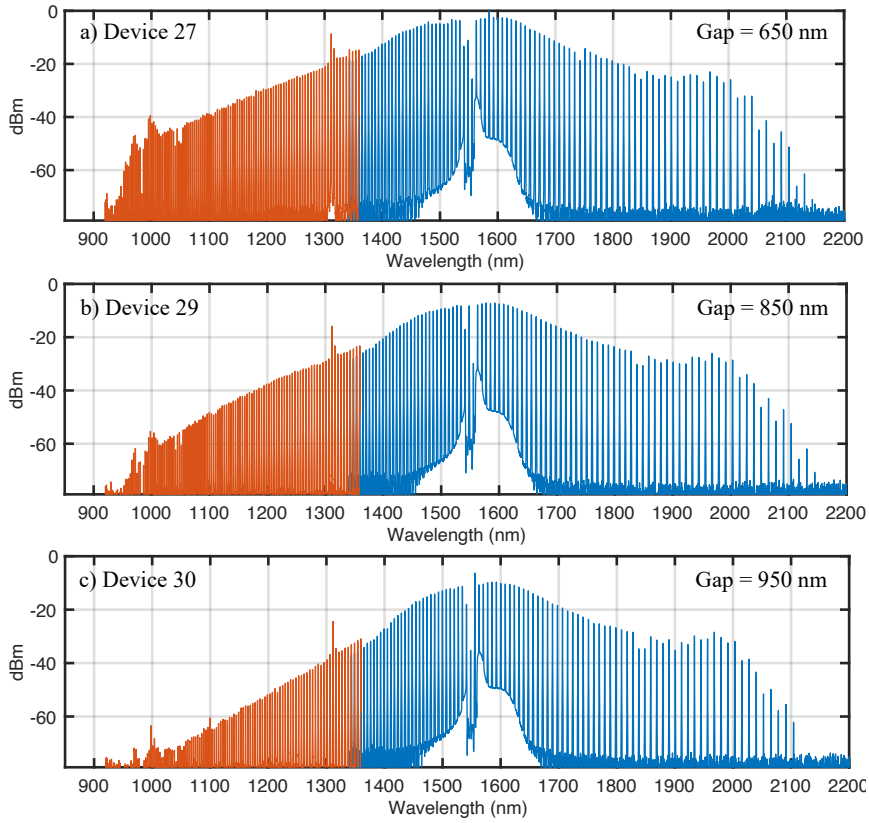

Fig. 7.5. Effect of increasing the coupling gap width. The gap in a), b) and c) is 650 nm, 850 nm, and 950 nm.

simulations. Figure 7.4 shows three comb spectra generated using devices fabricated at Chalmers with a ring-width of 1580 nm, 1620 nm, and 1640 nm. A clear octave-spanning comb is generated using the 1620 nm device, and even a mere 20 nm increase in ring-width narrows the comb bandwidth to a -practically- sub-octave! While dispersion simulations support two dispersive waves for all devices, LLE simulations indicate that coherent soliton formation is not assured by the former. If the dispersion offset is too large, soliton formation is prohibited, but more analysis and simulation is required to quantify and determine if indeed a hard limit on the dispersion mismatch exist.

To efficiently extract the octave, we used a pulley coupler and added variations in the coupling gap to probe the best designs. For the batch of devices with a ring-

width identical to that of the octave-spanning comb, the coupling gaps available was 650 nm, 850 nm, and 950 nm. We clearly observe that the coupling, particularly, at 1 μm, is increased. The devices with narrower gaps were damaged during the fabrication process, but an example from another wafer (see Fig. 7.6c) suggests that a gap of 450 nm can further improve the coupling as lines even at 900 nm are visible.

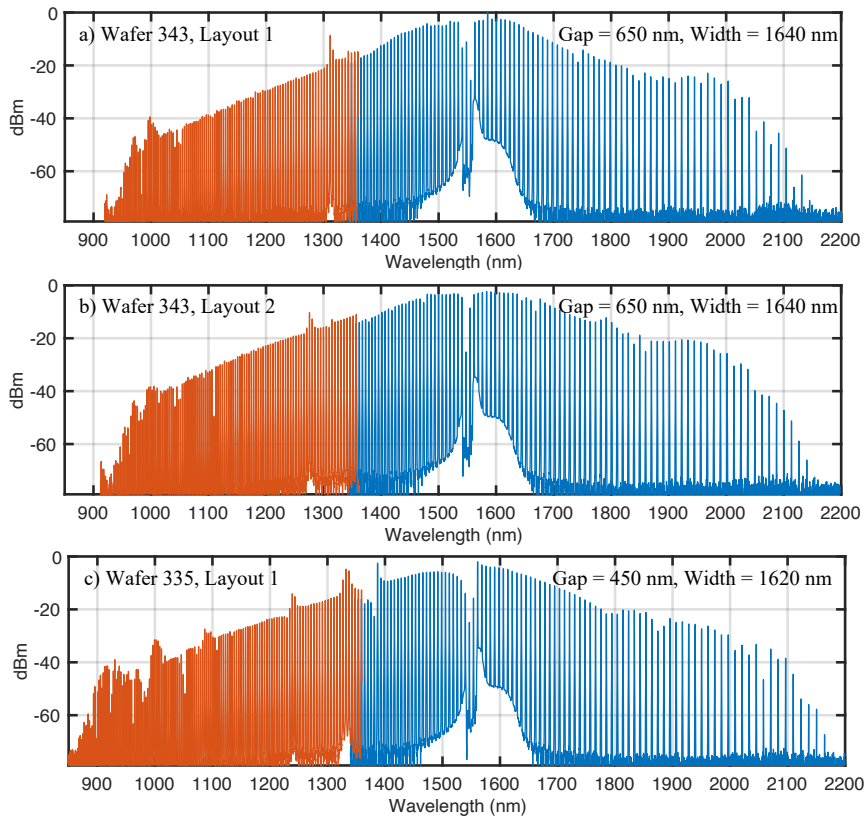

Fig. 7.6. Multiple Octave-spanning combs from two wafers.

In the fabrication run with Chalmers, a layout containing 47 rings of different FSRs and waveguide dimensions were designed and a second layout with identical parameters except a slightly smaller FSR was designed as well. The two layouts were fabricated using the same wafer, then replicated on a second wafer as well. On average, $\sim$ 10 rings in each layout were lost due to a Si_3N_4 exposure malfunction during the fabrication, these were unfortunately mostly centered at the location of devices with desirable ring-widths. Nevertheless, three octave-spanning combs with

practically appreciable powers at the edges of the spectra were obtained, and those examples were obtained from two separate wafers. The spectra are shown in Fig. 7.6, it is interesting to note that the layouts from the same wafer generate the broadest combs using a device of 1640 nm ring-width, while the broadest combs in the other wafer occur with devices having a ring-width of 1620 nm. The difference might have arose from a change in refractive indices between the two wafers, or due to a few a nanometer difference in thickness.

7.3 Soliton Initiation

The spectra shown in previous sections are all chaotic or incoherent spectra that can't be used to transfer the stability of the clock laser. To generate and access the soliton region with a CW pump, the pump is typically detuned into the resonance from the blue side. As the pump is red-tuned, the nonlinear dynamics evolve by first crossing the Turing roll region into the chaotic (modulation instability) comb regions which has a higher transfer of the pump power to the other comb lines. At the chaotic and soliton transition, a soliton emerges and crystallizes within a few round-trips, leading to an almost instantaneous drop in the comb's power. In practice, this rapid drop is followed by cavity shift originating from the thermo-optic absorption effect, i.e. the drop in the intracavity power cools the cavity resulting in a small change in the refractive index, which in turn modifies the resonance frequency, eventually leaving the pump outside of soliton existence range. This response is fast and occurs within the thermal dissipation time, which is on the order of tens to a few hundred nanosecond [188].

All of the previous spectra shown were in a chaotic state. As we transition into the soliton state and monitor the comb power, we observe the signature soliton step, but only with steps of 40 to 200 ns. Several methods have been adopted to mitigate thermal effects [20–24, 189]; here, we evaluate the use of an auxiliary pump and the fast scanning method.

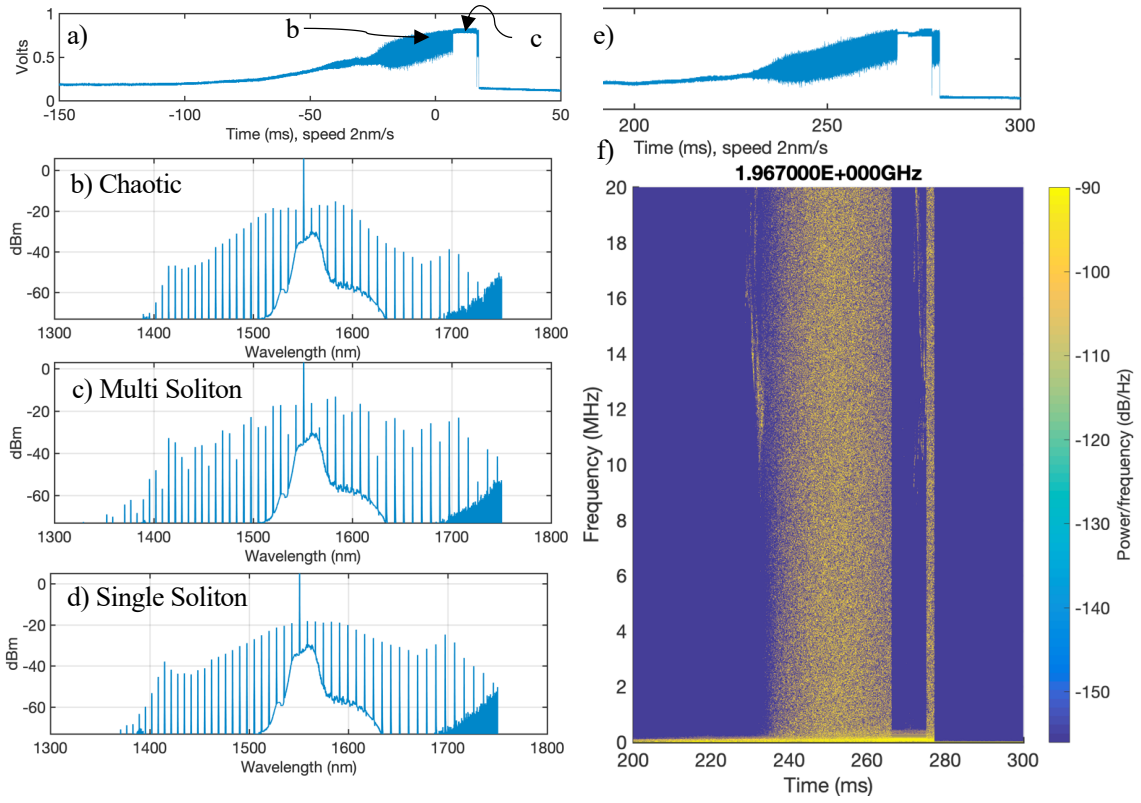

Fig. 7.7. Soliton initiation with an auxiliary pump. a) Comb power with the pump modulated by 1.717 GHz. b) Chaotic comb. c) Multi-soliton state. d) After obtaining a multi-soliton, we access a single soliton state via back-tuning. e) Comb power with the pump modulated by 1.967 GHz. f) Spectrogram of the temporal trace in (e) showing a stage with broadband rf noise followed by a low rf noise multi-soliton comb state. As the detuning is further increased, we enter a second high noise regime arising from the lagging pump generating its own chaotic comb.

7.3.1 Auxiliary pump approach

The basic idea of this approach is to have a second light field that counteracts the power drop and cooling effect that occurs during the emergence of solitons. Instead of using independent laser sources, we run the CW laser through a null-biased intensity modulator drive by an RF frequency on the order of the resonance linewidth (f_{rf} <<

FSR) resulting in two equi-amplitude optical sidebands with the carrier suppressed. As we increase the pump wavelength, the high-wavelength optical sideband reaches the soliton range first, while the other sideband sits on the lower wavelength edge of the resonance. The power drop at the soliton transition pushes the resonance to lower wavelengths, but now the blue-detuned pump couples into the resonance thereby balancing the power drop and counteracting the resonance shift.

In the experiment, we use a THz resonator and drive the intensity modulator using a sinusoidal wave with a frequency between 1.5 and 2.2 GHz. Without modulation, we observe a step of 300 ns. Using the auxiliary laser approach and an RF frequency of 1.717 GHz, we slowly scan the pump and observe a chaotic noisy comb followed by a coherent multi-soliton state (Fig. 7.7a-c). Subsequently, using the backward scan method we switch from a multi-soliton state to a single soliton. Figure 7.7e shows another example of the comb power trace using a frequency of 1.967 GHz, its spectrogram exhibits a low RF noise for the multi-soliton transition, supporting the premise that it is indeed a coherent state. Note that as we further increase the detuning, the soliton is lost and we observe a second chaotic region generated by the lagging pump. As we vary the RF frequency from 1.5 to 2.2 GHz and repeat the scans, we observe long-lived soliton regions across the full RF range, indicating a low sensitivity of the process to the selected RF frequency.

The main advantage of this approach is its relative operational and equipment simplicity. However, in the current implementation, half of the on-chip optical power is reserved to mitigate thermal effects. Additionally, at smaller frequency spacing, the lagging auxiliary pump can generate combs that overlap with the soliton lines and compromises the phase noise performance. Note that this experiment was done using devices from an early fabrication run having a dispersion profile that didn't support broadband combs.

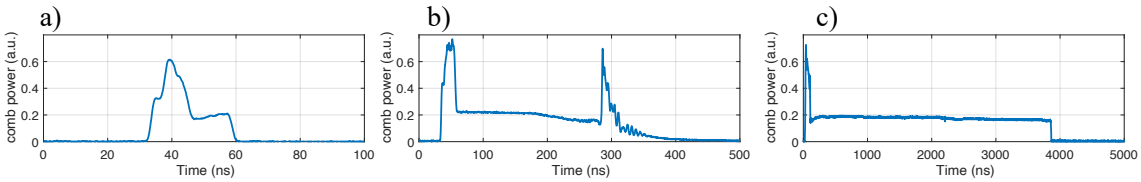

Fig. 7.8. Soliton initiation via fast scanning.

7.3.2 Fast scanning approach

The second approach we have examined was a more common one, where the laser is scanned across the resonance rapidly at rates exceeding the thermal dissipation time. Since the laser scan rate is limited by the piezo's bandwidth, we use a single-sideband suppressed-carrier modulator driven by a voltage-controlled oscillator to perform faster scans. The typical scan rate is a few GHz per 10 to 40 ns. Figure 7.8 shows three examples for a chip with an 80 ns step: in a) we scan by 4 GHz going into the soliton range and exceeding it. In the second case (b), we rapidly scan the laser and immediately stop in the soliton region, which effectively heats the cavity and pushes the resonance to higher wavelengths, thus placing the laser back into the chaotic region. In the third example, we go into the soliton region and then add a second slower ramp – $\sim$ 1 GHz/2.2μs – to move the laser with the resonance and maintain the soliton. These observations are in line with those reported in [189]. For the octave-spanning combs devices fabricated by Chalmers, we notice smaller thermal effects and - typically - a single ramp is sufficient to generate and keep a soliton state. The octave-spanning low noise soliton spectrum is shown in Fig. 7.9.

7.4 Optical Division of the Repetition Rate

At this point, we have successfully generated octave-spanning solitons, but the story doesn't simply end here. The main idea of introducing a frequency comb is to coherently divide the clock laser frequency down to a microwave frequency acces-

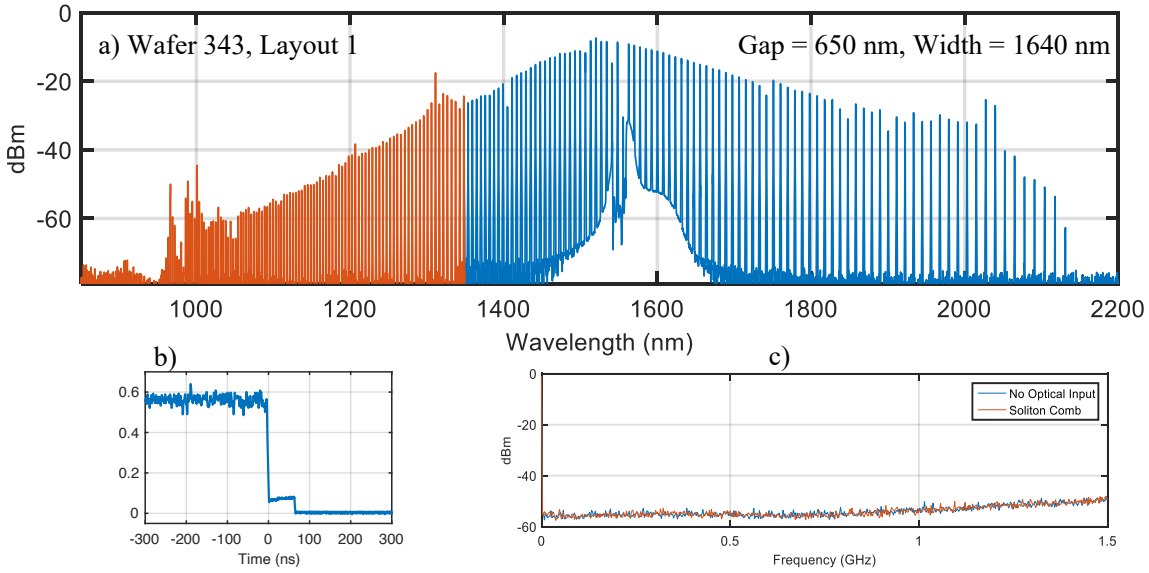

Fig. 7.9. Octave-spanning soliton. An example of 65 ns step is shown in b, and the soliton's RF spectrum is shown in c.

sible to electronic counters and processors. Thus far, we can only divide it down to $\sim$ 900 GHz–still electronically inaccessible. Of course, the most straightforward way would be to general low repetition rate octave-spanning Kerr combs, but mode-interaction, threshold power, and dispersion engineering constraints - at this point - do not permit that. Instead, we can divide the soliton's repetition itself optically; two methods are discussed below.

7.4.1 Conventional dual-comb division

The first method is a rather simple and straightforward method to understand; use a secondary ring with a smaller FSR, e.g. $\sim$ 20 GHz, to lock to and divide the repetition rate of the main comb. This is the method adopted by NIST in their recent papers where they use a SiO_2 whispering gallery mode resonator in conjunction with a Si_3N_4 THz ring [159, 184, 189]. The scheme is illustrated in Fig. 7.10 where we assume that a CW laser is used as a common pump constituting the first locking

point. If the $\sim$ 20 GHz comb is broad enough, the secondary comb overlaps with one or multiple of the main comb sidebands, and this will be our second locking point. The frequency instability of the secondary comb repetition rate, which now serves as the clock output, can be written as

$$\Delta f_{clk} = \Delta f_{rep_2} = \frac{1}{\bar{M}_2}\Delta f_{overlap} + \frac{f_{rep_2}}{f_{rep}}\Delta f_{rep} \tag{7.5}$$

where $\Delta f_{overlap}$ is the frequency instability of the beat note between the overlapping comb lines $\nu_o + \bar{M}_1 f_{rep}$ and $\nu_o + \bar{M}_2 f_{rep_2}$, where $\bar{M}$ is an integer, and Δf_{clk} is the frequency instability of the output RF clock. From this expression, we see that Δf_{rep_2} is a divided version of Δf_{rep} which can be either locked - as we will discuss next - or free-running. To have a successful division, the instabilities from the PLL ($\Delta f_{overlap}$) must be smaller than that of Δf_{rep}, so - ideally - $\bar{M}_2$ has to be as large as possible. For a 20 GHz comb locked to the first sideband of a 1 THz primary comb, $\bar{M}_2$ is 50 or integer multiple of f_{rep}/f_{rep_2} in general.

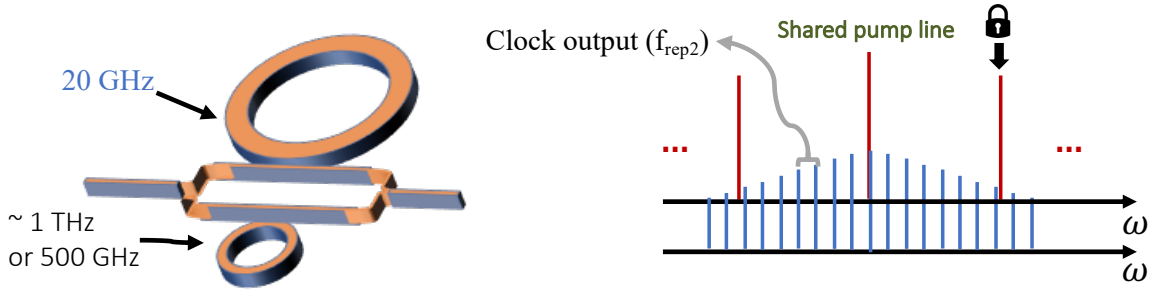

Fig. 7.10. Conventional dual-comb division.

7.4.2 Vernier dual-comb division

Instead of following the previous approach, we propose an alternative scheme that uses two rings with *large* repetition rates. The secondary comb now has a repetition rate of $f_{rep_2} = f_{rep} + \delta f$. The rings share the same CW pump, and due to the Vernier effect, the combs' sidebands progressively walk-off until they overlap back again M_2

modes away from the pump. At this point, the overlap beat note ($f_{overlap}$) is detected and locked. The divided clock output is produced by measuring the beat frequency between the first sideband pair. Adding a linear perturbation and solving for the instability term, we can write the frequency instability as

$$\Delta f_{clk} = \frac{1}{M_2}\Delta f_{overlap} + \frac{\delta f}{f_{rep}}\Delta f_{rep} \tag{7.6}$$

The expression is almost identical to eq. 7.5. We see that f_{rep} is divided down to δf, and that we also prefer a large M_2, which in general is integer multiple of $f_{rep}/\delta f$. Note that the secondary comb doesn't have to be octave-spanning but should be broad enough to overlap again with the primary comb. Using a 1 THz ring pumped at 1550 nm and a δf of 20 GHz, the two combs overlap at 1022 nm, 1232 nm, and 2090 nm. Ideally, we'd like to use the farthest overlap point, but practical considerations such as comb line powers and choice of photodetectors will eventually set the choice.

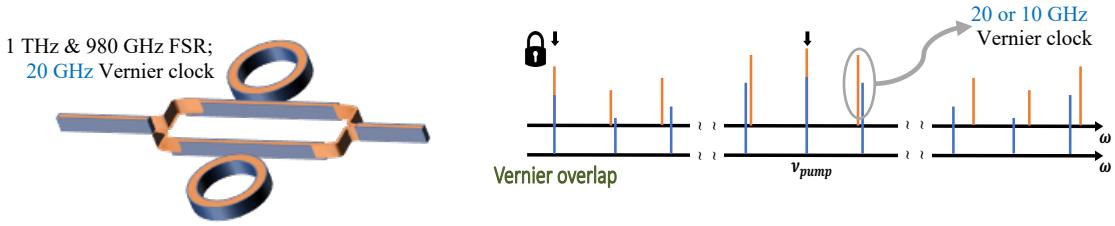

Fig. 7.11. Vernier dual-comb division.

Compared to the previous approach, this method has several advantages. Assuming that the two combs are to be homogeneously integrated, the intrinsic quality factor for both should be similar. Given that the parametric threshold power is proportional to the Radius/Q^2, the 20 GHz ring has threshold power 50 times larger than that of a THz ring. Furthermore, the 20 GHz ring consumes an area 2500 times larger as well, so using the same space we can fit hundreds of the THz combs compared to a few of the prior. This is important as we need to use the wafer's real-estate efficiently in

order to have sufficient sweeps of design parameters that overcome fabrication uncertainties. Additionally, not only do we save on power consumption and footprint but we also gain in terms of the power per comb line. For an overcoupled device, which is preferred to enhance the conversion efficiency, the pump to comb conversion efficiency is linearly proportional to the FSR [190]. Additionally, this total power is divided between a smaller number of lines for a THz device. Thus, the power per comb line for a THz comb can be more than 30 dB higher than a 20 GHz single soliton, which greatly benefits the signal-to-noise ratio (SNR) of the generated beat notes. This is key to obtaining a successful division and, generally, the power per comb line is an important and limiting factor for deploying Kerr combs in real-world applications as we've seen in chapter 6.

The first two octaves in Fig. 7.6 are a Vernier pair, and at least three other options that are not octave-spanning but are broad enough have been obtained. We are currently in pursuit of a Vernier division demonstration. Additionally, we are also pursuing the conventional division approach using a ∼900 GHz ring and a ∼20 GHz ring with Chalmers. The main novelty added in the later approach is that both rings will be based on integrated Si_3N_4 rings and fabricated using the same wafer. We note that, independently, another group has recently demonstrated a proof-of-principle Vernier division experiment using relatively narrow-band solitons with a repetition rate of 216 GHz [191].

7.5 Integrated Microring Heaters

The Vernier ring pair will have different resonance frequencies due to the different radius, therefore, pumping the rings using the same CW laser isn't viable. We rely on microring heater to shift the resonance of one ring to overlap with its pair. The targeted resonance shift range is a full FSR. The first designs were based on a 300 nm and 10 μm wide gold heaters on top of a 30 nm Titanium film, which had offered a maximum of 435 GHz tuning short-term tuning with a 1 THz ring before damage to

the heaters was observed. The origin of the damage was likely electromigration, indicating a material limited performance. To achieve the desired goal, we have changed the heater material to a 350 nm Platinum film on top of a thin 20 nm Titanium adhesion film. Figure 7.12 shows the electrical power required to tune the resonance. With a 10 μm wide heater, a maximum short-term tuning of 964 GHz was achieved using a THz ring at a cost of $\sim$420 mW of electrical power consumption. Notice as well that the platinum resistance increases proportionally to the tuning, which can be explained by Platinum's temperature dependent resistivity [192]. Assuming the heater was at room temperature, the change in resistance suggests that the temperature of the heater at maximum tuning is 314°C, but further investigations are needed to verify this conclusion and understand if the Titanium layer modifies the behaviour. Long-term reliability tests and cyclic tuning tests have been conducted, and more details can be found in my colleague Cong Wang's thesis.

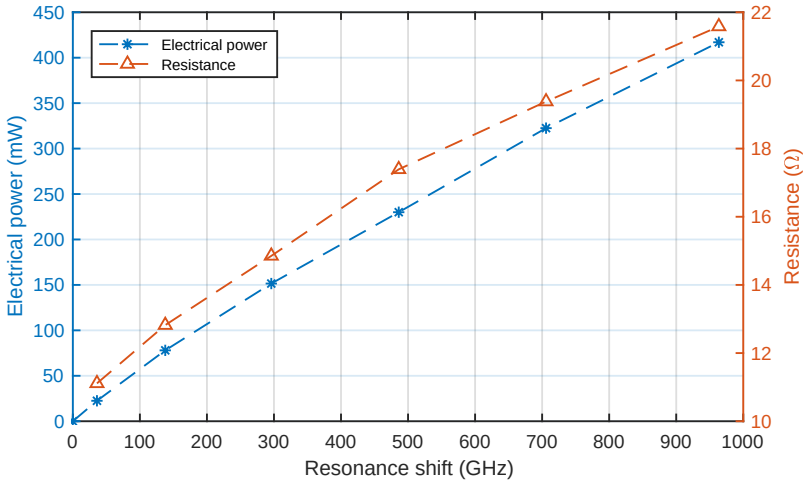

Fig. 7.12. Heater characterization.

Once the two rings are aligned, they can be moved in tandem to tune the CEO frequency. As the CEO frequency can be anywhere from $\pm$FSR/2, it is necessary to place it at an electronically detectable frequency and preferred to be at the lowest frequency possible. The full FSR tuning only gives ca. 100 GHz increase in CEO

frequency; a simple way to explain the discrepancy is to note that as we heat and tune the resonance, the Si_3N_4 temperature-dependent refractive index leads to a change in repetition rate that counteracts the resonance shift. For more in-depth analysis we refer the reader to [193]. Reliably achieving a small CEO frequency is one of the grand challenges in this project.

Note that the architecture shown in Fig. 7.11 is, for now, just a pictorial representation. As a first stage, we split the pump laser using a fiber coupler into two paths, each containing its own *separate* optical amplifier and chip mounting stage. In principle, a multi-mode interferometer can be fabricated to controllably split the laser on-chip and pump the Vernier ring pairs as depicted in Fig. 7.11 [194]. The substantial heating that we may apply to align the resonances or to tune the CEO frequency might introduce some thermal cross-talk between the rings. Nevertheless, previous examples of heating closely-placed coupled resonators [195–197] suggest that while thermal cross talk might complicate alignment, it should not be detrimental to the setup, especially that the rings in our case can be placed sufficiently far from each other. As a risk mitigation, the rings can be thermally insulated by digging trenches underneath the microring region, which also adds a second benefit by significantly improving the thermal tuning efficiency thereby reducing the electrical consumption [198].

7.6 Stabilization of the Main Comb

The final piece in this chapter, and the most important one, is stabilizing the comb to the clock laser and obtaining a phase-coherent divided RF output. The common scenario is to detect a heterodyne beat between one of the the comb lines and the clock laser and to then lock this beat. Along with the previously discussed f-2f CEO stabilization, this two-point locking scheme transfers the stability of the clock laser to the repetition rate of the main comb. However, since the comb's bandwidth in our case doesn't extend to 871 nm, we have to bridge the gap with aid of a frequency

conversion stage. In this section, we will discuss three options for phase-2 of the project and compare their 'practical' applicability.

7.6.1 Direct second-harmonic generation (SHG)

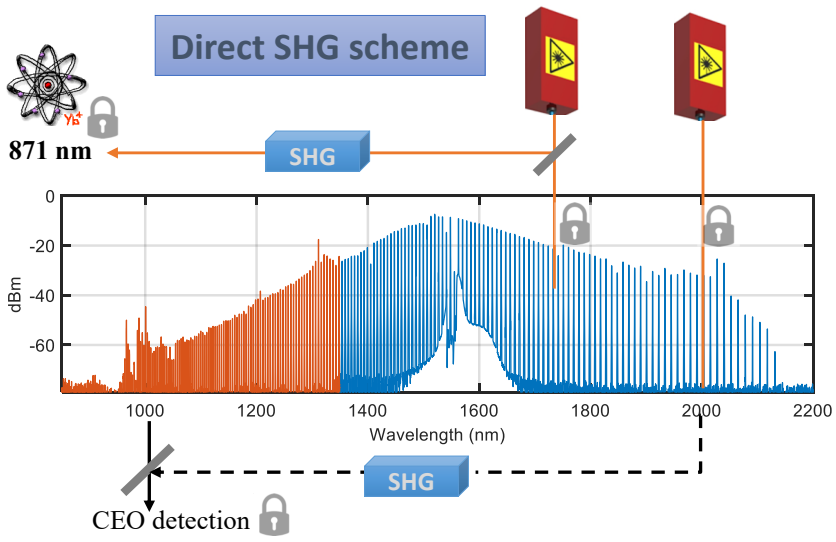

Fig. 7.13. Direct second-harmonic generation scheme.

The most straightforward and direct approach would be to frequency double a comb line at 1742 nm and lock it to the clock laser, as well as frequency doubling a comb line around 2 μm for CEO frequency locking. However, the low comb line powers (1 - 10 μW) leave insufficient power after the nonlinear SHG process, even if state-of-the-art waveguides are used (e.g. 1 μW input into a waveguide with 1000%/W conversion efficiency gives 10 pW at the second-harmonic). The only workaround is to either amplify the light externally or to use a 'helper' laser that locks to each comb-line and boosts the power level as shown in Fig. 7.13. This adds an overhead of two additional lasers that have to be integrated as well as two photodetectors and electronics associated with the PLL. Clearly, this doesn't bode well with the final

integration mission and is not an elegant approach. The instability of the comb, in this case, can be written as

$$\Delta f_{rep} = \frac{f_{rep}}{\nu_{clk}}\left(2\Delta f_{ceo} + \Delta f_{comb_{871}} + \Delta\nu_{clk}\right) \tag{7.7}$$

where ν_{clk} is the clock laser frequency and $\Delta\nu_{clk}$ is its frequency instability, Δf_{ceo} is the frequency instability of the CEO RF beat note, and $\Delta f_{comb_{871}}$ is the instability of the locked beat note generated by heterodyning a frequency-doubled comb line with the clock laser. This expression is identical to the usual OFC division except for the factor of 2 preceding Δf_{ceo} that arises from the SHG shortcut.

7.6.2 Sum frequency generation (SFG)

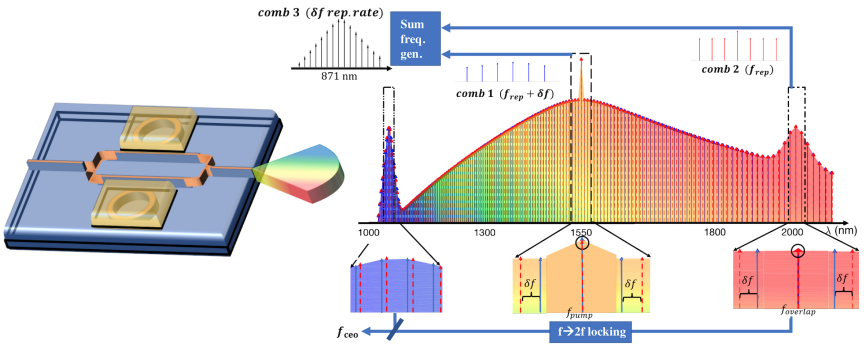

Fig. 7.14. Sum frequency generation scheme.

As mentioned previously, obtaining a close to zero CEO frequency is eo ipso an arduous challenge. Adding insult to injury, we also need to ensure that a comb line beats with the clock laser at a detectable frequency! To alleviate part of this direful situation, we propose to mix the two combs in an SFG waveguide. As illustrated in Fig. 7.14, mixing a section of the main comb at the C-band with a section of the Vernier comb centered around 2μm generates a cluster of narrow-band combs with a frequency spacing of δf centered around 871 nm, guaranteeing a beat note less than

or equal to $\delta f/2$. Following the linear perturbation approach and assuming that the CEO is locked via the f-2f method, we derive the instability as

$$\Delta f_{rep} = \frac{f_{rep}}{\nu_{clk}}\left(2\Delta f_{ceo} + \Delta f_{comb_{871}} + \frac{N_2}{M_2}\Delta f_{overlap} + \Delta\nu_{clk}\right) \tag{7.8}$$

where a line from the main comb is mixed with a line from the auxiliary comb ($\nu_o - N_2 f_{rep2}$) to beat with the clock laser. Here ν_o is the pump frequency and M_2 is the mode-spacing between the pump and the combs' overlap point as discussed in section 7.4. Notice that the instability of locking the two combs ($\Delta f_{overlap}$) unsurprisingly factors in the expression of the repetition rate instability. While this approach elegantly adds a second use case for the auxiliary comb which addresses the challenge of locking to the clock laser, it requires a broad phase matching design for the nonlinear waveguide, which comes at the expense of conversion efficiency, or a phase-matching tuning ability. Equally important, this method falls prey to the low-power challenge that hinders the f-2f process. It is a clever approach if one allows the use of broadband amplifiers and/or helper lasers, but it doesn't meet the program's goals.

7.6.3 Difference frequency generation (DFG)

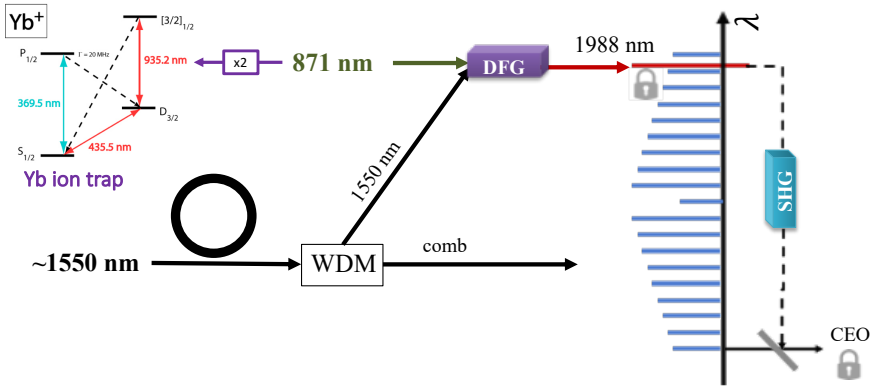

Fig. 7.15. Difference frequency generation scheme.

Driven by practical power concerns, we ask ourselves what is the best approach to efficiently use the optical power at hand? A pump line distinctly ∼20 dB higher than neighboring comb lines – surreptitiously filtered out in previously shown spectra – stands out! The low conversion efficiency of the Kerr comb generation process leaves more than 95% of the pump power untouched. Instead of leaving it to waste, by mixing the pump at ∼1550 nm with the 871 nm clock laser in a DFG process, we generate light at 1988 nm. Even with a moderate conversion efficiency of 50%/W, mixing 200 mW of the pump with 10 mW of the clock laser generates 1 mW at 1988 nm. By locking this DFG line to the neighboring comb line, we obtain our first locking point. Subsequently, we propose to use this high-power, felicitously chosen DFG output frequency for the f-2f process and lock it to a comb line at 1 μm, see Fig. 7.15 for an illustration. We derive the instability of this approach as

$$\Delta f_{rep} = \frac{f_{rep}}{\nu_{clk}}\left(3\Delta f_{DFG_{2\mu m}} - 2\Delta f_{2DFG_{1\mu m}} + \Delta\nu_{clk}\right) \tag{7.9}$$

where $\Delta f_{DFG_{2\mu m}}$ is the instability of locking a comb line at the high wavelength to the DFG line, and $\Delta f_{2DFG_{1\mu m}}$ is the instability of locking a comb line at the low wavelength to the frequency-doubled DFG line. While it may seem counter-intuitive at first as mixing a comb line with the clock laser may seem to obscure the stability of the clock laser, the derived equation proves otherwise. This is *not* a fundamental problem; even in the conventional case, when a comb line directly beats with the clock laser to generate a locking beat note, the photodetection process acts essentially as a nonlinear mixing process that generates an electromagnetic field at microwave frequencies. The stability of this microwave frequency is obscured by that of the comb as well, but this doesn't prevent the transfer of the clocks laser stability once all PLLs are engaged. This scheme hits two birds with one stone: First, it bridges the wavelength gap between the comb and the clock laser; Second, it allows f-2f locking without the need of external helper lasers, and does all without adding additional nonlinear stages. Since the power of the f-2f beat note is proportional to the the power of the heterodyned comb lines at 1 μm, it is then proportional to the squared of the 2μm that undergoes the frequency-doubling nonlinear stage. The 100 times

increase in power at 2 μm enabled by the DFG scheme gives a 10,000 fold increase in the f-2f RF beat note, which is typically a more difficult lock-point due to low SNRs. Note that it is also possible to lock the DFG line to a comb line of the auxiliary comb, which increases the chance of obtaining detectable beat notes for all lock points.

Finally, it is instructive to look at the final clock output expression with Vernier division written in terms of *fractional* instability $\bar{\Delta}f = \Delta f/f$. Substituting eq. 7.9 in eq. 7.6, we obtain

$$\bar{\Delta}f_{clk} = \frac{\bar{\Delta}f_{overlap}}{M_2} \cdot \frac{f_{overlap}}{\delta f} + \left(3\bar{\Delta}f_{DFG_{2\mu m}} \frac{f_{DFG_{2\mu m}}}{\nu_{clk}} - 2\bar{\Delta}f_{2DFG_{1\mu m}} \frac{f_{2DFG_{1\mu m}}}{\nu_{clk}} + \bar{\Delta}\nu_{clk}\right) \tag{7.10}$$

This equation gives insight into how tightly do we need to lock the combs and what terms are likely to be dominant. The first term on the right-hand-side ($\bar{\Delta}f_{overlap}$) is the fractional instability of locking the two Vernier combs at the overlap point. The two other fractional instabilities ($\bar{\Delta}f_{DFG_{2\mu m}}$ and $\bar{\Delta}f_{2DFG_{1\mu m}}$) arise from the two-point locking in the DFG scheme as discussed earlier. The program goal for the RF clock output is to follow that of the clock laser, i.e. $\bar{\Delta}f_{clk} = \bar{\Delta}\nu_{clk} = 1 \times 10^{-14}/\sqrt{\tau_{av}}$. To achieve that goal, all other instability terms arising from the PLLs must be smaller than that of $\bar{\Delta}\nu_{clk}$. We are aided on this front by the large division factors; if we assume that $f_{DFG_{2\mu m}} = f_{DFG_{2\mu m}} = 1$ GHz and given $\nu_{clk} \approx 344$ THz, to keep those locks instabilities one order of magnitude lower than the clock laser we require $\bar{\Delta}f_{2DFG_{1\mu m}}$ and $\bar{\Delta}f_{DFG_{2\mu m}}$ to be equal to or less than $\sim 10^{-10}/\sqrt{\tau_{av}}$. This not too difficult to achieve as good quartz reference oscillators can reach a stability $10^{-12}/\sqrt{\tau_{av}}$. As M_2 in the first right-hand term is small (50), the comb overlap lock point will dominate unless $f_{overlap}$ is sufficiently small. Assuming that $f_{overlap} = 10$ MHz and given $\delta f = 20$ GHz, to keep this term one order of magnitude lower than the clock laser we require $\bar{\Delta}f_{overlap}$ to be equal to or less than $\sim 10^{-10}/\sqrt{\tau_{av}}$. Note that if $f_{overlap} = 1$ GHz, the requirement on the lock instability becomes 100 times smaller. An alternative approach to overcome the limitation of the two-comb lock point is to have the two combs independently fully-stabilized and then generate an RF output by measuring the beat between the first sidebands.

7.7 Conclusion and Outlook

In this chapter, we have shown that through dispersion engineering, Kerr combs can generate octave-spanning combs in a single stage starting with just a CW pump. Using fast scanning, we overcome thermal effects and obtain coherent Mode-locked solitons. So far, these octave-spanning Kerr combs have electronically undetectable repetition rates. We propose a novel Vernier dual-comb division scheme that provides a coherently divided RF output. Compared to the conventional dual-comb division approach, this scheme is advantageous in terms of system footprint, power consumption, and higher powers per comb line. Finally, we have discussed three schemes to lock to the clock laser and proposed a novel DFG approach that alleviates the need for external helper lasers or amplifiers. While not within the scope of the current discussion, thermo-refractive noise is known to affect the comb's repetition rate through fluctuations in the refractive index that couples to dispersion. It would be interesting to study how large thermal tuning modifies the situation by affecting the dispersive wave power and the soliton recoil.

The integration and mass-production of fully-stabilized combs will heavily impact geodesy, LIDAR, timing, and synchronization applications. By equipping unmanned aerial vehicles (UAV) with such precision tools, we envision a fleet of UAVs that provide timing and positioning services in GPS denied environments, and UAVs that can measure sea-level rise or map the elevation of vast lands through the aid of LIDAR and height or gravitational potential measurements. All other OFC applications such as spectroscopy, microwave signal processing, and radars will benefit from this improved stability and ultra-low jitter performance.

To be a cost-effective tool for real-world applications, the process yield has to be improved. As process-development continues, we anticipate improved control on dispersion, film quality, and heater efficiency; however, ensuring that all locking points are at a small and detectable frequency is hindered by inevitable statistical variations in the fabrication process. To get a feel of the process sensitivity, table 7.1 shows

Table 7.1.
Fabrication uncertainties and parameter sensitivity for a 740 nm × 1.6 μm Si_3N_4 ring with 25 μm radius and oxide cladding using Chalmers refractive index measurements. Simulated by Cong Wang.

	Thickness	Width	Temperature
Pump resonance	-100 GHz / 5 nm	-54 GHz/ 10 nm	-2.6 GHz/°C
Repetition rate	-60 MHz / 5 nm	40 MHz / 10 nm	-14 MHz/°C
Carrier-envelope offset	92 GHz / 5 nm	67 GHz / 10 nm	400 MHz/°C
Dispersive wave (at 2 μm)	-6 THz / 5 nm	1 THz / 10 nm	-16 GHz/°C
Dispersive wave (at 1 μm)	7 THz / 5 nm	-4.7 THz / 10 nm	30 GHz/°C

simulations, performed by my colleague Cong Wang, of the sensitivity of a THz ring parameters to minute changes in thickness or width. The simulations show a ±92 GHz change in CEO frequency for a mere ±5 nm variation in film thickness! Note that this simulation assumes fixed, repeatable, and known refractive index and doesn't take into account wafer to wafer variations in the refractive index. The only way to overcome such uncertainties is to fabricate a large set of rings with few nanometer variations in radius and ring-width, which can increase the probability of obtaining a close-to-zero CEO frequency. However, the likelihood of having *both* the CEO frequency and the lock to the clock laser being zero remains a dreadful situation, but integrated heaters might improve our chances.

The natural way to overcome the sparsity in the comb spectral sampling is to shift to smaller FSRs: 100 GHz for example. Recent results in high-quality SiN rings indicate the threshold optical power shouldn't be a problem. However, as the mode spacing decreases, the likelihood of mode-interaction that destabilizes the soliton formation increases, especially if optimizing the dispersion requires multi-mode waveguides. Recent techniques in dispersion engineering showed that instead of having a fixed ring-width, designing multiple sections with different widths can be used

to add a mode-filtering section, provides additional control on the dispersion profile, and - in some cases - improves the quality factor [199]. I expect such techniques to enable 100 GHz octave-spanning solitons in the near future. The 100 GHz pulse train can be detected through the optical division methods we've discussed earlier, or through direct detection using uni-traveling carrier photodiodes [200]. In principle, pumping at shorter wavelengths should be possible and will eliminate the need for nonlinear frequency conversion stages to lock to the clock laser.

8. SUMMARY AND OUTLOOK

Photonic integrated circuits (PIC) enable massive fabrication of low-loss elements that hold the potential to change the landscape of photonics-based hardware and its market penetration. This thesis is a set of projects oriented around developing integrable methods and apparatuses to utilize photonics in quantum and radio frequency processing applications.

The first three chapters focused on high-dimensional quantum states. In chapter 2, we design a high-dimensional 16×16 SUM gate using a qudit pair encoded in the time and frequency DoF of a single photon. Encoding in a single-photon evades the probabilistic gate operation using two-photons. Using this SUM gate, we generate a four-party two-photon GHZ state with a Hilbert dimension of more than one million dimensions– equivalent to that of 20 qubits. Subsequently, in chapter 3, we utilize these concepts to demonstrate the first qutrit-based phase implementation of the quantum phase estimation algorithm. Finally, in chapter 4, we run a BFC through a tunable frequency-domain quantum random walk circuit implemented using an electro-optic phase modulator. We observe and control the formation of enhanced energy ballistic transport and bound-states and show a link between the energy transfer and the high-dimensional entanglement of the input BFC state.

Our interest in high-dimensional encoding is motivated by the relative ease of generating such states using integrated passive microrings. However, regardless of the platform, it is interesting to see if qudits have characteristics or advantages that are not attainable using qubits. These may be advantages of technical nature, e.g. reducing the number of gates or the depth of circuit implementing a quantum algorithm [201], or physical phenomena that can only be simulated with high-dimensional states [131].

The past decade saw a surging interest in the physical implementation and commercialization of quantum optics and quantum computing in general, driven by both private and government funding. Several competing platforms exist, among those are superconducting systems, trapped ions, spin-based qubits, quantum optics, and topological systems. Silicon photonics has certainly propelled the interest in photonic qubits, but it will be interesting to see how the field develops over the next ten years, particularly on the hardware front. In a survey among 22 leading quantum researchers, none chose optics as a first choice platform, and only three ranked it as a second choice option [202]. Nevertheless, among quantum start-ups, photonics-based start-ups surprisingly raised the largest share of disclosed private investment, securing a 36% share ($334 million) of the total investments over the 2010 - 2020 period [203]. Although this share is largely dominated by a single company, the bet on these mostly PIC-based platforms enunciates the disruptive impact of integrated solutions on the market landscape of photonics-based applications. Apart from quantum computing, optics are a leading platform for secure quantum communications, and quantum interconnects [204].

The second half of this thesis focuses on the classical applications of optical frequency combs, particularly electro-optic and Kerr combs. In chapter 5, we develop an integrable subsampling setup that disambiguates over 10 Nyquist zones with the potential to tune the bandwidths to as high as $\sim$100 GHz. We derive a detailed theoretical analysis of the link-metrics that will guide future designs. Next, in chapter 6, we use Kerr combs generated from an integrated Si_3N_4 microring to mitigate Brillouin scattering in long-haul analog links and demonstrate a 20 fold increase in the backscattering-power threshold. We perform the first detailed comparison of the RF link-metrics using Kerr combs and compare the performance using dark and bright solitons. Finally, in chapter 7, we propose a novel Vernier division scheme to enable the integration of optical-atomic clocks based on THz combs. We report on our progress on this front where we generate octave-spanning dissipative Kerr solitons as well as identify candidate Vernier rings that are integrated and fabricated in a single

wafer. To address challenges imposed by the low comb-line powers, we propose a scheme that utilizes the clock laser for the nonlinear frequency mixing operations, relieving the need for external lasers or amplifiers.

A great level of detail was dedicated to characterizing the rf metrics of our photonic-based RF processors and links. While photonics have enabled a plethora of unique RF processing and generation functionalities [5, 149], to be useful in real-world applications, said systems must achieve link metrics (noise figure, gain, and SFDR) equivalent to or better than their electronic counterparts. To achieve this goal, two main ingredients are needed: low-loss ultra-low V_π modulators, and high-power handling photodetectors. As for integrated OFC generators, both resonant and non-resonant EO combs as well as Kerr combs are the leading options. As we have seen in ch. 6, low conversion efficiency and low powers per comb-line are one of the main challenges for Kerr combs. The conversion efficiency is set by the nonlinear physics and is not a technical shortcoming, but highly-overcoupled designs or coupled cavities can improve the conversion efficiency [205]. Nevertheless, it is truly amazing how the field transformed within 10 years from barely making noisy incoherent combs to demonstrating octave-spanning solitons as well as integrated and packaged Kerr combs with turn-key operation [159, 206]. As the understanding of the underlying physics is reaching maturity, the focus has shifted heavily towards applications and exploring different materials as well as different frequency points of operation. A relatively less explored comb source is based on resonators with $\chi^{(2)}$ nonlinearity, and it has been shown that such combs, as well as semiconductor ring lasers, can generate coherent combs that share similar properties to that of dissipative Kerr solitons [207, 208]. Kerr combs have been demonstrated in waveguides made of a wide range of materials, of which silicon nitride is already made available by commercial foundries. In materials with both $\chi^{(2)}$ and $\chi^{(3)}$ nonlinearities, it will be interesting to observe how does the interplay between the two nonlinearities changes the dynamics of comb generation [209–211] or enables biphoton state manipulation [212]. The

transfer of such technologies to commercially accessible foundries ushers a new era of photonic design and implementation.

REFERENCES

REFERENCES

[1] J. L. Hall, "Nobel lecture: Defining and measuring optical frequencies," *Reviews of Modern Physics*, vol. 78, no. 4, p. 1279, 2006.

[2] T. W. Hänsch, "Nobel lecture: passion for precision," *Reviews of Modern Physics*, vol. 78, no. 4, p. 1297, 2006.

[3] D. J. Jones, S. A. Diddams, J. K. Ranka, A. Stentz, R. S. Windeler, J. L. Hall, and S. T. Cundiff, "Carrier-envelope phase control of femtosecond mode-locked lasers and direct optical frequency synthesis," *Science*, vol. 288, no. 5466, pp. 635–639, 2000.

[4] N. R. Newbury, "Searching for applications with a fine-tooth comb," *Nature photonics*, vol. 5, no. 4, p. 186, 2011.

[5] M. S. Alshaykh, J. D. McKinney, and A. M. Weiner, "Radio-frequency signal processing using optical frequency combs," *IEEE Photonics Technology Letters*, 2019.

[6] A. J. Metcalf, V. Torres-Company, D. E. Leaird, and A. M. Weiner, "High-power broadly tunable electrooptic frequency comb generator," *IEEE Journal of Selected Topics in Quantum Electronics*, vol. 19, no. 6, pp. 231–236, 2013.

[7] V. Torres-Company and A. M. Weiner, "Optical frequency comb technology for ultra-broadband radio-frequency photonics," *Laser & Photonics Reviews*, vol. 8, no. 3, pp. 368–393, 2014.

[8] C. Wang, M. Zhang, X. Chen, M. Bertrand, A. Shams-Ansari, S. Chandrasekhar, P. Winzer, and M. Lončar, "Integrated lithium niobate electro-optic modulators operating at CMOS-compatible voltages," *Nature*, vol. 562, no. 7725, p. 101, 2018.

[9] N. Andriolli, T. Cassese, M. Chiesa, C. De Dios, and G. Contestabile, "Photonic integrated fully tunable comb generator cascading optical modulators," *Journal of Lightwave Technology*, vol. 36, no. 23, pp. 5685–5689, 2018.

[10] M. Kourogi, K. Nakagawa, and M. Ohtsu, "Wide-span optical frequency comb generator for accurate optical frequency difference measurement," *IEEE Journal of Quantum Electronics*, vol. 29, no. 10, pp. 2693–2701, 1993.

[11] M. Kourogi, B. Widiyatomoko, Y. Takeuchi, and M. Ohtsu, "Limit of optical-frequency comb generation due to material dispersion," *IEEE journal of quantum electronics*, vol. 31, no. 12, pp. 2120–2126, 1995.

[12] Z. Jiang, D. E. Leaird, C.-B. Huang, H. Miao, M. Kourogi, K. Imai, and A. M. Weiner, "Spectral line-by-line pulse shaping on an optical frequency comb generator," *IEEE Journal of Quantum Electronics*, vol. 43, no. 12, pp. 1163–1174, 2007.

[13] M. Zhang, B. Buscaino, C. Wang, A. Shams-Ansari, C. Reimer, R. Zhu, J. M. Kahn, and M. Lončar, "Broadband electro-optic frequency comb generation in a lithium niobate microring resonator," *Nature*, vol. 568, no. 7752, p. 373, 2019.

[14] S. Coen, H. G. Randle, T. Sylvestre, and M. Erkintalo, "Modeling of octave-spanning kerr frequency combs using a generalized mean-field lugiato–lefever model," *Optics letters*, vol. 38, no. 1, pp. 37–39, 2013.

[15] Y. K. Chembo and C. R. Menyuk, "Spatiotemporal lugiato-lefever formalism for kerr-comb generation in whispering-gallery-mode resonators," *Physical Review A*, vol. 87, no. 5, p. 053852, 2013.

[16] C. Godey, I. V. Balakireva, A. Coillet, and Y. K. Chembo, "Stability analysis of the spatiotemporal lugiato-lefever model for kerr optical frequency combs in the anomalous and normal dispersion regimes," *Physical Review A*, vol. 89, no. 6, p. 063814, 2014.

[17] T. Herr, V. Brasch, J. D. Jost, C. Y. Wang, N. M. Kondratiev, M. L. Gorodetsky, and T. J. Kippenberg, "Temporal solitons in optical microresonators," *Nature Photonics*, vol. 8, no. 2, p. 145, 2014.

[18] H. Guo, M. Karpov, E. Lucas, A. Kordts, M. H. Pfeiffer, V. Brasch, G. Lihachev, V. E. Lobanov, M. L. Gorodetsky, and T. J. Kippenberg, "Universal dynamics and deterministic switching of dissipative kerr solitons in optical microresonators," *Nature Physics*, vol. 13, no. 1, p. 94, 2017.

[19] T. C. Briles, J. R. Stone, T. E. Drake, D. T. Spencer, C. Fredrick, Q. Li, D. Westly, B. Ilic, K. Srinivasan, S. A. Diddams *et al.*, "Interlocking kerr-microresonator frequency combs for microwave to optical synthesis," *Optics letters*, vol. 43, no. 12, pp. 2933–2936, 2018.

[20] V. Brasch, M. Geiselmann, M. H. Pfeiffer, and T. J. Kippenberg, "Bringing short-lived dissipative kerr soliton states in microresonators into a steady state," *Optics express*, vol. 24, no. 25, pp. 29 312–29 320, 2016.

[21] D. C. Cole, J. R. Stone, M. Erkintalo, K. Y. Yang, X. Yi, K. J. Vahala, and S. B. Papp, "Kerr-microresonator solitons from a chirped background," *Optica*, vol. 5, no. 10, pp. 1304–1310, 2018.

[22] H. Zhou, Y. Geng, W. Cui, S.-W. Huang, Q. Zhou, K. Qiu, and C. W. Wong, "Soliton bursts and deterministic dissipative kerr soliton generation in auxiliary-assisted microcavities," *Light: Science & Applications*, vol. 8, no. 1, p. 50, 2019.

[23] T. Wildi, V. Brasch, J. Liu, T. J. Kippenberg, and T. Herr, "Thermally stable access to microresonator solitons via slow pump modulation," *Optics letters*, vol. 44, no. 18, pp. 4447–4450, 2019.

[24] G. Moille, X. Lu, A. Rao, Q. Li, D. A. Westly, L. Ranzani, S. B. Papp, M. Soltani, and K. Srinivasan, "Kerr-microresonator soliton frequency combs at cryogenic temperatures," *Physical Review Applied*, vol. 12, no. 3, p. 034057, 2019.

[25] J. Liu, E. Lucas, A. S. Raja, J. He, J. Riemensberger, R. N. Wang, M. Karpov, H. Guo, R. Bouchand, and T. J. Kippenberg, "Photonic microwave generation in the x-and k-band using integrated soliton microcombs," *Nature Photonics*, pp. 1–6, 2020.

[26] Z. Ye, K. Twayana, P. A. Andrekson, and V. Torres-Company, "High-Q Si_3N_4 microresonators based on a subtractive processing for kerr nonlinear optics," *Opt. Express*, vol. 27, no. 24, pp. 35 719–35 727, Nov 2019.

[27] T. J. Kippenberg, A. L. Gaeta, M. Lipson, and M. L. Gorodetsky, "Dissipative Kerr solitons in optical microresonators," *Science*, vol. 361, no. 6402, p. eaan8083, 2018.

[28] Y. He, Q.-F. Yang, J. Ling, R. Luo, H. Liang, M. Li, B. Shen, H. Wang, K. Vahala, and Q. Lin, "Self-starting bi-chromatic linbo 3 soliton microcomb," *Optica*, vol. 6, no. 9, pp. 1138–1144, 2019.

[29] Y. He, J. Ling, M. Li, and Q. Lin, "Perfect soliton crystals on demand," *Laser & Photonics Reviews*, vol. 14, no. 8, p. 1900339, 2020.

[30] W. Liang, A. A. Savchenkov, V. S. Ilchenko, D. Eliyahu, D. Seidel, A. B. Matsko, and L. Maleki, "Generation of a coherent near-infrared kerr frequency comb in a monolithic microresonator with normal gvd," *Optics letters*, vol. 39, no. 10, pp. 2920–2923, 2014.

[31] X. Xue, Y. Xuan, Y. Liu, P.-H. Wang, S. Chen, J. Wang, D. E. Leaird, M. Qi, and A. M. Weiner, "Mode-locked dark pulse kerr combs in normal-dispersion microresonators," *Nature Photonics*, vol. 9, no. 9, p. 594, 2015.

[32] X. Xue, P.-H. Wang, Y. Xuan, M. Qi, and A. M. Weiner, "Microresonator kerr frequency combs with high conversion efficiency," *Laser & Photonics Reviews*, vol. 11, no. 1, p. 1600276, 2017.

[33] P. Imany, J. A. Jaramillo-Villegas, O. D. Odele, K. Han, D. E. Leaird, J. M. Lukens, P. Lougovski, M. Qi, and A. M. Weiner, "50-GHz-spaced comb of high-dimensional frequency-bin entangled photons from an on-chip silicon nitride microresonator," *Optics express*, vol. 26, no. 2, pp. 1825–1840, 2018.

[34] C. Reimer, M. Kues, P. Roztocki, B. Wetzel, F. Grazioso, B. E. Little, S. T. Chu, T. Johnston, Y. Bromberg, L. Caspani *et al.*, "Generation of multiphoton entangled quantum states by means of integrated frequency combs," *Science*, vol. 351, no. 6278, pp. 1176–1180, 2016.

[35] H.-H. Lu, J. M. Lukens, N. A. Peters, O. D. Odele, D. E. Leaird, A. M. Weiner, and P. Lougovski, "Electro-optic frequency beam splitters and tritters for high-fidelity photonic quantum information processing," *Physical review letters*, vol. 120, no. 3, p. 030502, 2018.

[36] H.-H. Lu, J. M. Lukens, B. P. Williams, P. Imany, N. A. Peters, A. M. Weiner, and P. Lougovski, "A controlled-NOT gate for frequency-bin qubits," *npj Quantum Information*, vol. 5, no. 1, p. 24, 2019.

[37] M. Kues, C. Reimer, J. M. Lukens, W. J. Munro, A. M. Weiner, D. J. Moss, and R. Morandotti, "Quantum optical microcombs," *Nature Photonics*, vol. 13, no. 3, p. 170, 2019.

[38] P. Imany, M. S. Alshaykh, J. M. Lukens, A. J. Moore, D. E. Leaird, and A. M. Weiner, "Demonstration of four-party 32-dimensional greenberger-horne-zeilinger entangled state," in *CLEO: QELS_Fundamental Science*. Optical Society of America, 2019, pp. JTh5C–5.

[39] P. Imany, M. S. Alshaykh, J. M. Lukens, J. A. Jaramillo-Villegas, D. E. Leaird, and A. M. Weiner, "A two-qudit operation on a 256-dimensional hilbert space," in *CLEO: QELS_Fundamental Science*. Optical Society of America, 2019, pp. JTu3A–3.

[40] P. Imany, J. A. Jaramillo-Villegas, M. S. Alshaykh, J. M. Lukens, O. D. Odele, A. J. Moore, D. E. Leaird, M. Qi, and A. M. Weiner, "High-dimensional optical quantum logic in large operational spaces," *npj Quantum Information*, vol. 5, no. 1, pp. 1–10, 2019.

[41] P. W. Shor, "Polynomial-time algorithms for prime factorization and discrete logarithms on a quantum computer," *SIAM review*, vol. 41, no. 2, pp. 303–332, 1999.

[42] A. Aspuru-Guzik and P. Walther, "Photonic quantum simulators," *Nature physics*, vol. 8, no. 4, p. 285, 2012.

[43] J. J. Morton and B. W. Lovett, "Hybrid solid-state qubits: the powerful role of electron spins," *Annu. Rev. Condens. Matter Phys.*, vol. 2, no. 1, pp. 189–212, 2011.

[44] J. J. Pla, K. Y. Tan, J. P. Dehollain, W. H. Lim, J. J. Morton, F. A. Zwanenburg, D. N. Jamieson, A. S. Dzurak, and A. Morello, "High-fidelity readout and control of a nuclear spin qubit in silicon," *Nature*, vol. 496, no. 7445, p. 334, 2013.

[45] H. Bernien, S. Schwartz, A. Keesling, H. Levine, A. Omran, H. Pichler, S. Choi, A. S. Zibrov, M. Endres, M. Greiner *et al.*, "Probing many-body dynamics on a 51-atom quantum simulator," *Nature*, vol. 551, no. 7682, p. 579, 2017.

[46] J. Zhang, G. Pagano, P. W. Hess, A. Kyprianidis, P. Becker, H. Kaplan, A. V. Gorshkov, Z.-X. Gong, and C. Monroe, "Observation of a many-body dynamical phase transition with a 53-qubit quantum simulator," *Nature*, vol. 551, no. 7682, p. 601, 2017.

[47] F. Arute, K. Arya, R. Babbush, D. Bacon, J. C. Bardin, R. Barends, R. Biswas, S. Boixo, F. G. S. L. Brandao, D. A. Buell, B. Burkett, Y. Chen, Z. Chen, B. Chiaro, R. Collins, W. Courtney, A. Dunsworth, E. Farhi, B. Foxen, A. Fowler, C. Gidney, M. Giustina, R. Graff, K. Guerin, S. Habegger, M. P. Harrigan, M. J. Hartmann, A. Ho, M. Hoffmann, T. Huang, T. S. Humble, S. V. Isakov, E. Jeffrey, Z. Jiang, D. Kafri, K. Kechedzhi, J. Kelly, P. V. Klimov, S. Knysh, A. Korotkov, F. Kostritsa, D. Landhuis, M. Lindmark, E. Lucero, D. Lyakh, S. Mandrà, J. R. McClean, M. McEwen, A. Megrant, X. Mi, K. Michielsen, M. Mohseni, J. Mutus, O. Naaman, M. Neeley, C. Neill, M. Y. Niu, E. Ostby, A. Petukhov, J. C. Platt, C. Quintana, E. G. Rieffel, P. Roushan, N. C. Rubin, D. Sank, K. J. Satzinger, V. Smelyanskiy, K. J. Sung, M. D. Trevithick, A. Vainsencher, B. Villalonga, T. White, Z. J. Yao, P. Yeh, A. Zalcman, H. Neven, and J. M. Martinis, "Quantum supremacy using a programmable superconducting processor," *Nature*, vol. 574, no. 7779, pp. 505–510, 2019. [Online]. Available: https://doi.org/10.1038/s41586-019-1666-5

[48] P. Krantz, M. Kjaergaard, F. Yan, T. P. Orlando, S. Gustavsson, and W. D. Oliver, "A quantum engineer's guide to superconducting qubits," *Applied Physics Reviews*, vol. 6, no. 2, p. 021318, 2019.

[49] N. Somaschi, V. Giesz, L. De Santis, J. Loredo, M. P. Almeida, G. Hornecker, S. L. Portalupi, T. Grange, C. Antón, J. Demory *et al.*, "Near-optimal single-photon sources in the solid state," *Nature Photonics*, vol. 10, no. 5, p. 340, 2016.

[50] R. E. Evans, M. K. Bhaskar, D. D. Sukachev, C. T. Nguyen, A. Sipahigil, M. J. Burek, B. Machielse, G. H. Zhang, A. S. Zibrov, E. Bielejec *et al.*, "Photon-mediated interactions between quantum emitters in a diamond nanocavity," *Science*, vol. 362, no. 6415, pp. 662–665, 2018.

[51] T. D. Ladd, F. Jelezko, R. Laflamme, Y. Nakamura, C. Monroe, and J. L. OBrien, "Quantum computers," *nature*, vol. 464, no. 7285, p. 45, 2010.

[52] H. J. Kimble, "The quantum internet," *Nature*, vol. 453, no. 7198, p. 1023, 2008.

[53] A. Crespi, R. Ramponi, R. Osellame, L. Sansoni, I. Bongioanni, F. Sciarrino, G. Vallone, and P. Mataloni, "Integrated photonic quantum gates for polarization qubits," *Nature communications*, vol. 2, p. 566, 2011.

[54] A. Rossi, G. Vallone, A. Chiuri, F. De Martini, and P. Mataloni, "Multipath entanglement of two photons," *Physical review letters*, vol. 102, no. 15, p. 153902, 2009.

[55] A. Babazadeh, M. Erhard, F. Wang, M. Malik, R. Nouroozi, M. Krenn, and A. Zeilinger, "High-dimensional single-photon quantum gates: Concepts and experiments," *Physical review letters*, vol. 119, no. 18, p. 180510, 2017.

[56] P. C. Humphreys, B. J. Metcalf, J. B. Spring, M. Moore, X.-M. Jin, M. Barbieri, W. S. Kolthammer, and I. A. Walmsley, "Linear optical quantum computing in a single spatial mode," *Physical review letters*, vol. 111, no. 15, p. 150501, 2013.

[57] F. Flamini, N. Spagnolo, and F. Sciarrino, "Photonic quantum information processing: a review," *Reports on Progress in Physics*, vol. 82, no. 1, p. 016001, 2018.

[58] M. Fiorentino and F. N. Wong, "Deterministic controlled-not gate for single-photon two-qubit quantum logic," *Physical review letters*, vol. 93, no. 7, p. 070502, 2004.

[59] K. H. Kagalwala, G. Di Giuseppe, A. F. Abouraddy, and B. E. Saleh, "Single-photon three-qubit quantum logic using spatial light modulators," *Nature communications*, vol. 8, no. 1, p. 739, 2017.

[60] W.-T. Fang, Y.-H. Li, Z.-Y. Zhou, L.-X. Xu, G.-C. Guo, and B.-S. Shi, "On-chip generation of time-and wavelength-division multiplexed multiple time-bin entanglement," *Optics express*, vol. 26, no. 10, pp. 12 912–12 921, 2018.

[61] P. C. Humphreys, W. S. Kolthammer, J. Nunn, M. Barbieri, A. Datta, and I. A. Walmsley, "Continuous-variable quantum computing in optical time-frequency modes using quantum memories," *Physical review letters*, vol. 113, no. 13, p. 130502, 2014.

[62] L. Roa, A. Delgado, and I. Fuentes-Guridi, "Optimal conclusive teleportation of quantum states," *Physical Review A*, vol. 68, no. 2, p. 022310, 2003.

[63] D. Boschi, S. Branca, F. De Martini, L. Hardy, and S. Popescu, "Experimental realization of teleporting an unknown pure quantum state via dual classical and einstein-podolsky-rosen channels," *Physical Review Letters*, vol. 80, no. 6, p. 1121, 1998.

[64] Y.-B. Sheng, F.-G. Deng, and G. L. Long, "Complete hyperentangled-bell-state analysis for quantum communication," *Physical Review A*, vol. 82, no. 3, p. 032318, 2010.

[65] G. K. Brennen, S. S. Bullock, and D. P. O'Leary, "Efficient circuits for exact-universal computations with qudits," *arXiv preprint quant-ph/0509161*, 2005.

[66] X. Wang, B. C. Sanders, and D. W. Berry, "Entangling power and operator entanglement in qudit systems," *Physical Review A*, vol. 67, no. 4, p. 042323, 2003.

[67] T. G. Draper, S. A. Kutin, E. M. Rains, and K. M. Svore, "A logarithmic-depth quantum carry-lookahead adder," *Quantum Info. Comput.*, vol. 6, no. 4, p. 351369, Jul. 2006.

[68] L. Li, X. Yi, T. Huang, and R. Minasian, "Microwave photonic filter based on dispersion controlled spectrum slicing technique," *Electronics letters*, vol. 47, no. 8, pp. 511–512, 2011.

[69] L. Li, X. Yi, T. X. Huang, and R. A. Minasian, "Distortion-free spectrum sliced microwave photonic signal processor: analysis, design and implementation," *Optics express*, vol. 20, no. 10, pp. 11 517–11 528, 2012.

[70] C. Reimer, S. Sciara, P. Roztocki, M. Islam, L. R. Cortés, Y. Zhang, B. Fischer, S. Loranger, R. Kashyap, A. Cino *et al.*, "High-dimensional one-way quantum processing implemented on d-level cluster states," *Nature Physics*, vol. 15, no. 2, p. 148, 2019.

[71] K. De Greve, P. L. McMahon, L. Yu, J. S. Pelc, C. Jones, C. M. Natarajan, N. Y. Kim, E. Abe, S. Maier, C. Schneider *et al.*, "Complete tomography of a high-fidelity solid-state entangled spin–photon qubit pair," *Nature communications*, vol. 4, p. 2228, 2013.

[72] R. Blume-Kohout, "Optimal, reliable estimation of quantum states," *New Journal of Physics*, vol. 12, no. 4, p. 043034, 2010.

[73] B. P. Williams and P. Lougovski, "Quantum state estimation when qubits are lost: a no-data-left-behind approach," *New Journal of Physics*, vol. 19, no. 4, p. 043003, 2017.

[74] A. Martin, T. Guerreiro, A. Tiranov, S. Designolle, F. Fröwis, N. Brunner, M. Huber, and N. Gisin, "Quantifying photonic high-dimensional entanglement," *Physical review letters*, vol. 118, no. 11, p. 110501, 2017.

[75] A. Tiranov, S. Designolle, E. Z. Cruzeiro, J. Lavoie, N. Brunner, M. Afzelius, M. Huber, and N. Gisin, "Quantification of multidimensional entanglement stored in a crystal," *Physical Review A*, vol. 96, no. 4, p. 040303, 2017.

[76] M. Erhard, M. Malik, M. Krenn, and A. Zeilinger, "Experimental greenberger–horne–zeilinger entanglement beyond qubits," *Nature Photonics*, vol. 12, no. 12, p. 759, 2018.

[77] J.-W. Pan, D. Bouwmeester, M. Daniell, H. Weinfurter, and A. Zeilinger, "Experimental test of quantum nonlocality in three-photon greenberger–horne–zeilinger entanglement," *Nature*, vol. 403, no. 6769, p. 515, 2000.

[78] X.-L. Wang, Y.-H. Luo, H.-L. Huang, M.-C. Chen, Z.-E. Su, C. Liu, C. Chen, W. Li, Y.-Q. Fang, X. Jiang *et al.*, "18-qubit entanglement with six photons three degrees of freedom," *Physical review letters*, vol. 120, no. 26, p. 260502, 2018.

[79] M. Hillery, V. Bužek, and A. Berthiaume, "Quantum secret sharing," *Physical Review A*, vol. 59, no. 3, p. 1829, 1999.

[80] Z. Zhao, Y.-A. Chen, A.-N. Zhang, T. Yang, H. J. Briegel, and J.-W. Pan, "Experimental demonstration of five-photon entanglement and open-destination teleportation," *Nature*, vol. 430, no. 6995, p. 54, 2004.

[81] M. Pant, D. Towsley, D. Englund, and S. Guha, "Percolation thresholds for photonic quantum computing," *Nature communications*, vol. 10, no. 1, p. 1070, 2019.

[82] M. Kues, C. Reimer, P. Roztocki, L. R. Cortés, S. Sciara, B. Wetzel, Y. Zhang, A. Cino, S. T. Chu, B. E. Little *et al.*, "On-chip generation of high-dimensional entangled quantum states and their coherent control," *Nature*, vol. 546, no. 7660, p. 622, 2017.

[83] J. Wang, S. Paesani, Y. Ding, R. Santagati, P. Skrzypczyk, A. Salavrakos, J. Tura, R. Augusiak, L. Mančinska, D. Bacco *et al.*, "Multidimensional quantum entanglement with large-scale integrated optics," *Science*, vol. 360, no. 6386, pp. 285–291, 2018.

[84] T. Ikuta and H. Takesue, "Four-dimensional entanglement distribution over 100 km," *Scientific reports*, vol. 8, no. 1, p. 817, 2018.

[85] M. Malik, M. Erhard, M. Huber, M. Krenn, R. Fickler, and A. Zeilinger, "Multi-photon entanglement in high dimensions," *Nature Photonics*, vol. 10, no. 4, p. 248, 2016.

[86] M. Erhard, R. Fickler, M. Krenn, and A. Zeilinger, "Twisted photons: new quantum perspectives in high dimensions," *Light: Science & Applications*, vol. 7, no. 3, p. 17146, 2018.

[87] N. T. Islam, C. C. W. Lim, C. Cahall, J. Kim, and D. J. Gauthier, "Provably secure and high-rate quantum key distribution with time-bin qudits," *Science advances*, vol. 3, no. 11, p. e1701491, 2017.

[88] D. Bouwmeester, J.-W. Pan, K. Mattle, M. Eibl, H. Weinfurter, and A. Zeilinger, "Experimental quantum teleportation," *Nature*, vol. 390, no. 6660, p. 575, 1997.

[89] H.-H. Lu, N. Klco, J. M. Lukens, T. D. Morris, A. Bansal, A. Ekström, G. Hagen, T. Papenbrock, A. M. Weiner, M. J. Savage *et al.*, "Simulations of subatomic many-body physics on a quantum frequency processor," *Physical Review A*, vol. 100, no. 1, p. 012320, 2019.

[90] C. Sparrow, E. Martin-Lopez, N. Maraviglia, A. Neville, C. Harrold, J. Carolan, Y. N. Joglekar, T. Hashimoto, N. Matsuda, J. L. OBrien *et al.*, "Simulating the vibrational quantum dynamics of molecules using photonics," *Nature*, vol. 557, no. 7707, p. 660, 2018.

[91] H.-H. Lu, Z. Hu, M. S. Alshaykh, A. J. Moore, Y. Wang, P. Imany, A. M. Weiner, and S. Kais, "Quantum phase estimation with time-frequency qudits in a single photon," *Advanced Quantum Technologies*, vol. 3, no. 2, p. 1900074, 2020.

[92] A. W. Harrow, A. Hassidim, and S. Lloyd, "Quantum algorithm for linear systems of equations," *Phys. Rev. Lett.*, vol. 103, p. 150502, Oct 2009. [Online]. Available: https://link.aps.org/doi/10.1103/PhysRevLett.103.150502

[93] Y. Cao, A. Daskin, S. Frankel, and S. Kais, "Quantum circuit design for solving linear systems of equations," *Molecular Physics*, vol. 110, no. 15-16, pp. 1675–1680, 2012.

[94] A. Aspuru-Guzik, A. D. Dutoi, P. J. Love, and M. Head-Gordon, "Simulated quantum computation of molecular energies," *Science*, vol. 309, no. 5741, pp. 1704–1707, 2005.

[95] H. Wang, S. Kais, A. Aspuru-Guzik, and M. R. Hoffmann, "Quantum algorithm for obtaining the energy spectrum of molecular systems," *Phys. Chem. Chem. Phys.*, vol. 10, pp. 5388–5393, 2008.

[96] A. Daskin and S. Kais, "Decomposition of unitary matrices for finding quantum circuits: Application to molecular hamiltonians," *The Journal of Chemical Physics*, vol. 134, no. 14, p. 144112, 2011.

[97] A. Aspuru-Guzik and P. Walther, "Photonic quantum simulators," *Nature Physics*, vol. 8, p. 285, 2012.

[98] X.-Q. Zhou, P. Kalasuwan, T. C. Ralph, and J. L. O'Brien, "Calculating unknown eigenvalues with a quantum algorithm," *Nat. Photon.*, vol. 7, no. 3, p. 223, 2013.

[99] S. Paesani, A. A. Gentile, R. Santagati, J. Wang, N. Wiebe, D. P. Tew, J. L. O'Brien, and M. G. Thompson, "Experimental bayesian quantum phase estimation on a silicon photonic chip," *Phys. Rev. Lett.*, vol. 118, no. 10, p. 100503, 2017.

[100] P. J. J. O'Malley, R. Babbush, I. D. Kivlichan, J. Romero, J. R. McClean, R. Barends, J. Kelly, P. Roushan, A. Tranter, N. Ding, B. Campbell, Y. Chen, Z. Chen, B. Chiaro, A. Dunsworth, A. G. Fowler, E. Jeffrey, E. Lucero, A. Megrant, J. Y. Mutus, M. Neeley, C. Neill, C. Quintana, D. Sank, A. Vainsencher, J. Wenner, T. C. White, P. V. Coveney, P. J. Love, H. Neven, A. Aspuru-Guzik, and J. M. Martinis, "Scalable quantum simulation of molecular energies," *Phys. Rev. X*, vol. 6, p. 031007, Jul 2016. [Online]. Available: https://link.aps.org/doi/10.1103/PhysRevX.6.031007

[101] M. A. Nielsen and I. L. Chuang, *Quantum Computation and Quantum Information: 10th Anniversary Edition*, 10th ed. New York, NY, USA: Cambridge University Press, 2011.

[102] Y. Cao, S.-G. Peng, C. Zheng, and G.-L. Long, "Quantum fourier transform and phase estimation in qudit system," *Communications in Theoretical Physics*, vol. 55, no. 5, pp. 790–794, may 2011.

[103] M. M. Wilde, *Quantum information theory*. Cambridge University Press, 2013.

[104] H.-H. Lu, J. M. Lukens, N. A. Peters, B. P. Williams, A. M. Weiner, and P. Lougovski, "Quantum interference and correlation control of frequency-bin qubits," *Optica*, vol. 5, no. 11, pp. 1455–1460, Nov 2018.

[105] H.-H. Lu, E. M. Simmerman, P. Lougovski, A. M. Weiner, and J. M. Lukens, "Fully arbitrary control of frequency-bin qubits," *Phys. Rev. Lett.*, vol. 125, p. 120503, Sep 2020. [Online]. Available: https://link.aps.org/doi/10.1103/PhysRevLett.125.120503

[106] M. Dobšíček, G. Johansson, V. Shumeiko, and G. Wendin, "Arbitrary accuracy iterative quantum phase estimation algorithm using a single ancillary qubit: A two-qubit benchmark," *Phys. Rev. A*, vol. 76, p. 030306, Sep 2007. [Online]. Available: https://link.aps.org/doi/10.1103/PhysRevA.76.030306

[107] P. Imany, N. B. Lingaraju, M. S. Alshaykh, D. E. Leaird, and A. M. Weiner, "Probing quantum walks through coherent control of high-dimensionally entangled photons," *Science Advances*, vol. 6, no. 29, p. eaba8066, 2020.

[108] A. M. Childs, R. Cleve, E. Deotto, E. Farhi, S. Gutmann, and D. A. Spielman, "Exponential algorithmic speedup by a quantum walk," in *Proceedings of the thirty-fifth annual ACM symposium on Theory of computing*, 2003, pp. 59–68.

[109] A. M. Childs and J. Goldstone, "Spatial search by quantum walk," *Physical Review A*, vol. 70, no. 2, p. 022314, 2004.

[110] S. D. Berry and J. B. Wang, "Two-particle quantum walks: Entanglement and graph isomorphism testing," *Physical Review A*, vol. 83, no. 4, p. 042317, 2011.

[111] P. M. Preiss, R. Ma, M. E. Tai, A. Lukin, M. Rispoli, P. Zupancic, Y. Lahini, R. Islam, and M. Greiner, "Strongly correlated quantum walks in optical lattices," *Science*, vol. 347, no. 6227, pp. 1229–1233, 2015.

[112] A. Peruzzo, M. Lobino, J. C. Matthews, N. Matsuda, A. Politi, K. Poulios, X.-Q. Zhou, Y. Lahini, N. Ismail, K. Wörhoff *et al.*, "Quantum walks of correlated photons," *Science*, vol. 329, no. 5998, pp. 1500–1503, 2010.

[113] T. Eichelkraut, C. Vetter, A. Perez-Leija, H. Moya-Cessa, D. N. Christodoulides, and A. Szameit, "Coherent random walks in free space," *Optica*, vol. 1, no. 4, pp. 268–271, 2014.

[114] G. Di Giuseppe, L. Martin, A. Perez-Leija, R. Keil, F. Dreisow, S. Nolte, A. Szameit, A. Abouraddy, D. Christodoulides, and B. Saleh, "Einstein-podolsky-rosen spatial entanglement in ordered and anderson photonic lattices," *Physical Review Letters*, vol. 110, no. 15, p. 150503, 2013.

[115] H. B. Perets, Y. Lahini, F. Pozzi, M. Sorel, R. Morandotti, and Y. Silberberg, "Realization of quantum walks with negligible decoherence in waveguide lattices," *Physical review letters*, vol. 100, no. 17, p. 170506, 2008.

[116] J. Carolan, J. D. Meinecke, P. J. Shadbolt, N. J. Russell, N. Ismail, K. Wörhoff, T. Rudolph, M. G. Thompson, J. L. O'brien, J. C. Matthews *et al.*, "On the experimental verification of quantum complexity in linear optics," *Nature Photonics*, vol. 8, no. 8, pp. 621–626, 2014.

[117] Y. Lahini, G. R. Steinbrecher, A. D. Bookatz, and D. Englund, "Quantum logic using correlated one-dimensional quantum walks," *npj Quantum Information*, vol. 4, no. 1, pp. 1–7, 2018.

[118] A. Schreiber, K. N. Cassemiro, V. Potoček, A. Gábris, P. J. Mosley, E. Andersson, I. Jex, and C. Silberhorn, "Photons walking the line: a quantum walk with adjustable coin operations," *Physical review letters*, vol. 104, no. 5, p. 050502, 2010.

[119] A. Schreiber, A. Gábris, P. P. Rohde, K. Laiho, M. Štefaňák, V. Potoček, C. Hamilton, I. Jex, and C. Silberhorn, "A 2d quantum walk simulation of two-particle dynamics," *Science*, vol. 336, no. 6077, pp. 55–58, 2012.

[120] F. Cardano, F. Massa, H. Qassim, E. Karimi, S. Slussarenko, D. Paparo, C. de Lisio, F. Sciarrino, E. Santamato, R. W. Boyd *et al.*, "Quantum walks and wavepacket dynamics on a lattice with twisted photons," *Science advances*, vol. 1, no. 2, p. e1500087, 2015.

[121] P. L. Knight, E. Roldán, and J. E. Sipe, "Quantum walk on the line as an interference phenomenon," *Physical Review A*, vol. 68, no. 2, p. 020301, 2003.

[122] C. Reimer, Y. Hu, A. Shams-Ansari, M. Zhang, and M. Loncar, "High-dimensional frequency crystals and quantum walks in electro-optic microcombs," *arXiv preprint arXiv:1909.01303*, 2019.

[123] D. Bouwmeester, I. Marzoli, G. P. Karman, W. Schleich, and J. Woerdman, "Optical galton board," *Physical Review A*, vol. 61, no. 1, p. 013410, 1999.

[124] M. Karski, L. Förster, J.-M. Choi, A. Steffen, W. Alt, D. Meschede, and A. Widera, "Quantum walk in position space with single optically trapped atoms," *Science*, vol. 325, no. 5937, pp. 174–177, 2009.

[125] P. Imany, O. D. Odele, M. S. Alshaykh, H.-H. Lu, D. E. Leaird, and A. M. Weiner, "Frequency-domain hong–ou–mandel interference with linear optics," *Opt. Lett.*, vol. 43, no. 12, pp. 2760–2763, 2018.

[126] A. Pe'Er, B. Dayan, A. A. Friesem, and Y. Silberberg, "Temporal shaping of entangled photons," *Physical review letters*, vol. 94, no. 7, p. 073601, 2005.

[127] J. C. Matthews, K. Poulios, J. D. Meinecke, A. Politi, A. Peruzzo, N. Ismail, K. Wörhoff, M. G. Thompson, and J. L. O'brien, "Observing fermionic statistics with photons in arbitrary processes," *Scientific reports*, vol. 3, no. 1, pp. 1–7, 2013.

[128] L. Sansoni, F. Sciarrino, G. Vallone, P. Mataloni, A. Crespi, R. Ramponi, and R. Osellame, "Two-particle bosonic-fermionic quantum walk via integrated photonics," *Physical review letters*, vol. 108, no. 1, p. 010502, 2012.

[129] M. Lebugle, M. Gräfe, R. Heilmann, A. Perez-Leija, S. Nolte, and A. Szameit, "Experimental observation of n00n state bloch oscillations," *Nature communications*, vol. 6, no. 1, pp. 1–7, 2015.

[130] A. F. Abouraddy, G. Di Giuseppe, D. N. Christodoulides, and B. E. Saleh, "Anderson localization and colocalization of spatially entangled photons," *Physical Review A*, vol. 86, no. 4, p. 040302, 2012.

[131] M. Blok, V. Ramasesh, T. Schuster, K. O'Brien, J. Kreikebaum, D. Dahlen, A. Morvan, B. Yoshida, N. Yao, and I. Siddiqi, "Quantum information scrambling in a superconducting qutrit processor," *arXiv preprint arXiv:2003.03307*, 2020.

[132] C. Gneiting, D. Leykam, and F. Nori, "Disorder-robust entanglement transport," *Physical review letters*, vol. 122, no. 6, p. 066601, 2019.

[133] P. Imany, O. D. Odele, J. A. Jaramillo-Villegas, D. E. Leaird, and A. M. Weiner, "Characterization of coherent quantum frequency combs using electro-optic phase modulation," *Physical Review A*, vol. 97, no. 1, p. 013813, 2018.

[134] J. Bavaresco, N. H. Valencia, C. Klöckl, M. Pivoluska, P. Erker, N. Friis, M. Malik, and M. Huber, "Measurements in two bases are sufficient for certifying high-dimensional entanglement," *Nature Physics*, vol. 14, no. 10, pp. 1032–1037, 2018.

[135] M. S. Alshaykh, D. E. Leaird, J. D. McKinney, and A. M. Weiner, "Rapid wideband RF subsampling and disambiguation using dual combs," in *CLEO: Science and Innovations*. Optical Society of America, 2019, pp. SF2N–8.

[136] R. Maleh, G. L. Fudge, F. A. Boyle, and P. E. Pace, "Analog-to-information and the nyquist folding receiver," *IEEE Journal on Emerging and Selected Topics in Circuits and Systems*, vol. 2, no. 3, pp. 564–578, 2012.

[137] E. H. Chan and R. A. Minasian, "Microwave photonic downconverter with high conversion efficiency," *Journal of Lightwave Technology*, vol. 30, no. 23, pp. 3580–3585, 2012.

[138] B. M. Haas and J. D. McKinney, "Multi-band RF downconversion over fiber with a single modulator," *IEEE Photonics Technology Letters*, vol. 30, no. 18, pp. 1633–1636, 2018.

[139] S. R. Harmon and J. D. McKinney, "Broadband RF disambiguation in subsampled analog optical links via intentionally-introduced sampling jitter," *Optics express*, vol. 22, no. 20, pp. 23 928–23 937, 2014.

[140] S. R. Harmon and J. D. Mckinney, "Precision broadband RF signal recovery in subsampled analog optical links," *IEEE Photonics Technology Letters*, vol. 27, no. 6, pp. 620–623, 2014.

[141] A. Klee, C. Middleton, and R. DeSalvo, "Dual-comb spectrometer for fast wideband RF spectral analysis," in *2017 IEEE Photonics Conference (IPC)*. IEEE, 2017, pp. 379–380.

[142] A. Djupsjobacka, "Residual chirp in integrated-optic modulators," *IEEE Photonics Technology Letters*, vol. 4, no. 1, pp. 41–43, 1992.

[143] P. Almeida and H. Silva, "Expressions of the chirp parameter components for intensity modulation with a dual-electrode mach-zehnder modulator," in *2012 14th International Conference on Transparent Optical Networks (ICTON)*. IEEE, 2012, pp. 1–4.

[144] M. S. Alshaykh, Y. Xuan, D. E. Leaird, J. D. McKinney, M. Qi, and A. M. Weiner, "Kerr combs for stimulated brillouin scattering mitigation in long-haul analog optical links," *Journal of Lightwave Technology*, 2019.

[145] S. Montebugnoli, M. Boschi, F. Perini, P. Faccin, G. Brunori, and E. Pirazzini, "Large antenna array remoting using radio-over-fiber techniques for radio astronomical application," *Microwave and Optical technology letters*, vol. 46, no. 1, pp. 48–54, 2005.

[146] W. Shillue, "Fiber distribution of local oscillator for atacama large millimeter array," in *OFC/NFOEC 2008-2008 Conference on Optical Fiber Communication/National Fiber Optic Engineers Conference*. IEEE, 2008, pp. 1–3.

[147] Y. He, K. G. Baldwin, B. J. Orr, R. B. Warrington, M. J. Wouters, A. N. Luiten, P. Mirtschin, T. Tzioumis, C. Phillips, J. Stevens *et al.*, "Long-distance telecom-fiber transfer of a radio-frequency reference for radio astronomy," *Optica*, vol. 5, no. 2, pp. 138–146, 2018.

[148] G. C. Tavik, C. L. Hilterbrick, J. B. Evins, J. J. Alter, J. G. Crnkovich, J. W. de Graaf, W. Habicht, G. P. Hrin, S. A. Lessin, D. C. Wu *et al.*, "The advanced multifunction RF concept," *IEEE Transactions on Microwave Theory and Techniques*, vol. 53, no. 3, pp. 1009–1020, 2005.

[149] R. A. Minasian, "Ultra-wideband and adaptive photonic signal processing of microwave signals," *IEEE Journal of Quantum Electronics*, vol. 52, no. 1, pp. 1–13, 2015.

[150] V. J. Urick, K. J. Williams, and J. D. McKinney, *Fundamentals of microwave photonics*. John Wiley & Sons, 2015.

[151] C. De Oliveira, C.-K. Jen, A. Shang, and C. Saravanos, "Stimulated brillouin scattering in cascaded fibers of different brillouin frequency shifts," *JOSA B*, vol. 10, no. 6, pp. 969–972, 1993.

[152] H. Wen, H. Zheng, Q. Mo, A. M. Velázquez-Benítez, C. Xia, B. Huang, H. Liu, H. Yu, P. Sillard, J. E. A. Lopez *et al.*, "Few-mode fibre-optic microwave photonic links," *Light: Science & Applications*, vol. 6, no. 8, p. e17021, 2017.

[153] J. D. McKinney, V. J. Urick, and J. Briguglio, "Optical comb sources for high dynamic-range single-span long-haul analog optical links," *IEEE Transactions on Microwave Theory and Techniques*, vol. 59, no. 12, pp. 3249–3257, 2011.

[154] P. Marin-Palomo, J. N. Kemal, M. Karpov, A. Kordts, J. Pfeifle, M. H. Pfeiffer, P. Trocha, S. Wolf, V. Brasch, M. H. Anderson *et al.*, "Microresonator-based solitons for massively parallel coherent optical communications," *Nature*, vol. 546, no. 7657, p. 274, 2017.

[155] A. Fülöp, M. Mazur, A. Lorences-Riesgo, Ó. B. Helgason, P.-H. Wang, Y. Xuan, D. E. Leaird, M. Qi, P. A. Andrekson, A. M. Weiner *et al.*, "High-order coherent communications using mode-locked dark-pulse Kerr combs from microresonators," *Nature communications*, vol. 9, no. 1, p. 1598, 2018.

[156] D. Marpaung, J. Yao, and J. Capmany, "Integrated microwave photonics," *Nature photonics*, vol. 13, no. 2, p. 80, 2019.

[157] X. Xue, Y. Xuan, C. Bao, S. Li, X. Zheng, B. Zhou, M. Qi, and A. M. Weiner, "Microcomb-based true-time-delay network for microwave beamforming with arbitrary beam pattern control," *Journal of Lightwave Technology*, vol. 36, no. 12, pp. 2312–2321, 2018.

[158] X. Xu, J. Wu, T. G. Nguyen, T. Moein, S. T. Chu, B. E. Little, R. Morandotti, A. Mitchell, and D. J. Moss, "Photonic microwave true time delays for phased array antennas using a 49 GHz fsr integrated optical micro-comb source," *Photonics Research*, vol. 6, no. 5, pp. B30–B36, 2018.

[159] D. T. Spencer, T. Drake, T. C. Briles, J. Stone, L. C. Sinclair, C. Fredrick, Q. Li, D. Westly, B. R. Ilic, A. Bluestone *et al.*, "An optical-frequency synthesizer using integrated photonics," *Nature*, vol. 557, no. 7703, p. 81, 2018.

[160] C. Bao, Y. Xuan, C. Wang, J. A. Jaramillo-Villegas, D. E. Leaird, M. Qi, and A. M. Weiner, "Soliton repetition rate in a silicon-nitride microresonator," *Optics letters*, vol. 42, no. 4, pp. 759–762, 2017.

[161] X. Xue, Y. Xuan, Y. Liu, P.-H. Wang, S. Chen, J. Wang, D. E. Leaird, M. Qi, and A. M. Weiner, "Mode-locked dark pulse Kerr combs in normal-dispersion microresonators," *Nature Photonics*, vol. 9, no. 9, p. 594, 2015.

[162] X. Xue, M. Qi, and A. M. Weiner, "Normal-dispersion microresonator Kerr frequency combs," *Nanophotonics*, vol. 5, no. 2, pp. 244–262, 2016.

[163] C. Wang, C. Bao, Y. Xuan, K. Han, D. E. Leaird, M. Qi, and A. M. Weiner, "Normal dispersion high conversion efficiency Kerr comb with 50 GHz repetition rate," in *CLEO: Science and Innovations*. Optical Society of America, 2017, pp. SW4N–5.

[164] M. H. Pfeiffer, J. Liu, A. S. Raja, T. Morais, B. Ghadiani, and T. J. Kippenberg, "Ultra-smooth silicon nitride waveguides based on the damascene reflow process: fabrication and loss origins," *Optica*, vol. 5, no. 7, pp. 884–892, 2018.

[165] E. Hamidi, D. E. Leaird, and A. M. Weiner, "Tunable programmable microwave photonic filters based on an optical frequency comb," *IEEE Transactions on Microwave Theory and Techniques*, vol. 58, no. 11, pp. 3269–3278, 2010.

[166] Z. Jiang, S.-D. Yang, D. E. Leaird, and A. M. Weiner, "Fully dispersion-compensated 500 fs pulse transmission over 50 km single-mode fiber," *Optics letters*, vol. 30, no. 12, pp. 1449–1451, 2005.

[167] A. W. S. Putra, M. Yamada, H. Tsuda, and S. Ambran, "Theoretical analysis of noise in erbium doped fiber amplifier," *IEEE Journal of Quantum Electronics*, vol. 53, no. 4, pp. 1–8, 2017.

[168] P. S. Devgan, V. J. Urick, K. J. Williams, and J. F. Diehl, "Long-haul microwave analog link with shot-noise-limited performance above the stimulated brillouin scattering threshold," in *2008 International Topical Meeting on Microwave Photonics jointly held with the 2008 Asia-Pacific Microwave Photonics Conference*. IEEE, 2009, pp. 326–329.

[169] A. B. Matsko and L. Maleki, "Feshbach resonances in Kerr frequency combs," *Physical Review A*, vol. 91, no. 1, p. 013831, 2015.

[170] ——, "Noise conversion in Kerr comb RF photonic oscillators," *JOSA B*, vol. 32, no. 2, pp. 232–240, 2015.

[171] J. Zhang and M. Phillips, "Modeling intensity noise caused by stimulated brillouin scattering in optical fibers," in *(CLEO). Conference on Lasers and Electro-Optics, 2005.*, vol. 1. IEEE, 2005, pp. 140–142.

[172] V. J. Urick, P. F. Knapp, L. Swingen, M. S. Rogge, A. L. Campillo, F. Bucholtz, and J. L. Dexter, "Design and characterization of long-haul single-channel intensity-modulated analog fiber-optic links," NAVAL RESEARCH LAB WASHINGTON DC, Tech. Rep., 2005.

[173] H.-J. Kim, D. E. Leaird, A. J. Metcalf, and A. M. Weiner, "Comb-based RF photonic filters based on interferometric configuration and balanced detection," *Journal of Lightwave Technology*, vol. 32, no. 20, pp. 3478–3488, 2014.

[174] X. Xue, P.-H. Wang, Y. Xuan, M. Qi, and A. M. Weiner, "Microresonator Kerr frequency combs with high conversion efficiency," *Laser & Photonics Reviews*, vol. 11, no. 1, p. 1600276, 2017.

[175] T. Nakamura, J. Davila-Rodriguez, H. Leopardi, J. A. Sherman, T. M. Fortier, X. Xie, J. C. Campbell, W. F. McGrew, X. Zhang, Y. S. Hassan *et al.*, "Coherent optical clock down-conversion for microwave frequencies with 10- 18 instability," *Science*, vol. 368, no. 6493, pp. 889–892, 2020.

[176] J. P. Turneaure, C. M. Will, B. F. Farrell, E. M. Mattison, and R. F. Vessot, "Test of the principle of equivalence by a null gravitational red-shift experiment," *Physical Review D*, vol. 27, no. 8, p. 1705, 1983.

[177] C. M. Will, "The confrontation between general relativity and experiment," *Living reviews in relativity*, vol. 9, no. 1, p. 3, 2006.

[178] L. Cacciapuoti, C. Salomon *et al.*, "Atomic clock ensemble in space," in *Journal of Physics-Conference Series*, vol. 327, no. 1, 2011, p. 012049.

[179] W. Oskay, S. Bize, S. Diddams, U. Tanaka, C. Tanner, T. Parker, R. Drullinger, T. Heavner, S. Jefferts, L. Hollberg *et al.*, "Testing the stability of fundamental constants with the^ 199hg^+ single-ion optical clock," *APS*, vol. 34, pp. B4–004, 2003.

[180] D. Lebach, B. Corey, I. Shapiro, M. Ratner, J. Webber, A. Rogers, J. Davis, and T. Herring, "Measurement of the solar gravitational deflection of radio waves using very-long-baseline interferometry," *Physical Review Letters*, vol. 75, no. 8, p. 1439, 1995.

[181] W. McGrew, X. Zhang, R. Fasano, S. Schäffer, K. Beloy, D. Nicolodi, R. Brown, N. Hinkley, G. Milani, M. Schioppo *et al.*, "Atomic clock performance enabling geodesy below the centimetre level," *Nature*, vol. 564, no. 7734, pp. 87–90, 2018.

[182] S. Kolkowitz, I. Pikovski, N. Langellier, M. D. Lukin, R. L. Walsworth, and J. Ye, "Gravitational wave detection with optical lattice atomic clocks," *Physical Review D*, vol. 94, no. 12, p. 124043, 2016.

[183] T. E. Drake, T. C. Briles, J. R. Stone, D. T. Spencer, D. R. Carlson, D. D. Hickstein, Q. Li, D. Westly, K. Srinivasan, S. A. Diddams *et al.*, "Terahertz-rate kerr-microresonator optical clockwork," *Physical Review X*, vol. 9, no. 3, p. 031023, 2019.

[184] Z. L. Newman, V. Maurice, T. Drake, J. R. Stone, T. C. Briles, D. T. Spencer, C. Fredrick, Q. Li, D. Westly, B. R. Ilic *et al.*, "Architecture for the photonic integration of an optical atomic clock," *Optica*, vol. 6, no. 5, pp. 680–685, 2019.

[185] H. R. Telle, G. Steinmeyer, A. E. Dunlop, J. Stenger, D. H. Sutter, and U. Keller, "Carrier-envelope offset phase control: A novel concept for absolute optical frequency measurement and ultrashort pulse generation," *Applied Physics B*, vol. 69, no. 4, pp. 327–332, 1999.

[186] M. S. Alshaykh, D. E. Leaird, and A. M. Weiner, "Investigation of the effect of stimulated raman scattering on parametric pumping of microring resonators," in *CLEO: Applications and Technology*. Optical Society of America, 2018, pp. JTu2A–112.

[187] G. Moille, Q. Li, T. C. Briles, S.-P. Yu, T. Drake, X. Lu, A. Rao, D. Westly, S. B. Papp, and K. Srinivasan, "Broadband resonator-waveguide coupling for efficient extraction of octave-spanning microcombs," *Optics Letters*, vol. 44, no. 19, pp. 4737–4740, 2019.

[188] J. Wang, Y. Xuan, A. M. Weiner, and M. Qi, "Fast and slow optical modulation of refractive index in a sin microring," in *2014 Conference on Lasers and Electro-Optics (CLEO)-Laser Science to Photonic Applications*. IEEE, 2014, pp. 1–2.

[189] T. C. Briles, J. R. Stone, T. E. Drake, D. T. Spencer, C. Frederick, Q. Li, D. A. Westly, B. R. Illic, K. Srinivasan, S. A. Diddams *et al.*, "Kerr-microresonator solitons for accurate carrier-envelope-frequency stabilization," *arXiv preprint arXiv:1711.06251*, 2017.

[190] J. K. Jang, Y. Okawachi, X. Ji, C. Joshi, M. Lipson, and A. L. Gaeta, "Universal conversion efficiency scaling with free-spectral-range for soliton," in *2020 Conference on Lasers and Electro-Optics (CLEO)*. IEEE, 2020, pp. 1–2.

[191] B. Wang, Z. Yang, X. Zhang, and X. Yi, "Vernier frequency division with dual-microresonator solitons," *Nature communications*, vol. 11, no. 1, pp. 1–7, 2020.

[192] D. Flynn and M. O'Hagan, "Measurements of the thermal conductivity and electrical resistivity of platinum from 100 to 900°C," *Precision Measurement and Calibration: Selected NBS Papers on Heat*, vol. 2, p. 334, 1970.

[193] X. Xue, Y. Xuan, C. Wang, P.-H. Wang, Y. Liu, B. Niu, D. E. Leaird, M. Qi, and A. M. Weiner, "Thermal tuning of Kerr frequency combs in silicon nitride microring resonators," *Optics express*, vol. 24, no. 1, pp. 687–698, 2016.

[194] A. Rao, G. Moille, X. Lu, D. Sacchetto, M. Geiselmann, M. Zervas, S. Papp, J. Bowers, and K. Srinivasan, "Integrated photonic interposers for processing octave-spanning microresonator frequency combs," in *CLEO: Science and Innovations*. Optical Society of America, 2020, pp. SF3O–1.

[195] X. Xue, Y. Xuan, P.-H. Wang, Y. Liu, D. E. Leaird, M. Qi, and A. M. Weiner, "Normal-dispersion microcombs enabled by controllable mode interactions," *Laser & Photonics Reviews*, vol. 9, no. 4, pp. L23–L28, 2015.

[196] B. Y. Kim, Y. Okawachi, J. K. Jang, M. Yu, X. Ji, Y. Zhao, C. Joshi, M. Lipson, and A. L. Gaeta, "Turn-key, high-efficiency kerr comb source," *Optics letters*, vol. 44, no. 18, pp. 4475–4478, 2019.

[197] Y. Zhang, M. Menotti, K. Tan, V. Vaidya, D. Mahler, L. Zatti, M. Liscidini, B. Morrison, and Z. Vernon, "Single-mode quadrature squeezing using dual-pump four-wave mixing in an integrated nanophotonic device," *arXiv preprint arXiv:2001.09474*, 2020.

[198] X. LIU, Y. PAN, X. ZHONG, J. XU, Y. HAN, S. YU, and X. CAI, "Highly efficient thermo-optic tunable micro-ring resonator based on thin film lithium niobate platform," *Optics letters*, vol. 45, no. 22, pp. 6318–6321, 2020.

[199] M. Corato-Zanarella, X. Ji, A. Mohanty, U. D. Dave, A. L. Gaeta, and M. Lipson, "Overcoming the trade-off between loss and dispersion in microresonators," in *CLEO: Science and Innovations*. Optical Society of America, 2020, pp. STh1J–1.

[200] K. Sun and A. Beling, "High-speed photodetectors for microwave photonics," *Applied Sciences*, vol. 9, no. 4, p. 623, 2019.

[201] Y. Wang, Z. Hu, B. C. Sanders, and S. Kais, "Qudits and high-dimensional quantum computing," *arXiv preprint arXiv:2008.00959*, 2020.

[202] M. Mosca and M. Piani, "Quantum threat timeline," *Global Risk Institute*, Oct 2019, accessed online October 03 2020. [Online]. Available: https://globalriskinstitute.org/publications/quantum-threat-timeline/

[203] M. Kurek, "Patents, publications and investments in quantum technologies," *Le Lab Quantique*, Sep 2020, accessed online October 03 2020. [Online]. Available: https://lelabquantique.com/kurek-quantum-report/

[204] D. Awschalom, K. K. Berggren, H. Bernien, S. Bhave, L. D. Carr, P. Davids, S. E. Economou, D. Englund, A. Faraon, M. Fejer, S. Guha, M. V. Gustafsson, E. Hu, L. Jiang, J. Kim, B. Korzh, P. Kumar, P. G. Kwiat, M. Lonar, M. D. Lukin, D. A. B. Miller, C. Monroe, S. W. Nam, P. Narang, J. S. Orcutt, M. G. Raymer, A. H. Safavi-Naeini, M. Spiropulu, K. Srinivasan, S. Sun, J. Vukovi, E. Waks, R. Walsworth, A. M. Weiner, and Z. Zhang, "Development of quantum interconnects for next-generation information technologies," *arXiv preprint arXiv:1912.06642*, 2019.

[205] X. Xue, X. Zheng, and B. Zhou, "Super-efficient temporal solitons in mutually coupled optical cavities," *Nature Photonics*, vol. 13, no. 9, pp. 616–622, 2019.

[206] B. Shen, L. Chang, J. Liu, H. Wang, Q.-F. Yang, C. Xiang, R. N. Wang, J. He, T. Liu, W. Xie *et al.*, "Integrated turnkey soliton microcombs," *Nature*, vol. 582, no. 7812, pp. 365–369, 2020.

[207] T. Hansson, P. Parra-Rivas, M. Bernard, F. Leo, L. Gelens, and S. Wabnitz, "Quadratic soliton combs in doubly resonant second-harmonic generation," *Optics letters*, vol. 43, no. 24, pp. 6033–6036, 2018.

[208] M. Piccardo, B. Schwarz, D. Kazakov, M. Beiser, N. Opačak, Y. Wang, S. Jha, J. Hillbrand, M. Tamagnone, W. T. Chen *et al.*, "Frequency combs induced by phase turbulence," *Nature*, vol. 582, no. 7812, pp. 360–364, 2020.

[209] A. K. Tusnin, A. M. Tikan, and T. J. Kippenberg, "Nonlinear states and dynamics in a synthetic frequency dimension," *arXiv*, pp. arXiv–2004, 2020.

[210] A. W. Bruch, X. Liu, Z. Gong, J. B. Surya, M. Li, C.-L. Zou, H. Tang *et al.*, "Pockels soliton microcomb," *arXiv preprint arXiv:2004.07708*, 2020.

[211] X. Xue, F. Leo, Y. Xuan, J. A. Jaramillo-Villegas, P.-H. Wang, D. E. Leaird, M. Erkintalo, M. Qi, and A. M. Weiner, "Second-harmonic-assisted four-wave mixing in chip-based microresonator frequency comb generation," *Light: Science & Applications*, vol. 6, no. 4, pp. e16 253–e16 253, 2017.

[212] X. Zhu, C.-H. Chang, C. González-Arciniegas, J. Higgins, A. Pe'er, and O. Pfister, "Graph state engineering by phase modulation of the quantum optical frequency comb," *arXiv preprint arXiv:1912.11215*, 2019.

[213] P. Brochard, S. Schilt, and T. Südmeyer, "Ultra-low noise microwave generation with a free-running optical frequency comb transfer oscillator," *Optics letters*, vol. 43, no. 19, pp. 4651–4654, 2018.

APPENDIX

A. FREQUENCY INSTABILITY DERIVATION

Here I will derive the instability equations shown in ch. 7. The first section addresses the dual-comb division schemes, the second covers the stabilization and the locking of the main comb to the clock laser, and finally, I discuss electronic mixing as an alternative to phase-locked loops.

A.1 Dual-comb optical division

In the dual-comb scheme, we assume that the two combs are pumped using the same laser and that the overlapping comb lines far away from the shared pump line ($\nu_o + M_1 f_{rep}$ and $\nu_o + M_2 f_{rep_2}$ where M_1, M_2 are integers) are locked together. Here comb-2 has a repetition rate of $f_{rep_2} = f_{rep} + \delta f$

$$f_{overlap} = (\nu_o + M_2 f_{rep_2}) - (\nu_o + M_1 f_{rep}) \tag{A.1}$$

Adding a linear perturbation (i.e. $f \approx f + \Delta f$) and collecting the frequency instability terms we get

$$\Delta f_{overlap} = (\Delta\nu_o + M_2 \Delta f_{rep_2}) - (\Delta\nu_o + M_1 \Delta f_{rep}) \tag{A.2}$$

$$\Delta f_{rep_2} = \frac{1}{M_2}\Delta f_{overlap} + \frac{M_1}{M_2}\Delta f_{rep} \tag{A.3}$$

For the *Vernier division scheme* , the clock output will be the beating of the first sideband pairs of the two combs (δf), so

$$\Delta f_{clk} = \Delta\delta f \tag{A.4}$$

$$= \Delta f_{rep_2} - \Delta f_{rep} \tag{A.5}$$

$$= \frac{1}{M_2}\Delta f_{overlap} + \frac{M_1 - M_2}{M_2}\Delta f_{rep} \tag{A.6}$$

using eq. A.1 we can rewrite $\frac{M_1-M_2}{M_2}$ more generally as $\frac{\delta_f}{f_{rep}}$. Therefore, we obtain

$$\Delta f_{clk} = \frac{1}{M_2}\Delta f_{overlap} + \frac{\delta f}{f_{rep}}\Delta f_{rep} \tag{A.7}$$

For the *conventional dual-comb division scheme*, the clock output is simply the repetition rate of the secondary comb (eq.A.3). Given that $f_{rep} \approx n \cdot f_{rep_2}$ where n is an integer, then $M_2 = n \cdot M_1$, so we can rewrite eq.A.3 more generally as

$$\Delta f_{clk} = \Delta f_{rep_2} = \frac{1}{M_2}\Delta f_{overlap} + \frac{f_{rep_2}}{f_{rep}}\Delta f_{rep} \tag{A.8}$$

A.2 Stabilization of the main comb

A.2.1 Direct second harmonic scheme

Following the previous method, we start from the carrier envelope offset locking through f-2f scheme

$$\nu_o + N f_{rep} - 2(\nu_o - M f_{rep}) = f_{ceo} \tag{A.9}$$

Where N and M are integers, f_{rep} is the comb's free spectral range or repetition rate, ν_o is the pump frequency and f_{ceo} refers to the detected RF beatnote after heterodyning the $1\mu m$ comb line ($\nu_o + N f_{rep}$) and frequency doubled $2\mu m$ ($\nu_o - M f_{rep}$) comb line. Reorganizing the equation then writing it in terms of frequency instabilities, we get

$$\begin{aligned} (N+2M)\ f_{rep} - \nu_o &= f_{ceo} \\ Instability \rightarrow (N+2M)\ \Delta f_{rep} - \Delta\nu_o &= \Delta f_{ceo} \\ and\ using \quad (N+2M) &= \frac{\nu_o + f_{ceo}}{f_{rep}} \approx \frac{\nu_o}{f_{rep}} \end{aligned}$$

we get

$$\Delta\nu_o = \frac{\nu_o}{f_{rep}}\ \Delta f_{rep} - \Delta f_{ceo} \tag{A.10}$$

Now, a comb line at $2 \times 871nm$ written as $(\nu_o - Af_{rep})$ where A is an integer, from the main comb is frequency doubled to beat with clock laser locked to the atomic transition (ν_{clk})

$$2(\nu_o - Af_{rep}) - \nu_{clk} = f_{comb_{871}} \tag{A.11}$$

$$\rightarrow \quad 2(\Delta\nu_o - A\Delta f_{rep}) - \Delta\nu_{clk} = \Delta f_{comb_{871}} \tag{A.12}$$

Solving for Δf_{rep}

$$\Delta f_{rep} = \Delta\nu_o/A - \Delta f_{comb_{871}}/2A - \Delta\nu_{clk}/2A \tag{A.13}$$

substituting eg.A.10 in eg.A.13

$$\Delta f_{rep} = \left(\frac{\nu_o}{A \cdot f_{rep}} \, \Delta f_{rep} - \Delta f_{ceo}/A - \Delta f_{comb_{871}}/2A - \Delta\nu_{clk}/2A \right) \tag{A.14}$$

$$\Delta f_{rep} \left(\frac{A \cdot f_{rep} - \nu_o}{A \cdot f_{rep}} \right) = -\Delta f_{ceo}/A - \Delta f_{comb_{871}}/2A - \Delta\nu_{clk}/2A \tag{A.15}$$

By substituting $\nu_o - A \cdot f_{rep}$ by $\nu_{clk}/2$ and reorganizing the terms we get eq. 7.7:

$$\Delta f_{rep} = \frac{f_{rep}}{\nu_{clk}} \big(2\Delta f_{ceo} + \Delta f_{comb_{871}} + \Delta\nu_{clk} \big)$$

A.2.2 Sum frequency generation scheme

Instead of frequency doubling a comb line to lock to the clock laser, we'll look a the case of performing sum frequency generation between a line at $\sim$ 1550 nm $(\nu_o - N_1 f_{rep})$ and a line from the second comb around $\sim$ 1988 nm $(\nu_o - N_2 f_{rep_2})$. Therefore, we get

$$\nu_o - N_1 f_{rep} + \nu_o - N_2 f_{rep_2} - \nu_{clk} = f_{comb_{871}} \tag{A.16}$$

and

$$N_1 \Delta f_{rep} = (2\Delta\nu_o - \Delta f_{comb_{871}} - N_2 \Delta f_{rep_2} - \Delta\nu_{clk}) \tag{A.17}$$

Note that the previously derived equations for the CEO (eq.A.10) and the comb overlap (eq.A.3) still apply. Substituting these expressions we get

$$\Delta f_{rep} = \frac{M_2 f_{rep} \cdot \left(2\Delta f_{ceo} + \Delta f_{comb_{871}} + \frac{N_2}{M_2}\Delta f_{overlap} + \Delta\nu_{clk}\right)}{2M_2\nu_o - N_2 M_1 f_{rep} - N_1 M_2 f_{rep}} \tag{A.18}$$

Given that $M_1 f_{rep} = M_2 f_{rep_2} - f_{overlap} \approx M_2 f_{rep_2}$, and from eq.A.16 we have $\nu_{clk} \approx 2\nu_o - N_1 f_{rep} - (N_2 M_1/M_2) f_{rep}$, we can rewrite the expression to obtain eq. 7.8:

$$\Delta f_{rep} = \frac{f_{rep}}{\nu_{clk}} \cdot \left(2\Delta f_{ceo} + \Delta f_{comb_{871}} + \frac{N_2}{M_2}\Delta f_{overlap} + \Delta\nu_{clk}\right)$$

A.2.3 Difference frequency generation

In the DFG scheme we have two locking points: the first being locking the RF beat between the DFG line and a high wavelength comb line around $2\mu m$

$$f_{DFG_{2\mu m}} = (\nu_{clk} - \nu_o) - (\nu_o - D_1 f_{rep})$$

and locking the RF beat between the frequency-doubled DFG line and a low wavelength comb line around $1\mu m$

$$f_{2DFG_{1\mu m}} = 2(\nu_{clk} - \nu_o) - (\nu_o + D_2 f_{rep}) = 2\nu_{clk} - 3\nu_o - D_2 f_{rep}$$

From the prior we obtain

$$D_1 \Delta f_{rep} = (2\Delta\nu_o + \Delta f_{DFG_{2\mu m}} - \Delta\nu_{clk}) \tag{A.19}$$

and from the latter beat ($f_{2DFG_{1\mu m}}$) we get

$$\Delta\nu_o = (2\Delta\nu_{clk} - D_2\Delta f_{rep} - \Delta f_{2DFG_{1\mu m}})/3 \tag{A.20}$$

Substituting eq. A.20 in eq. A.19 we get

$$(D_1 + \frac{2}{3}D_2)\Delta f_{rep} = (\Delta f_{DFG_{2\mu m}} - 2\Delta f_{2DFG_{1\mu m}}/3 + \Delta\nu_{clk}/3) \tag{A.21}$$

To obtain a more general expression we can use

$$(D_1 + \frac{2}{3}D_2) \approx \frac{2\nu_o - \nu_{clk}}{f_{rep}} + \frac{2}{3} \cdot \frac{2\nu_{clk} - 3\nu_o}{f_{rep}} \tag{A.22}$$

$$= \frac{2\nu_o - \nu_{clk} + 4\nu_{clk}/3 + 2\nu_o}{f_{rep}} \tag{A.23}$$

$$= \frac{\nu_{clk}/3}{f_{rep}} \tag{A.24}$$

Using this expression, we obtain eq. 7.9:

$$\Delta f_{rep} = \frac{f_{rep}}{\nu_{clk}}\left(3\Delta f_{DFG_{2\mu m}} - 2\Delta f_{2DFG_{1\mu m}} + \Delta\nu_{clk}\right) \tag{A.25}$$

A.3 Electronic Mixing of Vernier Combs

An alternative approach to locking the two Vernier combs via phase locked loops is to remove the unwanted contributions via electronic mixing. By choosing appropriate division factors prior to mixing the RF beatnotes, we can obtain an RF beat that is a divided version of f_{rep} with contributions of, the now free-running, f_{rep_2} cancelled. For example, the Vernier clock output instability (eq. A.6) is a divided version of the main comb's repetition rate summed with the instability of the Vernier two-comb overlap lock-point. Instead of locking this beat note in a phase locked loop, its contribution to the output clock instability can be cancelled by judicious electronic mixing. For example, if we divide the overlap point by M_2 (the mode spacing between the shared pump line and the overlap point) and mix it with the clock output (i.e. the beating of the first sideband pair in the Vernier case), we obtain

$$f_{RF,mix_1} = f_{clk} - \frac{f_{overlap}}{M_2} \tag{A.26}$$

$$Instability \rightarrow \Delta f_{RF,mix_1} = \Delta f_{clk} - \frac{\Delta f_{overlap}}{M_2} \tag{A.27}$$

$$= \frac{\Delta f_{overlap}}{M_2} + \left(\frac{\delta f}{f_{rep}}\right)\Delta f_{rep} - \frac{\Delta f_{overlap}}{M_2} \tag{A.28}$$

$$= \left(\frac{\delta f}{f_{rep}}\right)\Delta f_{rep} \tag{A.29}$$

The fractional instability, approximating $f_{RF,mix_1} \approx \delta_f$, then is simply $\bar{\Delta} f_{RF,mix_1} = \bar{\Delta} f_{rep}$. Given that we want $f_{overlap}$ to be small ($\sim$ 10 - 500 MHz) and M_2 is on the

order of 50, then $\frac{f_{overlap}}{M_2} \ll f_{clk}$ and it might be difficult to filter out the fundamentals and harmonics after the microwave mixer stage, thus extra care must be given in choosing the mixer to suppress unwanted signals.

Alternatively, we can look into the case of mixing the two beatnotes of the modes adjacent to the overlap point, i.e.

$$f_{RF_1} = (M_2 + 1)f_{rep_2} - (M_1 + 1)f_{rep}$$
$$f_{RF_2} = (M_1 - 1)f_{rep} - (M_2 - 1)f_{rep_2}$$

Our goal here is to use these two signals and remove any contributions of comb-2 (f_{rep_2}). To achieve that we have to divide the two signals by appropriate factors before mixing them:

$$f_{RF,mix_2} = \frac{f_{RF_1}}{(M_2 + 1)} + \frac{f_{RF_2}}{(M_2 - 1)} = \frac{2(M_1 - M_2)}{(M_2 - 1)(M_2 + 1)} f_{rep} \tag{A.30}$$

Assuming that the overlap frequency is sufficiently small, we can approximate $f_{RF_1} \approx f_{RF_2} \approx \delta f$. Thus $f_{RF,mix_2} \approx 2\frac{\delta_f}{M_2}$, where here we approximate $(M_2 + 1) \approx (M_2 - 1) \approx M_2$. With $M_2 = 50$ and $\delta f = 20$ GHz, the output frequency f_{RF,mix_2} is now at ~ 800 MHz and the LO tones may be spectrally filtered. Using eq. A.30 and looking at the fractional instabilities ($\Delta f_{RF,mix_2} = \bar{\Delta} f_{RF,mix_2} \cdot f_{RF,mix_2} \approx \bar{\Delta} f_{RF,mix_2} \cdot (2\delta f / M_2)$, we get

$$\bar{\Delta} f_{RF,mix_2} \cdot (2\delta f / M_2) = \frac{2(M_1 - M_2)}{(M_2 - 1)(M_2 + 1)} f_{rep} \bar{\Delta} f_{rep} \tag{A.31}$$

Approximating $(M_2 - 1) \approx (M_2 + 1) \approx M_2$ and recalling that $\frac{(M_1 - M_2)}{M_2} = \frac{\delta f}{f_{rep}}$ we obtain

$$\begin{aligned}
\bar{\Delta} f_{RF,mix_2} &= \frac{2(M_1 - M_2)}{M_2^2} \cdot \frac{M_2}{2\delta f} f_{rep}\ \bar{\Delta} f_{rep} \\
&= \frac{(M_1 - M_2)}{M_2} \cdot \frac{1}{\delta f}\ f_{rep}\ \bar{\Delta} f_{rep} \\
&= \frac{\delta f}{f_{rep}} \cdot \frac{1}{\delta f}\ f_{rep}\ \bar{\Delta} f_{rep} \\
&= \bar{\Delta} f_{rep}
\end{aligned}$$

resulting in fractional instability similar to that of f_{RF_1} but at a different output frequency (e.g. $\sim$ 800 MHz v.s. $\sim$ 20 GHz).

The choice of either locking the two combs or performing electronic mixing will likely be decided based on the limitations in the system. If the frequency instability of the factor $\frac{1}{M_2}\Delta f_{overlap}$ cannot be sufficiently locked to a low-frequency reference with low fractional instability, electronic mixing may be a more suitable option. That said, a more deeper theoretical and experimental understanding of the limitations in PLLs versus rf mixer and dividers is needed to determine which scheme would be more advantageous.

A.3.1 Transfer oscillator combined with DFG

The transfer oscillator scheme allows using a free-running comb (with no feedback) to transfer the stability of a reference to the microwave domain, provided that the comb's noise and instability contributions are canceled. The previous discussion can be thought of as an example of such schemes (i.e. comb-2 acted as a transfer oscillator for comb-1).

Let us focus on the case of the DFG scheme: our goal here is to mix the beatnote $f_{DFG_{2\mu m}} = \nu_{clk} - 2\nu_o - D_1 f_{rep}$ and $f_{2DFG_{1\mu m}} = 2\nu_{clk} - 3\nu_o - D_2 f_{rep}$ to cancel all contributions from ν_o and f_{rep}. It is straightforward to see that mixing the microwave beatnotes $f_{2DFG_{1\mu m}}$ and $f_{DFG_{2\mu m}}$ divided by 3 and 2, respectively, we can cancel ν_o:

$$f_{2DFG_{1\mu m}}/3 - f_{DFG_{2\mu m}}/2 = \nu_{clk}/6 - (D_1/2 + D_2/3) f_{rep}$$

The next step is get rid of the repetition rate contributions. From the previous section, through the Vernier division scheme, we have obtained a signal that is a divided version of the repetition rate ($f_{RF,mix_1} = \left(\frac{\delta_f}{f_{rep}}\right) f_{rep}$). So now, if we divide

the previous signal by $(D_1/2 + D_2/3)$ and subsequently by $\frac{f_{rep}}{\delta_f}$ and then mix it with f_{RF,mix_1} (eq.A.29), we get

$$\begin{aligned} f_{RF,mix_3} &= \frac{2}{D_1 + 2D_2/3} \cdot \frac{\delta_f}{f_{rep}} \cdot \left(f_{2DFG_{1\mu m}}/3 - f_{DFG_{2\mu m}}/2\right) + f_{RF,mix_1} \\ &= \frac{2}{D_1 + 2D_2/3} \cdot \frac{\delta_f}{f_{rep}} \cdot \frac{\nu_{clk}}{6} \end{aligned}$$

Recall that the division factor can be rewritten as $\frac{2}{D_1+2D_2/3} = \frac{6f_{rep}}{\nu_{clk}}$ (eq. A.24). Therefore, the total division factor $\frac{6f_{rep}}{\nu_{clk}} \cdot \frac{\delta_f}{f_{rep}} = \frac{6}{344.279\times50}$ corresponds to a division by ~ 2868. Such large, and is some cases non-integer, division factors have been experimentally performed in previous demonstrations of the transfer oscillator method using more complicated electronic division methods in order to reduce spurs [213]. Substituting this division factor in the previous equation we can write $f_{RF,mix_3} = \left(\frac{\delta_f}{\nu_{clk}}\right) \cdot \nu_{clk}$; showing that this RF frequency is a version of the clock laser divided down to δ_f. The fractional instability of this RF beatnote then follows that of the clock laser, i.e. $\bar{\Delta} f_{RF,mix_3} = \bar{\Delta}\nu_{clk}$.

VITA

VITA

Mohammed S. Al Alshaykh holds a B.Sc. in electrical engineering from King Saud University and a M.Sc. in electrical and computer engineering from Purdue University. In 2012, he was an intern at Max Planck Institute of Quantum Optics. Mohammed is currently a Ph.D. candidate at Purdue University, where he conducts research in integrated photonics and quantum optics. He has coauthored eight journal articles and numerous conference proceedings. Broadly, his area of interest includes optical frequency combs, integrated photonics, and quantum optics. Mohammed is a member of the Optical Society (OSA) and the Institute of Electrical and Electronics Engineers (IEEE). He is an active reviewer for OSA, IEEE, and the Nature Publishing Group.